Timothy Aschl, Ing, BSc

Tunable artificial cellulose substrates for in situ AFM investigation of enzymatic degradation

MASTER THESIS

For obtaining the academic degree
Diplom-Ingenieur

Master Programme of
Technical Physics

Graz University of Technology

Graz University of Technology

Supervisor:

Ao.-Univ.-Prof. Dipl.-Ing. Dr. techn. Gerald Kothleitner

Co-Supervisor:

Dipl.-Ing. Dr. techn. Harald Plank

Institute of Electron Microscopy and Nanoanalysis

Graz, March 2013

Abstract

Technological progress and economic growth dominates our world. This goes hand in hand with an ever-growing need for resources, especially in the field of energy production. Environmentally friendly means of energy production have to be promoted to counteract global warming. This process will have to be carried by several pillars. A main pillar will be the conversion of renewable biomass to more accessible forms of energy. Second generation biofuels are produced from biomass sources which also take greenhouse gas emissions and land use into account, e.g. cellulose via enzymatic degradation and subsequent fermentation. Cellulose is the most abundant biomass on earth and its structure is characterised by multiple crystal phases. Synergistic effects become apparent when enzymatic degradation is carried out, as some enzymes preferably degrade certain cellulose phases. In order to be able to conduct in situ AFM investigations of the enzymatic degradation the cellulose substrate has to be well defined and nanoflat. This work focuses on the preparation and characterisation of artificial cellulose substrates with tunable properties in respect of crystal phase and particle densities. Microcrystalline cellulose (Avicel) is dissolved in the ionic liquid BMIMCl and dried. In the next step the ionic liquid is removed by a fractional solvent exchange, and then the samples are embedded in epoxy and cut with the ultramicrotomy, yielding nanoflat surfaces. Depending on the mixing ratio of cellulose and BMIMCl and further mixing parameters the substrate properties (crystal phases, crystal distribution) can be controlled. The substrates were characterized with X-ray diffraction, optical microscopy, transmission electron microscopy and atomic force microscopy. This showed the possibility of producing cellulose substrates with mixed or pure crystal phases. A further substrate was characterized. The spin cast cellulose are fast and easy to produce cellulose substrates with no necessity for embedding and ultramicrotomy. They turned out to be ideal testing substrates for enzymatic degradation. Enzymatic degradations of test substrates and of substrates with different crystalline properties will be described and compared. Furthermore evaluations of cellulosomes (multi-enzyme complexes) were performed and their outcome is described in this work.

The tunable substrates which were characterized and tested allow for exact observation of enzymatic degradation on different phases. This will make it possible to describe enzymatic degradation more precisely on a morphological scale, leading to a better understanding of the involved processes.

Kurzfassung

Unsere Welt ist geprägt von wirtschaftlichem Wachstum und technischem Fortschritt. Dies bedingt einen immer größeren Bedarf an Ressourcen, besonders im Bereich der Energieproduktion. Um globaler Erwärmung entgegenzuwirken müssen verschiedene umweltfreundliche Arten der Energieproduktion forciert werden. Dieser Prozess wird von mehreren Säulen getragen werden müssen. Eine Hauptsäule dieses System wird die Umwandlung erneuerbarer Biomasse in leichter zugängliche Energieformen sein. Bei Biokraftstoffen der zweiten Generation werden die Rohmaterialien auch hinsichtlich ihrer Treibhausgasemissionen und Landnutzung bewertet. Ein Beispiel dafür ist Zellulose die enzymatisch abgebaut und anschließend fermentiert wird. Zellulose ist die am häufigsten vorkommende Biomasse der Welt und ihre Struktur ist charakterisiert durch mehrere verschiedene Kristallphasen. Während der enzymatischen Hydrolyse treten Synergismus-Effekte auf, da manche Enzyme verschiedene Zellulose-Strukturen bevorzugen. Um in situ AFM Messungen durchführen zu können müssen die Zellulose Substrate wohl definiert und nanoflach sein. Diese Arbeit konzentriert sich auf die Herstellung und Charakterisierung künstlicher Zellulose Substrate mit einstellbaren Eigenschaften, bezüglich ihrer Kristallinität und Partikelverteilung. Mikrokristalline Zellulose (Avicel) wird in einer ionischen Flüssigkeit (BMIMCl) gelöst und anschließend getrocknet. Das BMIMCl wird mit einem Lösungsmittelaustausch entfernt und dann werden die Proben eingebettet und mit dem Ultramikrotom geschnitten, nanoflache Oberflächen ergebend. Die Substrateigenschaften lassen sich durch das Mischungsverhältnis und weitere Mischungsparameter einstellen. Die Substrate wurden mittels Röntgendiffraktometrie, Lichtmikroskopie, Transmissionselektronenmikroskopie und Rasterkraftmikroskopie charakterisiert. Dies zeigt die Möglichkeit von Substraten mit gemischten Phasen auf. Es wurde ein weiteres Substrat untersucht, die spin cast Zellulose. Diese Substrate sind einfach und schnell herstellbar ohne Notwendigkeit weiterer Präparation für Flüssigkeits-Rasterkraftmikroskopie Messungen. Das Substrat stellte sich als ideales Testsubstrat heraus für enzymatische Hydrolyse. In dieser Arbeit werden auch Untersuchungen zur enzymatischen Hydrolyse auf den Testsubstraten und den normalen Substraten beschrieben. Weiters wurden auch Cellulosome (Multi-Enzym Komplexe) untersucht und die Ergebnisse werden in dieser Arbeit dargelegt.

Die einstellbaren Substrate, die charakterisiert und getestet wurden, ermöglichen die genaue Beobachtung enzymatischer Hydrolyse auf unterschiedlichen Phasen. Dies wird eine genaue Beschreibung des Zelluloseabbaus auf einer Nanoskala möglich machen, was zu einem besseren Verständnis der involvierten Prozesse führen wird.

Acknowledgments

Table of Content

1 Introduction

The world in which we live in today is marked by an enormous technological progress. Especially developing countries and emerging economies are undergoing a rapid economic and technical growth, causing an ever-growing need for resources. This does not only affect the sector of food production but especially the energy production. However, in times of man caused global warming a ruthless and unsustainable production of energy is way more than just counterproductive.

In order to be able to cover the soaring energy needs by environmentally friendly means the alternative energy production will have to be carried by several pillars. A lot of effort is being put into the research of the most commonly known, photovoltaics and wind power. A controversially discussed pillar of alternative energy production is the first generation of biofuels. They are disputed because their production competes directly with food production. The fuels are won from plants which are rich in starch or sugar like corn or sugar cane. As a consequence, especially in developing countries, fields are cultivated with plants for energy production what in turn causes food prices to rise. Therefore research is pushed forward strongly in the field of second generation biofuels. These biofuels are also gained of renewable sources, but this is done taking into account their greenhouse gas emissions, impact on biodiversity and land use. Possible sources are for example algae via fermentation and cellulose via enzymatic degradation and subsequent fermentation.

Cellulose is the most abundant biomass on earth and a very versatile material which inter alia has been used by mankind for thousands of years as building material and for clothes. Described broadly it is a biopolymer of glucose units which is produced by plants, algae, microorganisms and more. Furthermore cellulose is insoluble in water and also in most organic solvents. Depending on its source it has a different structure and morphology. In enzymatic cellulose hydrolysis the cellulose is degraded by enzymes (biocatalysts) into its glucose components (saccharification) which can then be fermented into bioethanol. Even though the mechanisms of hydrolysis are well known empirically much has still to be investigated about the degradation on a structural and morphological scale. Enzymatic synergism effect, product inhibition and more effects are starting to be understood by nanoscale investigations. For this in situ AFM investigations have proven to be a powerful tool, allowing in liquid measurements and visualising the enzymatic degradation on a nanoscale. Using this technique the synergistic effects of enzymes attacking certain cellulose phases were visualized [1]. But these measurement methods call for appropriate, well defined and nanoflat substrates. In order to be able to visualise for example synergistic effects it is necessary for the samples to show multiple cellulose crystal phases, as natural cellulose does.

This work focuses on the preparation and characterisation of artificial cellulose substrates with tunable properties in respect of crystal phase and particle densities. The method of preparation was introduced to this project by Judith Dohr and was further improved to yield reproducible substrates. In this process the cellulose is dissolved in an ionic liquid. Then it is dried and the ionic liquid is removed in a solvent exchange. The result is samples which can be embedded in epoxy and cut with the ultramicrotome, finally yielding nanoflat cellulose samples (called FSEC) which are suitable for investigations of enzymatic degradation. The characterisation was done by a multitude of means. X-ray diffractometry, optical microscopy, transmission electron microscopy and atomic force

microscopy were applied, revealing the properties regarding crystal phase and crystal distribution. I.e. it is now possible to produce multiphasic cellulose substrates which allow the observation of enzymatic activity with specific crystal phases. Since the production of this substrate is very time consuming a new test substrate was introduced and characterized. The spin cast cellulose (SCC) is an easy and fast to produce cellulose with a nanoflat native surface making embedding and ultramicrotomy cutting unnecessary. Characterization of the SCC revealed similar properties like certain FSEC samples. Also investigations of enzymatic degradation have been conducted, further confirming the usability of SSC as test substrate. In situ AFM degradation investigations have also been performed for a relatively new class of promising multi-enzyme complexes called cellulosomes.

2 Biological and chemical fundamentals

2.1 Cellulose

Cellulose is a biological polymer. As stated in literature several times before, it is the most abundant biological material on earth with an estimated annual production of 10^{11}-10^{12} tons by plants, but also by bacteria, algae and fungi [2], [3]. It is often found to form a composite with lignin and other polysaccharides [4]. Although the knowledge on cellulosic biosynthesis is growing rapidly many answers are still to be found [3].

Cellulose is water-insoluble, tough and has been used by mankind in a multitude of ways, e.g. as construction material or for clothing. Due to its abundance it represents a potential source of renewable energy. The problem with this is that cellulose is very stable by nature and not easy to decompose. In order to produce biofuels the cellulose has to be converted. Two main ways of conversion are being researched on: biochemical and thermochemical. The biochemical conversion is carried out by hydrolysis (e.g. enzymatic, dilute acid or concentrated acid hydrolysis) and followed by fermentation resulting in ethanol. The procedure of thermochemical conversion usually starts with gasification or another thermal treatment. The resulting ethanol or other fuels is gained by catalytic synthesis or fermentation of the gas or liquid [3].

For more information on cellulose than is laid out in this chapter please refer to [2], [3].

2.1.1 Molecular structure

Cellulose is a linear polymer and it consists of β-D-glucopyranose units (anhydroglucose units (AGU)) covalently linked by β-1,4-glucosidic bonds (Fig. 1). The pyranose rings adopt the thermodynamically favored $^4C_1$ chair conformation and every second one is rotated 180° in the plane. This conformation is stabilized by intramolecular hydrogen bonds, leading to chain stiffness. Intermolecular hydrogen bonding is responsible for binding between molecules and the development of cellulose crystals. The chain ends with a C4 hydroxyl group (non-reducing end) and on one side, and with a C1 unsubstituted hemiacetal (reducing end) on the other side [3], [4], [5].

The degree of polymerization (DP) is the number of monomeric units in the polymer. The DP of celluloses depends on the origin and treatment and its values range from 100 (e.g. cellulose powder after milling) to 44000 (Valonia) [3].
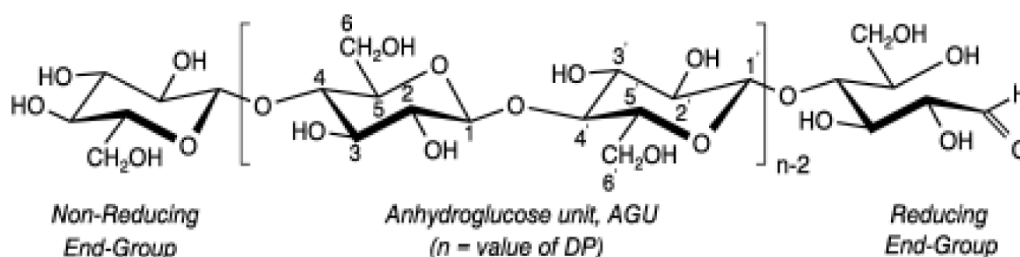
Fig. 1: Molecular structure of cellulose with numbered carbon atoms [5].

2.1.2 Supramolecular structure

Cellulose appears in a multitude of polymorphs (Iα, Iβ, II, III$_I$, III$_{II}$, IV$_I$, IV$_{II}$) [3], [6]. Polymorphism is the characteristic of a solid material that it can exist in different forms or crystal structures. A very well-known example for polymorphism is carbon and its forms graphite, diamond, graphene and fullerene.

Most natural cellulose is of the polymorph **cellulose I**. ^{13}C NMR has revealed that this polymorph can actually be distinguished as the two polymorphs cellulose Iα and Iβ [5]. The main difference can be found in the unit cell. While cellulose Iα has a triclinic unit cell with one chain the cellulose Iβ consists of a monoclinic cell with two chains (see Fig. 2 for unit cell of Iβ). Both phases can exist within a single crystalline fibril. It has been proven, that the metastable Iα phase can be converted to the more stable Iβ by high-temperature annealing [3], [7].

Cellulose II is obtained from cellulose I when it has undergone either regeneration (dissolving and precipitating) or mercerization (swelling in sodium hydroxide and removing swelling agent) [6].
The transformation is irreversible because cellulose II is thermodynamically more stable than cellulose I. Research on the structure of cellulose II presented two anti-parallel chains and a monoclinic unit cell (Fig. 2) [3].

Cellulose III$_I$ and III$_{II}$ can reversibly be generated from cellulose I and cellulose II, respectively. The phase change is performed by swelling with liquid ammonia or amines and consecutive anhydrous removal. The structure of cellulose III depends on if it was formed of cellulose I or II, the unit cell of cellulose III$_I$ is monoclinic (Fig. 2) [3].

Cellulose IV is formed by heating cellulose III in glycerol. The polymorphs IV$_I$ and IV$_{II}$ come from the polymorphs III$_I$ and III$_{II}$, respectively. The unit cell was reported to be orthogonal and is displayed in Fig. 2 [6].
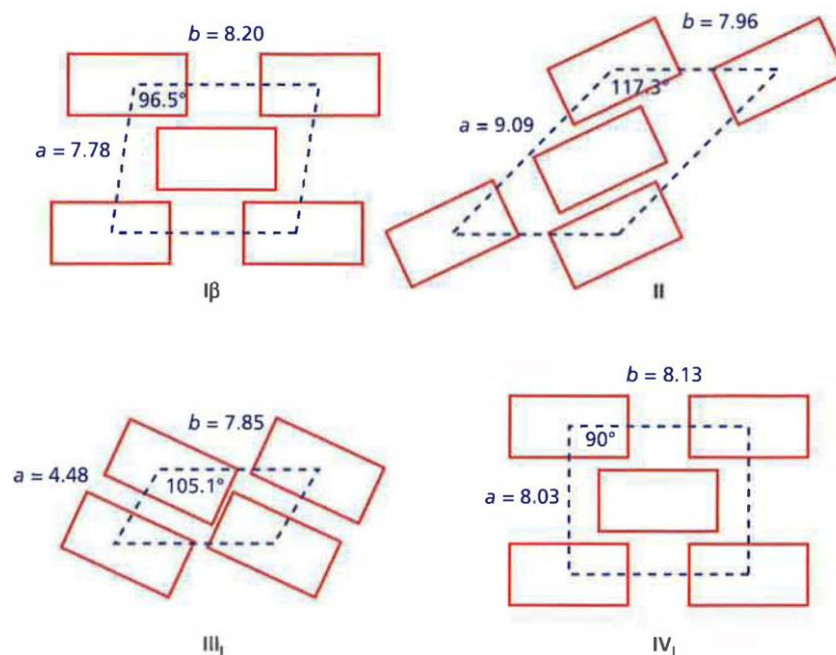
Fig. 2: Proposed unit cells for the cellulose polymorphs Iβ, II, III$_I$, IV$_I$; dimensions: a and b in Å, γ in degrees, c is perpendicular to the drawing and is between 10.31 and 10.38 Å [3].

Even though **amorphous cellulose** has been described in literature, it probably does not exist in the strict sense of the term "amorphous", as this would mean the regions of amorphous cellulose would lack long-range order and crystal characteristics. Nevertheless the regions identified as amorphous possess a certain degree of order [6]. Amorphous cellulose is understood as regions with disordered chains, although short-range order is possible.

2.1.3   Morphological structure

The morphological structure describes the structural organization of cellulose. It can be found in form of fibrils, fibers, tissues, layers, cell walls and many more [3].

In nature the cellulose is usually in form of fibers. For example, in primary cell walls the cellulose chains are less ordered and not oriented, while the chains are organised into more densely packed, parallel microfibrils in secondary cell walls. [6]

A very interesting point about regenerated cellulose is in the morphological possibilities it offers. Depending on the solvent and regeneration process the regenerated cellulose can be manufactured in nearly any morphology, like fibers or films. This capability is the basis of this thesis which uses regenerated films as source material for artificial cellulose substrates.

2.2   Ionic liquids and cellulose dissolution

Ionic liquids (IL) are molten salts. To melt a salt the strong ionic bond between the anions and cations has to be overcome, which generally demands high temperatures. When molten, the liquid salt consists entirely of ions. ILs are basically a subgroup of molten salts, divided from them by their melting point, which is lower than the boiling point of water. But the main difference setting them apart from molten salts is the fact that they can be treated like normal solvents [8].

One reason why so much effort is being put into ionic liquids is the amazing properties they have. They have a huge liquidus range (the temperature range between boiling and freezing point) and are **non-volatile** organic solvents [8]. ILs have excellent stability and are not easily flammable. Further they are almost entirely recoverable (>99.5 %) and reusable [9]. And finally there is a vast amount of different ionic liquids available. This makes finding a suitable IL as solvent relatively easy (see [10] for a lineup of 67 ionic liquids).

Ionic liquids are often regarded to as green and environmentally friendly solvents [11]. This is done even though ILs show toxic behavior towards bacteria, algae and cells [12]. The argument in favor of ionic liquids is that due to their non-volatility their volatile organic compound emissions can be mostly avoided, which is a major problem with traditional organic solvents. This makes the ILs more environmentally friendly in comparison [13]. Even though the vapour pressure is immeasurably low most ILs are readily soluble in water, whereby they can cause environmental damage easily. In all these discussions it should not be forgotten, that once ionic liquids are used in industrial applications the risk of accidental spilling or contamination rises immensely.

A lot of effort is put into the research of cellulose dissolution in ionic liquids. Cellulose is relatively difficult to dissolve; neither water nor most organic solvents can fulfill this task, but many ionic liquids dissolve cellulose with varying maximum cellulose content [10]. In the context of our work we concentrated on BMIMCl (1-N-butyl-3-methylimidazolium chloride), which is one of the most commonly used. The chemical structure of BMIMCl is displayed in Fig. 3. Moultrop et al. showed with ^{13}C NMR studies that cellulose is dissolved and disordered in BMIMCl, but not degraded [14]. Further studies have proposed the solvation to be propelled mainly by the chloride ions in the IL. They interaction is thought to take place between the chloride ions and the hydroxyl protons of the cellulose [15]. These interactions disrupt the hydrogen bonding in the cellulose and thereby dissolving it. BMIMCls maximum capability of dissolving cellulose has been reported to be between 6 wt. % and 15 wt. % [13], [16].
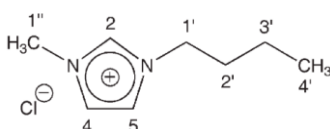
Fig. 3: Structure of BMIMCl [17].

Additional information on BMIMCl and on other ionic liquids can be found here [8], [11], [15], [18].

2.3   Cellulase

Enzymes are biocatalysts which reduce the activation energy of specific reactions. Already small amounts are active and they are not consumed by the reaction – they can be reused over and over again. Even though they accelerate conversion speed, enzymes do not shift the position of equilibrium. Every enzyme has an active site which is responsible for the catalytic reaction. The active site works with the substrate in a key-lock principle. The catalytic mechanism can be driven by hydrogen bonding, ionic bonding, electrostatic interactions and covalent bonding. There are several types of enzymes like nuclease, protease, synthase and hydrolase. The group of hydrolase are enzymes which catalyse hydrolysis, and include cellulase.

Cellulases are enzymes which specifically degrade cellulose to its cellobiose components. The process of degradation by cellulases is usually called enzymatic hydrolysis of cellulose or cellulolysis. Cellulases are mainly produced by microorganisms (bacteria, fungi, aerobes, anaerobes) [19]. The cellulases used for further research in this work were from the fungi *Trichoderma Reesei*. This enzyme system was chosen because it is one of the most investigated and because of its ability to secrete large amounts of cellulase. Furthermore it provides all necessary components for cellulose degradation. For more information specifically on Trichoderma Reesei refer to [20], [21], [22].

There are multiple ways of producing cellulases. In order to make the production of bioethanol economical and profitable the refinement of cellulases has to be as cheap and efficient as possible, and a lot of effort is being put into research that.

All cellulases used in measurements were prepared by DI Manuel Eibinger and DI Dr. Patricia Bubner from the Institute of Biotechnology and Bioprocess-Technology.

Cellulose can degrade to cellobiose and oligosaccharides in presence of water, but the process is not very likely to happen at room temperature. The cellulases only accelerate (catalyse) the degradation. Cellulases tend to have cellulose-binding domains (CBD) in addition to the catalytic core. The CBDs cause a nonhydrolytic fiber disruption of the cellulose. [21]

Enzymes are a well-studied and large field. Much more information can be found in according literature [23] [20].

2.3.1 Hydrolytic Enzymes

There are three main enzymes of *Trichoderma Reesei*, on which these investigations concentrated. They are the endoglucanase (EG) and the two exoglucanases called cellobiohydrolases (CBH1 and CBH2). Together they show synergistic effects, accelerating the cellulose degradation immensely (see [1] for more information).

2.3.1.1 CBH1

CBH1 (EC 3.2.1.91) is an exoglucanase and it has a catalytic core domain (Fig. 4) and a CBD. In general exoglucanases cleave from free cellulose chain ends, separating cellobiose from the chain. CBH1 attacks the reducing ends. The cellulose has to thread through a tunnel in which the active site is located [22].
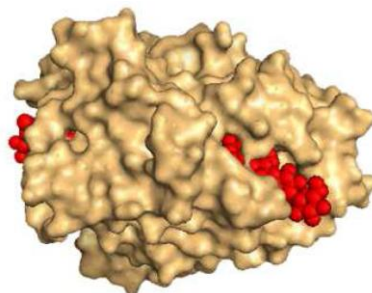
Fig. 4: Side view of the catalytic core domain of CBH1, with cellulose threading through [24].

2.3.1.2 CBH2

CBH2 (EC 3.2.1.91) is also an exoglucanase and is quite similar to CBH1. Its catalytic core domain is shown in Fig. 5. The main difference is that CBH2 attacks the non-reducing end, cleaving cellobiose.
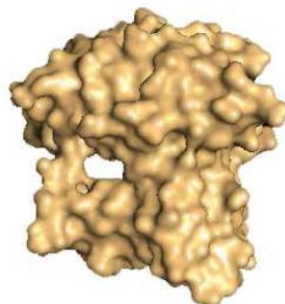
Fig. 5: Front view of the catalytic core domain of CBH2 [24].

2.3.1.3 EG

EG (EC 3.2.1.4) is an endoglucanase and cuts cellulose chains at random places, increasing the reducing and non-reducing ends. This raises the possibility of degradation by CBH1 and CBH2. The structure of EG shows a grabber and trench with which the cellulose is degraded (Fig. 6). It works best on amorphous cellulose due to its form.
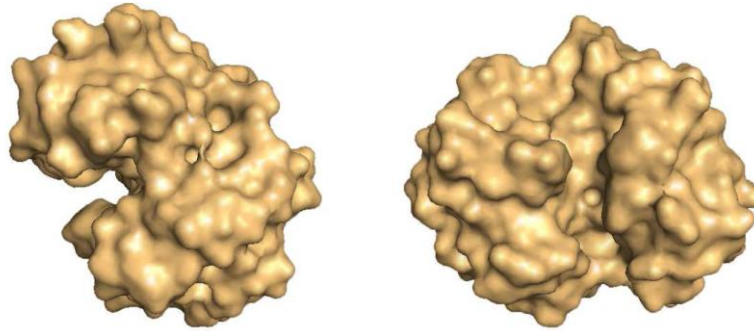
Fig. 6: Side and bottom view of EG 3, displaying the grabbing trench [24].

2.3.1.4 CBD

Cellulose binding domains are not enzymes, but part of them. They are chemically inert, but modify physical and chemical properties of materials. CBDs can be used for cell immobilization and protein engineering. Furthermore, they can cause nonhydrolitic fiber disruption, allowing for faster enzymatic degradation [25].

2.3.2 Cellulosomes

Cellulosomes are multi-enzyme complexes. They consist of a scaffolding (or scaffoldin) subunit which is responsible for the organization of the various kinds of cellulases. The cellulases bind to the scaffolding by its dockerin domains which interact with the cohesion domains of the scaffolding. This allows multiple and varying cellulases on one complex. Synergistic effects become easily accessible and important through this setting [26], [27]. Cellulosomes look like a very promising option for biofuel production. Therefore a lot of effort in research is recently going into researching them.

For more information on cellulosomes turn to [26], [27], [28].

3 Experimental techniques

3.1 Ultramicrotomy

Over the last decades various sample preparation methods have been developed for microscopic investigation techniques (e.g. TEM, SEM, AFM). These preparation methods can basically be divided into preparation of surfaces, preparation of thin layers and preparation of thin cuts [29]. Ultramicrotomy is a mechanical process to cut ultra-thin slices down to 20 nm [29] or gain nanoflat surfaces.

All ultramicrotome cuts were done by Ing. Claudia Mayrhofer at the Institute for Electron Microscopy and Fine Structure Research, TU Graz.

3.1.1 Working principle

The specimen is usually embedded in a resin and then moved past a stationary knife of glass or diamond repeatedly. In each cycle the sample holder (and with it the sample) is moved a certain, adjustable distance in direction of the knife. The thickness of the cut slice corresponds to the forward feed of the sample holder. The quality of the cuts depends on cutting parameters and the sample material. Main cutting parameters are knife type, knife quality, knife angle, cutting method, temperature, feed speed. Material characteristics which influence ultramicrotomy are for example compressibility and plasticity.

The ultramicrotome used for the samples in this work is displayed in Fig. 7. Samples of knives can be seen in Fig. 8. Some knives have a trench which can be filled with liquid (e.g. water, buffer solution). The trench has two main applications: thin slices, which were cut, float on the liquid and can be collected for further investigation and it also enables cutting of wet samples without letting them dry.

Fig. 7: Ultramicrotome (Leica EM UCS-NT) [30].
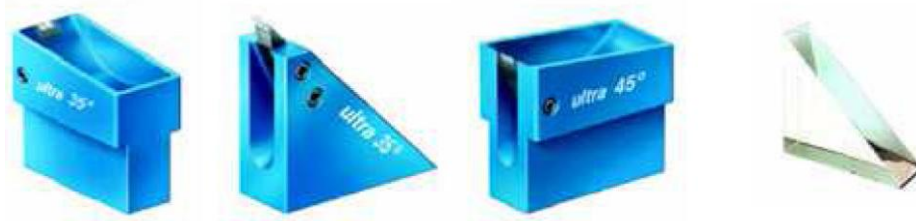
Fig. 8: Ultramicrotome-knives. Three different diamond knives (with and without trench, different angles) and a glass knife.

For further information on ultramicrotomy and knives see reference [29].

3.2 X-ray diffractometry

X-ray diffractometry (XRD) is a basic method of material characterization. It uses elastic scattering of X-rays from atoms to retrieve information on atomic / molecular / crystallographic structure. The main points of X-ray radiation, X-ray generation, X-ray detectors and crystallography have been described in detail elsewhere [31], [32]. The discussion here will just shortly describe diffraction in general and X-ray diffraction of polymers / cellulose.

A diffraction experiment consists of an incident beam which is directed to a sample at a certain angle (θ) and the diffracted intensity is measured. A simple approach to explain the diffracted intensity is the *Bragg's law*, which can be found by geometrical considerations. The incident beam is diffracted by the lattice plains (different parts of the beam are diffracted by different plains). To get optical interference the additional travelled distance has to be a multiple of the X-rays wavelength (λ) resulting in $\lambda = 2d_{hkl}sin\left(\frac{2\theta}{2}\right)$. Where n is a natural number, d is the distance between atomic planes, hkl represent the Miller indices of the Bragg plane and θ is the angle between incident beam and scattering plane. This is all under the condition that the outgoing beam angle is equal to the incoming one. The interference peaks which occur at certain angles then allow conclusions to be drawn on the crystal size, symmetry and perfection.

For characterizing polymers there are multiple methods. Which one to choose depends on the specimen's form, its orientation, etc. [31]. Krässig [2] for example mentions that small angle X-ray scattering can be used to determine the average molecular mass of cellulose. He furthermore describes the possibility of cellulose characterization by X-ray diffraction by small angle (SAXS) and wide angle XRD (WAXS). Also powder diffraction and single crystal technique can be used for cellulose characterization, making it possible to determine e.g. degree of orientation, crystallinity and crystallite dimensions (with varying results, see chapter 6.1), unit cells and polymorphic composition.

Unless mentioned differently, all XRD-measurements were performed with a *Siemens D501 diffractometer (CuKα 1 radiation; Siemens, Munich, Germany)*. The method of measurement used was the θ-2θ-method. In evaluation a linear baseline was subtracted from the spectrum and the curve was smoothed with a FFT-filter. Furthermore, the curves were often integratively normed to allow relative comparisons of different diffraction peaks.

3.3 Raman spectroscopy

Raman spectroscopy investigates the inelastic scattering of light on solid or liquid samples. The incoming monochromatic light is absorbed and excites an electron into a virtual unstable energy state. Light is remitted when the electron relaxes. If the electron relaxes into a different vibrational or rotational state then it started from the emitted photon has a different wavelength then the incoming light. This effect is called Stokes shift and anti-Stokes shift, for downshift and upshift of energy respectively. The spectra (intensity over shifted wavelength) which are obtained by these measurements allow rapid retrieving of a sample's chemical composition, molecular structure, bonding effects, internal stress and more. The theoretical background and more details on the use of Raman spectroscopy can be found in literature [33].

All Raman measurements in this work were conducted by Mag. Dr. Boril Chernev on a Horiba Jobin Yvon LabRam 800 HR, 1024 x 256 px Peltier-cooled CCD, confocal Olympus BX41 Microscope. Laser 633 nm (He-Ne), Objective x100 (NA=0.9), Grating with 300l/mm.

3.4 Scanning electron microscopy

In Scanning electron microscopy (SEM) a focused electron beam interacts with a sample. The beam scans the sample point by point, one line after another. Each point represents a position on the sample with certain properties. The beam-sample interaction at each point generates a myriad of evaluable signals. The signals usually used are the ones generated by secondary electrons, backscattered electrons and characteristic X-rays. Secondary electrons are emitted valence electrons which are excited upon inelastic scattering and show low energies (per definition < 50 eV). This allows them only to travel a short distance of a few nanometer which therefore provides best resolution. The contrast of secondary electrons originates mostly from sample topography [34]. Backscattered electrons are primary electrons which were elastically (back) scattered from sample nuclei, therefore revealing high energies. Since they can travel a much longer distance they stem from deeper areas which worsens the lateral resolution. Contrast is from differences in average atomic number (the higher the Z the higher the backscattering). But the SEM has some major limitations like vacuum constraints (high vacuum is necessary) and sample constraints (they must be vacuum tolerant and electrically conductive). Further information can be found in literature [35], [34].

All SEM measurements in this work were conducted with DI Dr. Harald Plank on a FEI NOVA200 FIB/SEM Dual Beam Microscope.

3.5 Transmission electron microscopy

The Transmission electron microscopy (TEM) takes advantage of the electrons duality of particles and waves appointing a wavelength to the electron via the de Broglie wavelength ($\lambda_e = h/m_e v$). Where λ_B is the de Broglie wavelength, h is the Planck constant, m_B is the particle mass and v its velocity. A TEM is basically constructed like an optical microscope, but with electro-magnetic lenses instead of lenses of glass. The sample is penetrated by an electron beam, the non-absorbed part of

the beam is then recorded. Theoretically the same rules for resolution limits apply for the TEM as for the optical microscope. This would make a TEMs resolution higher by a factor of 10^5 compared with the optical microscopes resolution (visible light: $\lambda = 0.4 - 0.8$ µm; electrons accelerated with 20 - 200 kV: $\lambda = 8.6 - 2.5$ pm [29]). Nevertheless, due to non-perfection of electron lenses the real resolution of a TEM is a lot less, around 30 pm for state of the art instruments [36].

Even though the TEM offers amazing resolution possibilities such as chemical bond mapping in between individual atoms, some problems arise. Interpretation can be difficult as the recorded 2D images actually represent a 3D projection in transmission direction. Another problem is that the electron beam can severely damage sensitive samples such as biological material. But the most difficult part is the sample preparation as the samples have to be thin enough to not absorb too much of the electron beam. Thicknesses under 100 nm are suggested, for high-resolution TEM 50 nm and less is absolutely required [36].

Further information can be found here [36].

All TEM measurements in this work were conducted by DI Arno Meingast and DI Dr. Harald Plank on a FEI Tecnai F20. All images captured are zero-loss filtered bright-field images.

3.6   Atomic force microscopy

The atomic force microscope (AFM) is an extremely versatile microscope which, unlike most other microscopes, generates images on a nanoscale by "feeling" and not by "looking". But it is not only bound to imaging and measuring, manipulations can also be conducted. Depending on the measurement mode it allows to retrieve a sample's 3-dimensional topological information, surface properties (e.g. roughness, elasticity, hardness, adhesion), material differences, magnetic domains and many more. In the AFM it is even possible to image in-situ measurements of biological processes in liquids.

The AFM is part of the group of scanning probe microscopes, which use probes (tips) to retrieve information. In the early 1980s Gerd Binning and Heinrich Rohrer invented the scanning tunnelling microscope (STM) which works by detecting the current flowing between a sample and a very closely positioned tip. Nevertheless the STM is very limited when detecting materials which are not well conducting. This led to further development being carried out which led to the invention of the contact mode AFM. Since then the AFM has undergone a rapid development leading inter alia to amplitude modulation AFM, in situ liquid imaging, multifrequency AFM, and high-speed AFM [37].

This chapter will only present an outline on how an AFM works. It will also contain a brief section on liquid imaging in AFM (also liquid cell AFM or LC-AFM). For more informations on AFM consult [26], for AFM of biological samples consult [38].

All AFM measurements in this work were conducted on a Dimension 3100 (Digital Instruments, VEECO) with a Hybrid X-Y-Z closed loop scan head and a Nanoscope IVa controller (Bruker).

3.6.1 Fundamental principles

The functionality of an AFM is actually quite simple and will be explained on basis of Fig. 9, where it is compared with the human motoric and tactile abilities when sensing. It consists of four main parts:

1 & 2: Tip & Cantilever
3: Motion system
4: Detection system

Sensing with our fingers is similar to sensing with the very sharp tip (1). When the tip comes along height changes the cantilever (2) it is attached to bends. The same can be thought of to happen in the arm were the joints allow for adjustment. While muscles are used to move the arm and finger a motion system (3) takes on that task in the AFM. Not entirely unlike the muscles which move the arm the motion system is driven by piezoelectric actuators. The last main component is the detection and feedback system (4). The detection system can be compared to nerves and eyes in a human and the feedback corresponds to the brain which links the detection system with the motion system. The detection system registers deflection of the cantilever when the tip moves over changing heights. Many different systems exist for the detection system. In the first AFMs a tunneling current was used to detect deflection. Also self-sensing cantilevers with piezoresistive layers have been developed [37]. Nevertheless the most common system of detection is by optical means (as displayed in Fig. 9). In optical detections systems usually a laser beam is reflected from the end of the cantilever and detected by a four segment photodetector. It allows simultaneous acquisition of cantilever deflection and contortion. The feedback system (which is not displayed in Fig. 9) will register the signal detected and tell the motion system what to do in accordance to the applied measurement technique.
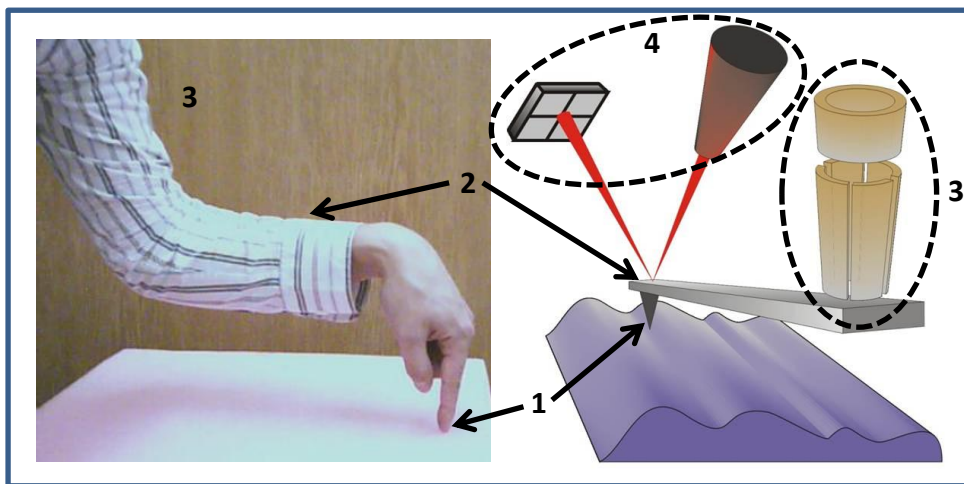
Fig. 9: The basic principle of atomic force microscopy [39]. The components 1 – 4 are explained in the text.

3.6.2 Components

The main components (cantilever-tip system, motion system, detection and feedback system, imaging formation) will be explained in more detail in this chapter.

3.6.2.1 Cantilever-tip system

The probably most important part of an AFM is the cantilever-tip system. Two examples are displayed in Fig. 10. The tip is on the end of the cantilever and the whole system is attached to a glass chip to enable easier handling.

The tip is a micro-fabricated spike. Its geometry is influential on the quality of measurements. Sharp tips resolve fine structures better than dull tips but are also more sensitive and take damage easier (Fig. 11). The lateral resolution is mainly determined by the tips apex. The smaller the apex is the higher the possible resolution gets. Standard commercially available tips have a radius of 5 - 10 nm although also smaller tips are available with radius down to 2 nm [37].

The cantilever has two basic geometries, triangular and rectangular (Fig. 10). The v-shaped triangular ones were originally intended to be stiffer and more resistant to lateral forces. Sader and Sader conducted measurements on macroscopic cantilever models and verified that rectangular cantilevers have a higher lateral force resistance [40]. The force which is applied on the sample depends on the spring constant of the cantilever. Longer cantilevers have a lower spring constant and therefore exert less force to the sample. But it should not be forgotten, that a longer cantilever has lower sensitivity in optical detection systems as the displacement of the reflected beam is inversely proportional to the length of the cantilever.

The cantilever determines the operation mode. Depending on geometry and spring constant the tips can be applied for contact mode, non-contact mode, tapping mode or force spectroscopy.
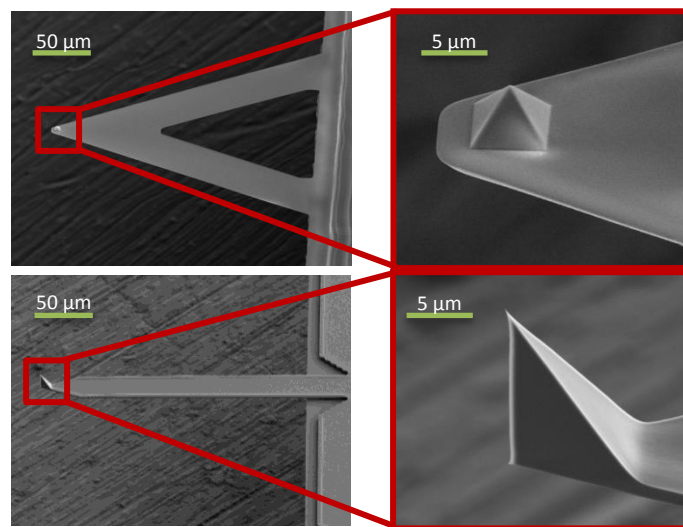
Fig. 10: SEM images of typical cantilever (top: triangular, bottom: rectangular) and tips (top: pyramidal, bottom: tetragonal) [39].
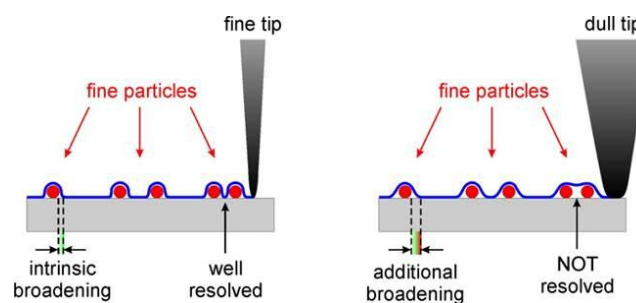
Fig. 11: Influence of a fine tip (left) and a dull tip (right) on the image quality [39].

3.6.2.2 Motion system

Two basic motion system types are used in modern AFMs: either the tip is moved or the sample is moved by piezoelectric actuators. They can be arranged in several ways. The first arrangement used by Binnig was a tripod which is rather imprecise. The tube scanner (as depicted in Fig. 12) is more precise and allows greater scan areas. Their disadvantages are that far motions in x or y direction lead to an arc in the trace and that the tube scanner is rather slow. In the meantime newer and better scanners are starting to be available in high performance AFMs [38].

In general piezoelectric scanners struggle with the usual problems of piezoelectricity – hysteresis, creep, aging and thermal drift. There are countermeasures which can be taken (software algorithms and closed-loop scanners). But regular calibrations should be done to compensate for sensitivity changes.
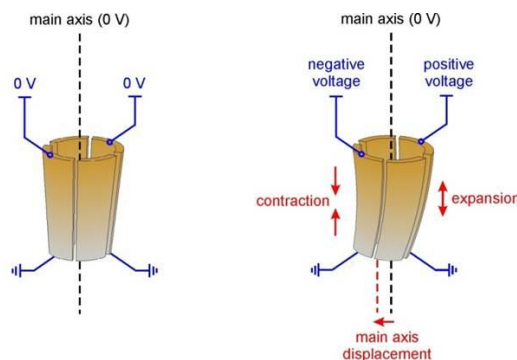
Fig. 12: Piezo tube scanner uncontracted (left) and contracted (right) [39].

3.6.2.3 Detection and Feedback system

Only the optical beam detection will be explained here. Other detection methods are described well in literature [26]. The detection by optical means is displayed in Fig. 13. A laser beam is focused on the cantilevers end from where it is reflected to a photo sensitive detector (or PSD). The PSD detects the position of the laser beam. When the cantilever bends the laser is reflected to another position on the PSD which gives feedback on the bending of the cantilever. The smallest detectable cantilever deflection is around 0.01 nm if the system is set up well [37].
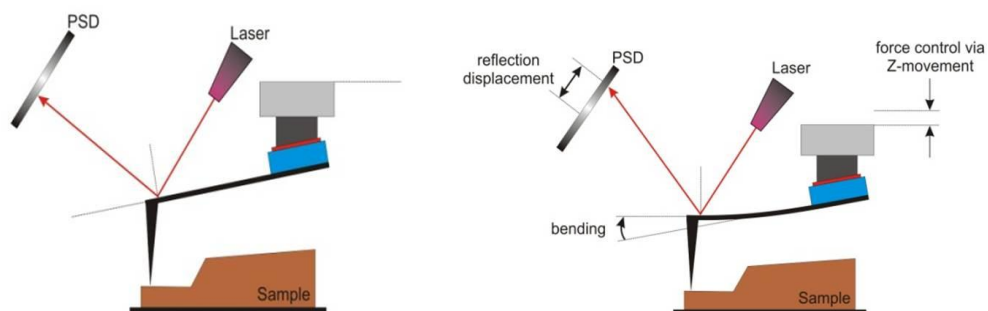
Fig. 13: Optical beam detection with straight (left) and with bent cantilever (right) [39].

The feedback system is the link between the detection and the motion system. It processes the incoming signals from the PSD and controls the piezo scanner depending on the operational mode and the user set controlling parameter like integrational gain or proportional gain.

3.6.3 Tip-sample interactions

AFM images basically depend on the force between the tip and the sample. As the tip approaches the sample it experiences different forces – from long range (electrostatic) to short range (electron repulsion). The forces depend not only on the tip-sample distance but also on the cantilever-tip and sample material as well as the environment of measurement conditions (air, inert gas, vacuum or liquid).

The main forces which act between sample and tip are listed in Table 1:

Table 1: Tip-sample interaction forces.

Tip – sample separation r	Dominant interaction type	Potential dependence (a,b,c…constants)
$> \sim 10$ nm	Electrostatic (magnetic)	$\dfrac{c}{r^2}$
~ 10 nm to ~ 0.5 nm	Van der Waals interaction (dipole-dipole interaction)	$-\dfrac{a}{r^6}$
$< \sim 0.2$ nm	e$^-$ - e$^-$ repulsion (Pauli principle)	$\dfrac{b}{r^{12}}$

For further consideration the electrostatic (magnetic) forces can be ignored since the working distance is usually smaller than 10 nm. Then the forces on the cantilever can be calculated from the sum of the attractive Van der Waals potential (V_{VdW}) and the potential of the electron repulsion (V_{rep}). This is also known as the Lennard-Jones-Potential (with r the tip-sample separation):

$$V_{LJ} = V_{rep} + V_{VdW} = \frac{b}{r^{12}} - \frac{a}{r^6}$$

A qualitative depiction of the Lennard-Jones potential (blue line) is displayed in Fig. 14. In the green region the attractive forces predominate, while in the red region the repulsive forces dominate.
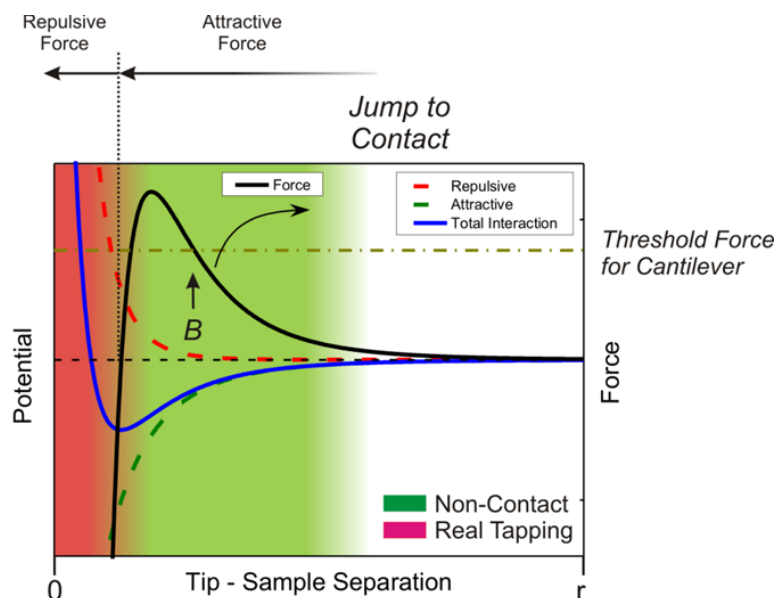
Fig. 14: Schematic drawing of the Lennard-Jones potential between tip and sample [39].

Ergo when approaching the surface, the tip will first feel attractive forces and will be pulled in direction of the sample, bending the cantilever downwards (this is used for measurements in the attractive region which can be more material sensitive). When the tip is only a few angstroms from the sample the strong Pauli repulsion becomes predominant and the tip is repelled, causing the cantilever to bend upwards (measuring in the repulsive region gives very precise topological information and high resolution).

There are also other forces which interact between tip and sample like adhesion and capillary forces [37]. Capillary forces are probably one of the most resolution limiting influences in AFM. Water, from the vapour present in air, condensates between the tip and the sample. The tip with its small radius resting on the sample is a perfect nucleation site. Water can also already be on the sample if the surface is hydrophilic. In both cases a meniscus between sample and tip will be formed which will greatly disturb imaging.

3.6.4   Operation modes

There are three main modes of imaging:
* Contact mode
* Non-contact mode
* Tapping mode

In this chapter also tapping in liquid will be described.

3.6.4.1   *Contact mode*

The tip is in direct contact with the sample's surface without any excitation. The tip is relatively soft and moved over the sample with constant cantilever deflection. The piezo-scanner compensates changes of the deflection, allowing readout of vertical changes of the sample. The applied force is always constant and is set in the instrument software. With a four segment PSD also contortion of the cantilever can be evaluated giving results on local friction values.

Through the constant applied force both tip and sample have to be very insensitive as they will take damage quickly otherwise. Contact mode can also be conducted in liquids.

3.6.4.2   *Non-contact mode*

In this case the tip never touches the sample. The cantilever is excited by an additional piezo at its resonance frequency and with pre-set amplitude. Its oscillation is damped (the amplitude is reduced) by the attractive long range van der Waals forces. This mode enables true atomic resolution [38]. The advantage is that nearly no force acts on the sample allowing imaging of highly sensitive samples. Nevertheless these measurements are quite difficult to conduct. If the tip gets too close to the sample it might hit it and also get "glued" to it by capillary forces. If this happens repeatedly the tip is bound to be damaged. This is especially difficult for rough samples.

3.6.4.3   Tapping mode

In tapping mode the cantilever is also excited by a piezo to the cantilevers resonance frequency and a set amplitude (black curve in Fig. 15). When the cantilever approaches the sample the amplitude is damped (blue and red curve in Fig. 15). The sample-tip interaction can be evaluated by the damped amplitude. The system is set to maintain a constant damped amplitude, thus applying a constant force.

The cantilevers resonance frequency depends on its geometry, size and material and under normal conditions the software can "Auto-Tune" to the resonance frequency with a frequency sweep. This frequency is then used for the external excitation. Common values for the resonance frequency are between 15 kHz and 450 kHz.

The set up enables selecting the working regime for imaging. Depending on the amplitude setpoint the images are acquired in the attractive or repulsive regime. In the **attractive regime** the tip is not in contact with the sample which is advantageous for sensitive samples. It also provides high resolution. The tip softly (the force depends on the settings) taps the surface when in the **repulsive regime**. Often this allows for more stable imaging, as water-meniscus does not influence measurements in this regime. But the sample can be damaged as the tip is constantly tapping on the surface.
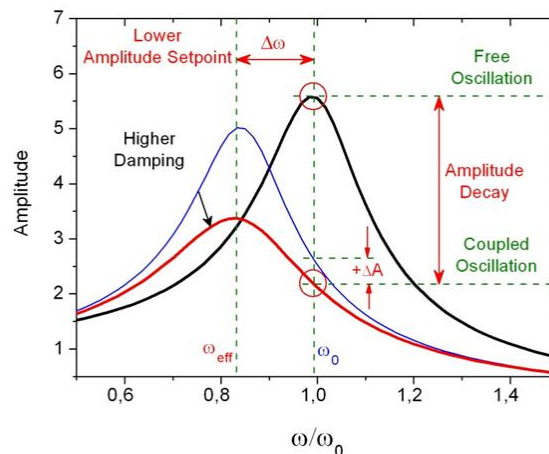
Fig. 15: Oscillation amplitude for free oscillation and coupled oscillation [39].

Another imaging method while tapping is the phase mode. When the piezo (exciter) excites the cantilever (excited) the whole system can be seen as a driven damped oscillator with a phase lag between exciter and cantilever ($\frac{\pi}{2}$ when far from sample and undamped). The lag for free oscillation is detected and set to zero by the controller. The tip-sample interaction damps the oscillation resulting in a phase lag which indicates the interaction. Attractive forces cause lower resonance frequencies, while repulsive forces cause higher resonance frequencies. Thus the working regime can be detected and controlled by the phase signal. Generally the phase signal is acquired at the same time as the height image and yields topological information on the material comoposition, mechanical hardness, viscoelasticity and more [37].

Often higher resolution can be gained with phase images than with height images and can be an useful additional information in addition to the topographic images. Nevertheless, phase lag strongly depends on the material – two different materials might not appear as such due to similar lag.

3.6.4.4 Tapping mode in liquid

Measuring in liquid opens a whole new world for AFM imaging. It makes possible to visualize biological samples and processes *in situ*. For implementation a special sealed tip holder, a special cantilever and a liquid cell (see Fig. 16) are necessary.
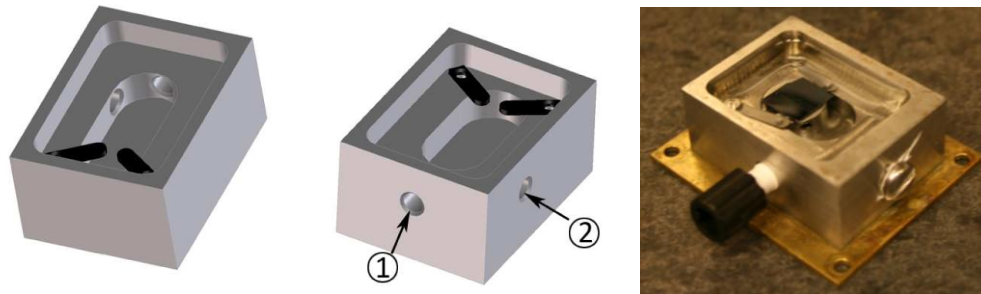
Fig. 16: Left: 3D-image of liquid cell with hole for injection system (1) and temperature sensor (2) [24]. Right: picture of the in-house built liquid cell.

There are a few things that drastically change in liquid. One advantage is that capillary forces are avoided. But in turn the cantilevers resonance changes due to the aqueous environment, making proper tuning difficult. When oscillating in liquid the cantilever has to also move the surrounding liquid, causing a reduced resonance frequency with broadened peak. Also the deflection is not symmetric anymore. The oscillation is mainly distorted on the bottom, but this leads to the fact that the cantilever oscillation cannot be approximated with a sinusoid anymore. Thus the contribution of higher eigenmodes to the excitation have to be taken into account [37]. How all these factors influence the resonance behavior of cantilevers is displayed in Fig. 17. The left image shows a normal cantilever in a normal air environment. The resonance peak is very thin and distinct. The right image is the tuning curve of a liquid-imaging cantilever in a NaC buffer solution. The resonance curve shows a multitude of peaks, of higher modes. The resonance curves are very specific for the cantilever and they can differ strongly for two cantilevers even if they are from the same batch. Depending on the imaging liquid, the sample, the temperature and the cantilever different peaks yield different results.

Fig. 17: Tuning curves of different cantilever. Left: soft cantilever for tapping mode (in dry environemnt). Right: cantilever in liquid for tapping mode in liquid.

The main additional forces in liquid are the double layer forces. They arise when a surface is charged. Then the surface attracts oppositely charged ions from the solution which gather at it. The clustered ions form a charged layer on the surface with an electrostatic potential which decays exponentially.

It can be generally said that if the imaging liquid is of greater ionic strength the tip will undergo less electrostatic repulsion. In literature it is suggested to add small quantities of salt to shield the tip from buffer influences [38].

3.6.4.5 Other modes

Owing to the AFMs versatility there are a multitude of other modes, this is just an excerpt:

- Chemical force microscopy (CFM: chemically modified tips for mapping chemical groups
- Electrostatic force microscopy (EFM): qualitative changes of surface potential and polarizability
- Magnetic force microscopy (MFM): mapping of magnetic domains
- Conductive AFM (CAFM): mapping of current through sample and tip
- Kelvin probe microscopy (KPFM): quantitative changes of surface potential
- Lithography
- …

Many more measurement possibilities arise from combining AFM with other methods. This is a short list of combinations which are commercially available:

- Raman – AFM
- SEM – AFM
- AFM – Langmuir Trough
- Cryo-AFM
- ….

4   Mechanical and IT design

This chapter is about the mechanical construction and the software which was developed in the course of this thesis. The first part of this chapter is a detailed description of an oil bath which was developed to enable sample preparation within a steady surrounding. The second part is on the database which was developed to keep the samples clearly organized.

4.1   Oil bath

The oil bath was developed in order to provide a steady and well defined environment while the cellulose is dissolved in the ionic liquid (see chapter 5.1.2 for more details on the preparation process).

The oil bath is shown in Fig. 18 (left) and its inlet in Fig. 18 (right). The inlet is put into the oil bath to stabilize the sample vials. The oil bath is filled with oil and put on a magnetic stirrer with integrated heating. The filled sample vials are easily pushed through a Styrofoam inlet (see Fig. 18 left) which insulates and keeps the vials from tilting. The cover has a hole where a PT-100 temperature sensor can be fit through which gives the heating plate feedback on the oil temperature.
The bottom of the oil bath is kept very thin in order to not have too much distance between the magnetic stirrer and the sample vials. The sample vials "float" in the oil, allowing a constant and uniform temperature. Six sample vials can fit once, enabling the preparation of six different samples with the same settings at the same time.

For the technical drawings please see Appendix A.

Fig. 18: The oil bath with sample vials and cover (left) and its inlet (right).

4.2 Sample database

This project (as is the case with most projects) is faced with the organizational problem of long sample preparation times and several people working on it at once. A database was developed in order to be able to keep track of the samples and the steps they go through while being processed.

4.2.1 Key points

The database was programmed in Microsoft Access. The structure was designed according to the task at hand and the main elements are displayed in Fig. 19:

Sample management
- Unique sample numbers/name (automatic sample name suggested)
- Sample progress traceable
- Searchable by any parameter
- Documents can be attached
- Mixtures can be entered
- Sample description standardized

Backup management
- Automated regular backups
- Entire database backuped

User management
- Log-in
- Assignable permissions
- User name automatically tracked with sample entry

FELMI-ZfE integrated
- Project number is recorded

Fig. 19: Cornerstones of the database.

4.2.2 User-Interface and database structure

A screenshot of the sample data entry screen is displayed in Fig. 20 exemplarily for the entire database system. The unique sample description can be seen among others at the top, as well as attached documents in the table on the bottom.

For the database structure please see Appendix A.

Fig. 20: Screenshot of the sample of the database data entry screen.

5 Preparation of nanoflat cellulose substrates

Every scientific process relies on reproducibility. This automatically leads to the necessity of reproducible specimen if they are to be used for investigations. But also the process of production, the method of measurement, goals trying to be achieved by these measurements and external precepts can be determining parameters in sample preparation.

In the case of this work it was the goal to produce tunable cellulose samples which allow the AFM supported in situ visualization of enzymatic degradation. For these investigations the samples are required to be nanoflat for two reasons. The profane one is that the AFM is limited to a maximum height-difference of approximately 7μm. The second reason is measurement related – the flatter a sample is the easier it is to detect change of topology, morphology and texture. Certainly a homogeneous sample is also preferable, as homogeneous samples increase the reproducibility strongly.

Producing adequate and reproducible substrates can be quite difficult, especially when dealing with unknown processes during the production. The manufacturing process used by Ganner, Dohr and coworkers is based on [16], [41] but contains some factors of uncertainty.

This chapter will first explain the manufacturing process used before and then will go into detail about the changes introduced, and what happened to the substrate due to these changes. The chapter will finish with a short description of the preparation of spin cast cellulose which is an easy and fast to produce test substrate.

5.1 Preparation of standard cellulose samples

This chapter lays out the preparation method used for the standard cellulose samples before modifications have been applied.

5.1.1 Previous method of preparation

The procedure for sample preparation as described here is based on the work of Judith Dohr [42].

The base material for the samples is microcrystalline Avicel PH101 (further denoted as Avicel). In short, the production is as follows:
The Avicel is dissolved in an ionic liquid and dried. Then a fractional solvent exchange is carried out to remove the ionic liquid. The final step is embedding the substrate in epoxy and then cutting it with the ultramicrotome.

The main states and the processing steps that lead from one state to another are displayed in Fig. 21.
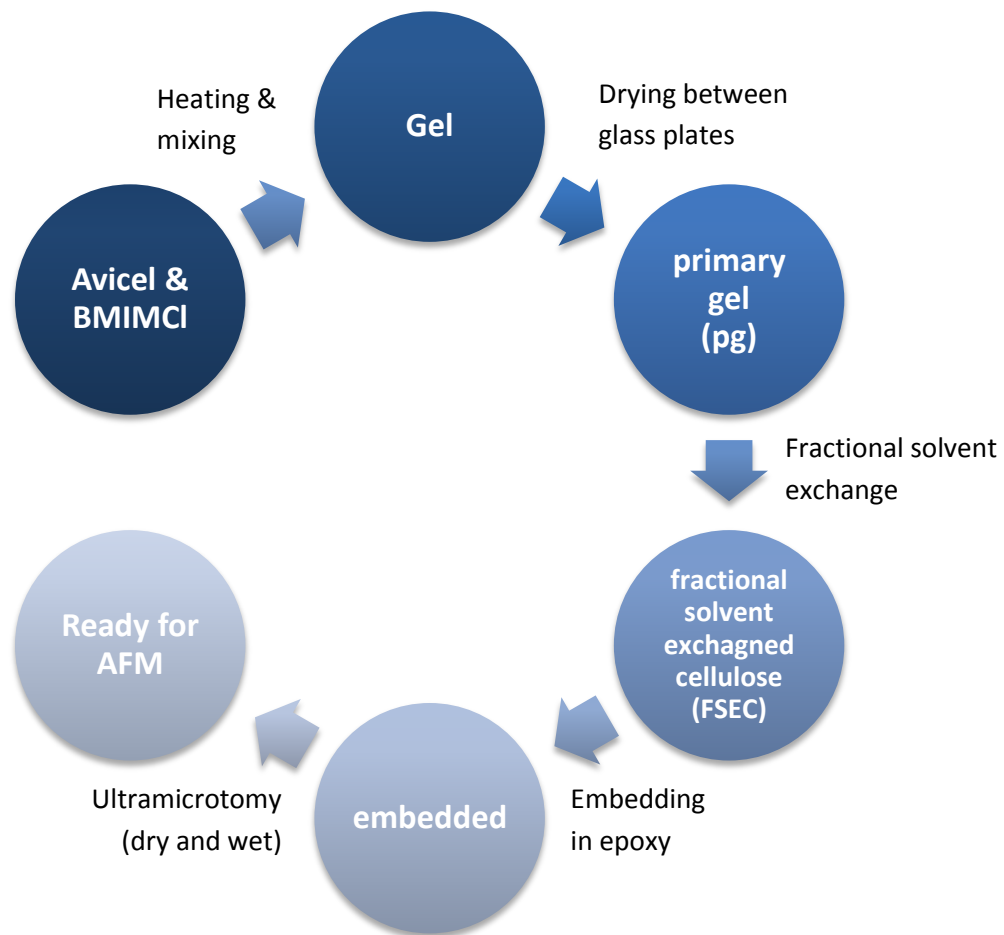
Fig. 21: Flow chart of the main states and the processing steps of the samples during preparation.

i) Heating and mixing:

Ionic liquid is put into a Petri dish and then placed on a heating plate at 100°C until liquid. Then up to 15 wt. % Avicel is added slowly into the Petri dish and the solution is stirred for 24 hours at which point the mixture is supposed to be a completely blended and very viscous gel (see chapter 2.2 for more information on cellulose dissolution in ionic liquids).

ii) Drying;

In this step the gel is pre-dried between to glass plates as is shown in Fig. 22. Separation plates left and right of the gel insure a uniform thickness. After one week of pre-drying the primary gel can be removed. The primary gel is still very soft and formable, but not liquid anymore (Fig. 25 middle).
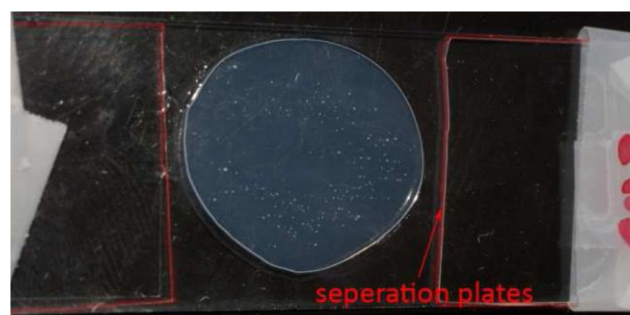
Fig. 22: Primary gel between glass plates [24].

iii) Fractional solvent exchange:

The fractional solvent exchange is a multistep exchange process to remove the ionic liquid from the sample. The primary gel is cut into fragments and then the solvent exchange is performed with varying water/ethanol ratios as suggested by Dohr [42]. The exact procedure is shown in Table 2. The resulting fragments are very hard, rigid and distorted (see Fig. 23) and are called fractional solvent exchanged cellulose (FSEC) from here on.

Table 2: Protocol of the fractional solvent exchange on cellulose fragments.

Ethanol concentration	Fragment exchange time
30 % EtOH	15 min
50 % EtOH	15 min
70 % EtOH	30 min
70 % EtOH	30 min
80 % EtOH	30 min
90 % EtOH	30 min
90 % EtOH	30 min
100 % EtOH	30 min
100 % EtOH	30 min

Fig. 23: Cellulose fragments after fractional solvent exchange [24].

iv) & v) Embedding in epoxy & Ultramicrotomy

The following explanation follows the graphical depiction in Fig. 24. Before the ultramicrotomy can be performed the fragments are embedded in an epoxy. The epoxy is pre-cut with a milling machine to reduce the cutting surface. Then a pre-cut is performed to expose the cellulose cross section. In the next step the cellulose cross section is exposed to the buffer solution to allow swelling. Finally the last ultramicrotome cut is performed with an oscillating diamond knife that has a liquid trench. Done this way the sample is constantly wetted. This process yields nanoflat surfaces with very low roughness. It should be noted that the distorted fragments complicate ultramicrotomy intensely as the embedment is not evenly distributed, leading to many fragments breaking out of the epoxy.
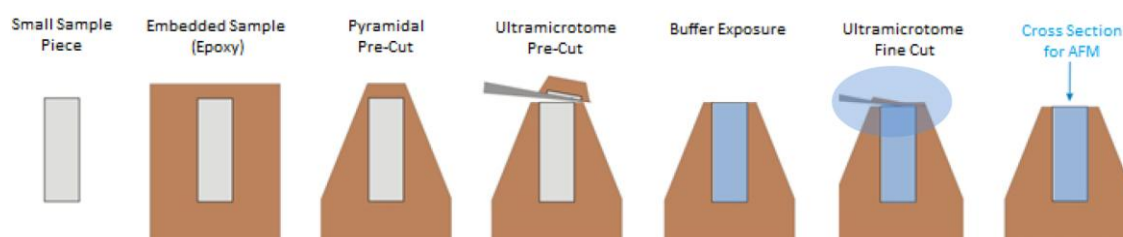
Fig. 24: Cellulose ultramicrotomy sample preparation [42].

5.1.2 Improvements

A major problem in the sample preparation was that the results were always varying, depending on various unknown factors. Therefore some improvements to the sample preparation were introduced.

i) Heating and mixing
The first problem identified was found in the heating and mixing of the Avicel with the BMIMCl. Previously this was done in an open Petri dish. This results in two main problems. The surrounding environment can influence the mixing, as for example water (humidity) reduces the solubility of BMIMCl drastically [13]. Furthermore it is not entirely sure to which temperature the gel is actually heated, as the heating plate cannot hold the temperature at exactly 100°C.

In order to prevent these problems an oil bath has been designed (see chapter 4.1). A PT-100 temperature sensor can be attached to the heating plate, controlling the oil temperature more precise. Also environmental influences can be avoided as the samples are stirred in closed sample vials.

ii) Drying
This process has only been altered minimally. The glass plates are now heated to the gel temperature before the gel is applied.

iii) Solvent exchange
This step has also been improved. The solvent exchange itself is done as before, but on whole flakes of primary gel (see Fig. 25 left and middle) instead of fragments. Letting the samples air dry after the solvent exchange yields crumpled and distorted flakes, which are difficult to process in ultramicrotomy. Therefore the cellulose flakes are put between pulp-free wipes which are drenched in Ethanol (Fig. 26) and weighted down. This allows the samples to dry slower. The result is again a very stiff and rigid cellulose flake, but it is extremely flat (Fig. 25 right). The native surface is even flat enough to allow AFM imaging on it without any further preparation like ultramicrotomy (chapter 6.6.1)

Fig. 25: Cellulose substrates; primary gel (left and middle) and FSEC (right).
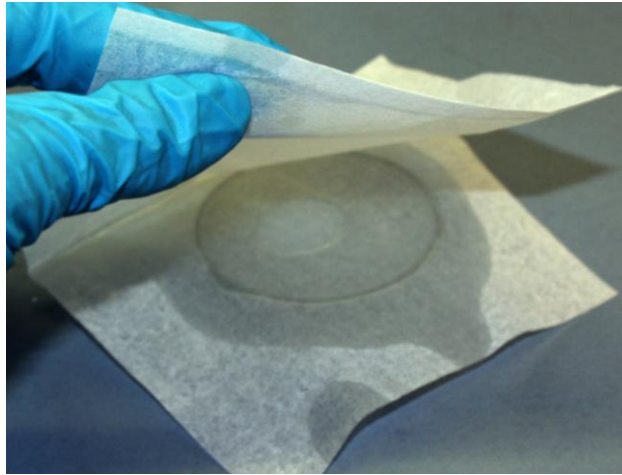
Fig. 26: Cellulose flake after solvent exchange and before last step of drying.

5.2 Preparation of spin cast cellulose

Spin cast cellulose substrates were started to be used as an alternative to the samples introduced above. They are fast and easy to produce, and are therefore predestined as testing substrate. Since they are already nanoflat by the production process (spin-coating) they can be used in the LC-AFM without the need of ultramicrotomy. Even though at the moment the substrate consists of only very amorphous cellulose 2 (for more information on the properties see chapter 6.7), it is thinkable to spin several layers with different properties to get versatile samples [43].

Some of the samples which we investigated were received from Ao.Univ.-Prof. Mag. Dr.rer.nat. Robert Schennach from the Institute of Solid State Physics, TU Graz, Austria. Others were made in-house by DI Thomas Ganner. They were produced by dissolving trimethylsilyl cellulose (TMSC) in Xylol and spin casting it on a sample carrier (e.g. silicon wafer). The layer thickness can be controlled by the ratio of TMSC to its solvent and by spinning multiple films over one another. The thin films are then exposed to HCl vapor which substitutes the trimethylsilyl by a proton with the result of regenerated cellulose [43].

Further information on manufacturing and properties can be found in [44], [45].

6 Characterization of cellulose

In order to tune cellulose samples one has to be able to characterize them. This chapter describes various ways of characterization and shows results for samples which were prepared as explained in chapter 5.1.2. This will lead to a clear understanding of the samples properties and how they can be adjusted according to ones needs.

6.1 X-ray diffraction

XRD is an easy, straight forward and relatively fast method for measuring samples as discussed in more detail in chapter 3.2. Applied on cellulose it allows to get results for a sample's cellulose type as well as for its crystallinity index (chapter 2.1). The spectra of cellulose 1 and cellulose 2 are clearly distinguishable [2], [46]. In addition the crystallinity degree of each cellulose type can be calculated with different methods [47], [48], [49]. Of course each of these methods has advantages and disadvantages, some are quite complex to calculate or need standardized samples to compare. But the main problem which occurs in these calculations is that the derived crystallinity degree varies widely even for one sample. Park et. al [47] compared three methods and reported the crystallinity index of Avicel PH-101 to be between 60.6 % and 91.7 %, depending on the method of calculation. This leads to the conclusion that qualitative tendencies can be found by directly comparing spectra of different samples even though XRD cannot be used for exact quantitative results with cellulose.

The measurements in this chapter are aimed at clarifying the properties of cellulose as it is processed during its preparation for AFM in-situ investigations. The measurements have been conducted in between all preparation steps to understand the processes and structural changes the samples go through, starting with microcrystalline Avicel cellulose and ending with comparing different FSECs.

6.1.1 Microcrystalline cellulose Avicel

The XRD-spectra of microcrystalline Avicel (Fig. 27) was taken in order to characterize the starting material and understand the changes it goes through during the processing. The spectrum was taken from 10° - 60° with an increment of 0.02° and a step dwell time of 3 seconds.
The reference spectra of cellulose 1 and cellulose 2 are also displayed in Fig. 27; they are taken from the Master thesis of Judith Dohr [42]. The Avicel cellulose is mainly of the type cellulose 1, but partly amorphous.
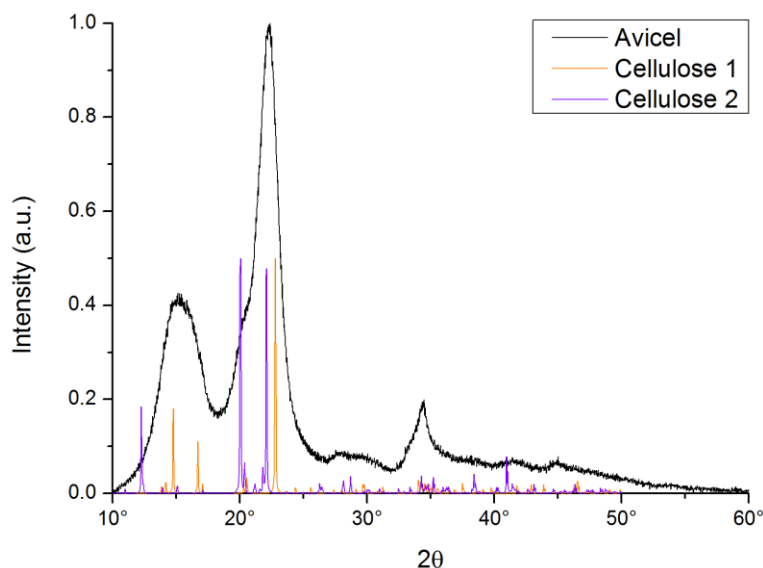
Fig. 27: XRD-spectra of microcrystalline Avicel cellulose.

6.1.2 BMIMCl on mica

The determination of the spectra of the ionic liquid BMIMCl is quite important as it is a crucial part of the sample preparation with the cellulose being dissolved in it.

In the purpose of recording the spectra some BMIMCl was heated and a drop was spread on mica. This substrate was chosen because the ionic liquid has a relatively high surface tension and was difficult to measure on standard surfaces like SiO_X or glass. In contrast, mica shows a very high surface polarity which is highly beneficial in this case. The spread droplet was then analysed in the XRD (Fig. 28). Mica is very strongly crystalline ordered which causes very intense peaks. The scan was interrupted in the vacancy of these peaks to avoid damage of the X-ray detector. Especially interesting is the peak around 25° which partly coincides with the main peaks of cellulose 1 and cellulose 2.
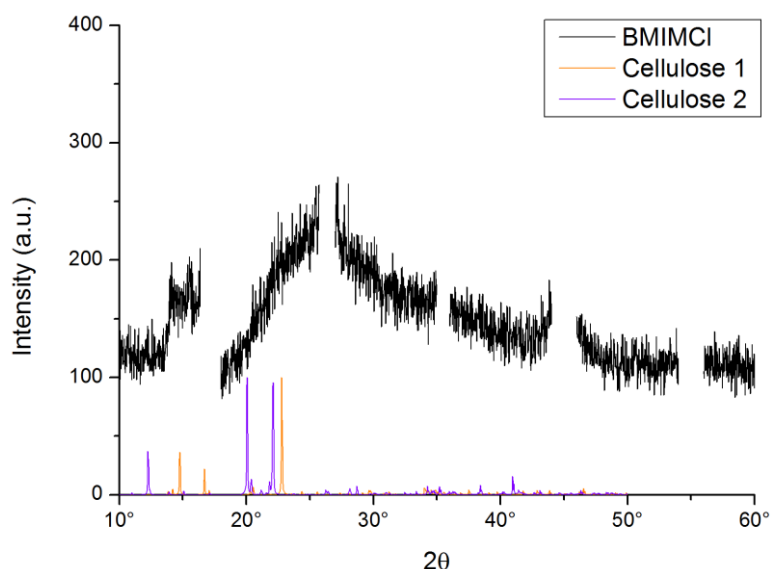
Fig. 28: XRD-spectra of BMIMCl on mica in comparison with cellulose 1 and cellulose 2 main peak positions.

6.1.3   Primary gel: long time gel forming process of a single side gel

In the process of producing the samples the heated cellulose - ionic liquid mixture is wedged between two glass plates and then left for a week. During this time a not completely understood gelation process takes place (chapter 5.1.2). The measurements in this chapter were conducted to get an improved structural understanding for these gelation processes including possible recrystallization and / or phase changes.

A drop of a 14 wt. % gel was applied on a glass substrate. This was done at that point in the manufacturing process where typically the gel would be dried between glass plates. The drop was subjected to XRD measurements at varying time intervals to investigate the temporal evolution. However, this sample (single side gel) was exposed significantly longer to the environment than the usually prepared samples (standard gels and PGs). Therefore, the results are not entirely comparable. Nevertheless, the measurements give a good idea of what is going on during drying when considering the spectra in Fig. 29. The small horizontal shift of the main peaks at 25° (downward-pointing left arrow) is not significant enough to allow a profound argumentation, but a big influence in this peak is from the IL (chapter 6.1.2). This peak decreases as the time passes, possibly indicating a decomposition of the ionic liquid. The peak at 35° (upward pointing right arrow) grows with time and corresponds with the quarter length of one cellobiose and comes most likely from the ordering along the direction of the fibres. It thus depends on the fibrillar alignment into chains and the length of these crystals (along the crystal axis: (004)) [49], [50].
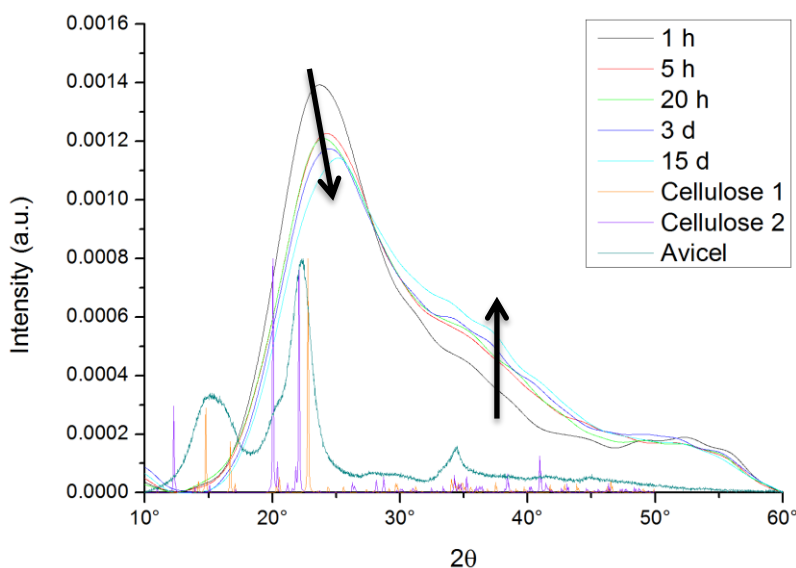
Fig. 29: XRD-spectra of a single side gel over a longer time period.

6.1.4   Primary gel: comparing a single side gel with standard PG

Since the normal samples are not as much in contact with the ambient air, it was of interest to find out if the results of the measurements described in chapter 6.1.3 are significant for the normal samples. The comparison of spectra of the single side gel (14 wt. %) and the standard PG (14 wt. %) can be seen in Fig. 30. Eventually, the differences are actually quite conspicuous. A major problem, in addition to the problem of interaction with the surrounding environment, which negatively influences this measurement and especially the comparability, is the surface of the samples. While the standard PG has a very flat surface, the single side sample has a strongly curved surface as it has

been applied as a drop on the glass carrier. Nevertheless one can deduce that a recrystallization is taking place while the sample is drying.
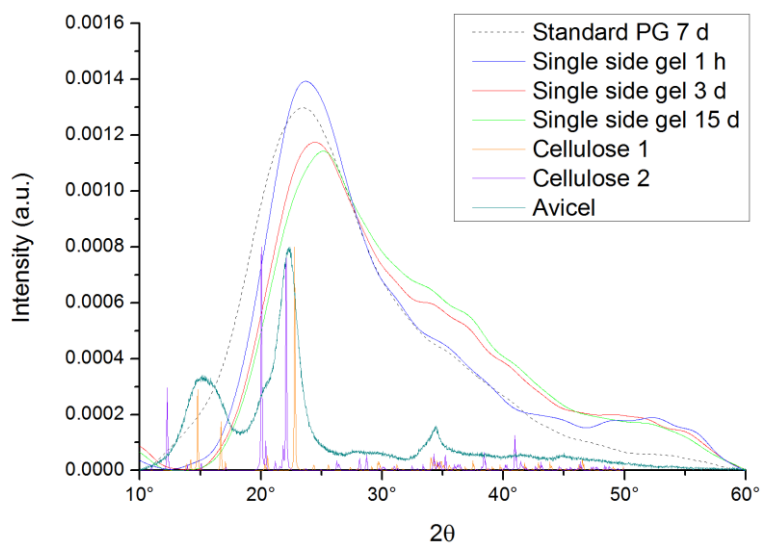
Fig. 30: XRD-spectra of standard PG and single side gel.

6.1.5   Primary gel: comparing low (4 wt. %) and high concentration (14 wt. %)

Measurements comparing primary gels of 4 wt. % and 14 wt. % were conducted in order to further investigate the difference of mixtures. The XRD-spectra in Fig. 31 indicate a shift from cellulose 2 to cellulose 1 as the amount of Avicel in the mixture rises. The spectrum of the PG 14 wt. % is higher at an angle of 15° which concurs with the double peak of cellulose 1 in that region. At an angle of 35° the spectrum of the PG 14 wt. % shows a shoulder, due to a small peak. This peak indicates longer crystals in the higher concentrated gel [49], [50]; it also coincides with a peak of Avicel. The main peak at 22° shifts to the right for lower concentration, because of the higher ionic liquid concentration in that sample. These findings suggest, that the 14 wt. % primary gel contains longer crystals, i.e. probably undissolved Avicel. These findings of undissolved cellulose can also be found in literature [13].
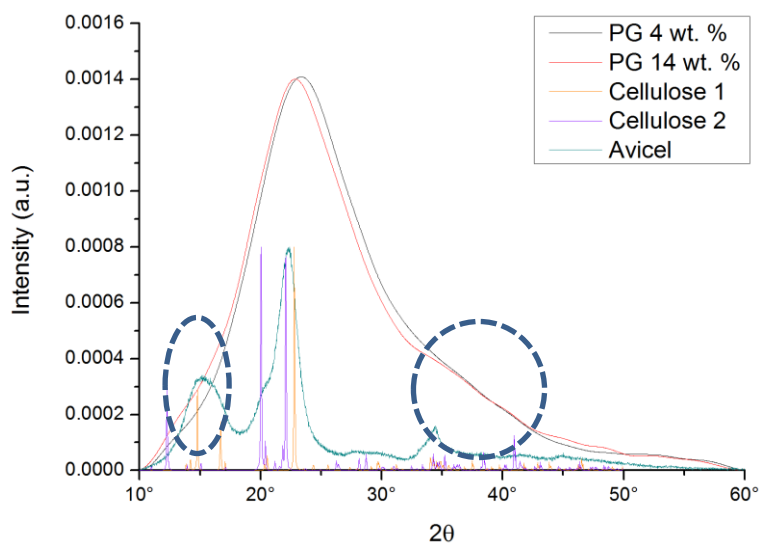
Fig. 31: XRD comparing 4 wt. % and 14 wt. % primary gels. Left circle: double peak of cellulose 1. Right circle: peak at 35° indicates larger crystal length.

6.1.6   Solvent exchange: comparing low (4 wt. %) and high concentration (14 wt. %)

An important step in the process of producing the samples is the fractional solvent exchange (as described in chapter 5.1.2). In this process the ionic liquid is removed from the primary gel by a multistep procedure with varying water/ethanol ratios. When the samples have dried from the last step in the solvent exchange they are hard and brittle. The measurements in this chapter where done to shed some light on the changes the samples go through during the solvent exchange.

The samples were scanned before the solvent exchange, every few steps during the process and after the solvent exchange. In the steps closer to the end of the process the samples started to dry while taking the XRD-spectra. To prevent the sample from rolling up it was cut into squares of approximately of 2x2 mm after the solvent exchange step with 50 % Ethanol. These smaller flakes rolled up too, influencing the measurement negatively – however, much less than if one tried to do the measurement on one whole piece.

The XRD-spectra of the PG 4 wt. % and of the PG 14 wt. % are shown in Fig. 32 and Fig. 33, respectively. The black arrows show the direction of the solvent exchange process. A major problem with these spectra was finding a proper way of normalization in order to compare them. As a straightforward approach we normalized the spectra to the main peak with the consequence that absolute variations are inaccessible while relative interpretations are valid.

For the PG 4 wt. %, which is shown in Fig. 32, the spectra develop a peak around 40° for the first few steps. In the next few steps ranging from 50 % over 70 % to 90 % these peaks become much more distinct and the spectra reveal furthermore another highly defined peak around 21° while the central peak related to the IL is strongly decreasing. The spectrum shows a clear absence of cellulose 1 as the main peak is clearly over the main cellulose 2 peaks and there is a local minimum at 35° (which would not be the case for cellulose 1). All these findings indicate that the sample consists mainly of cellulose 2.
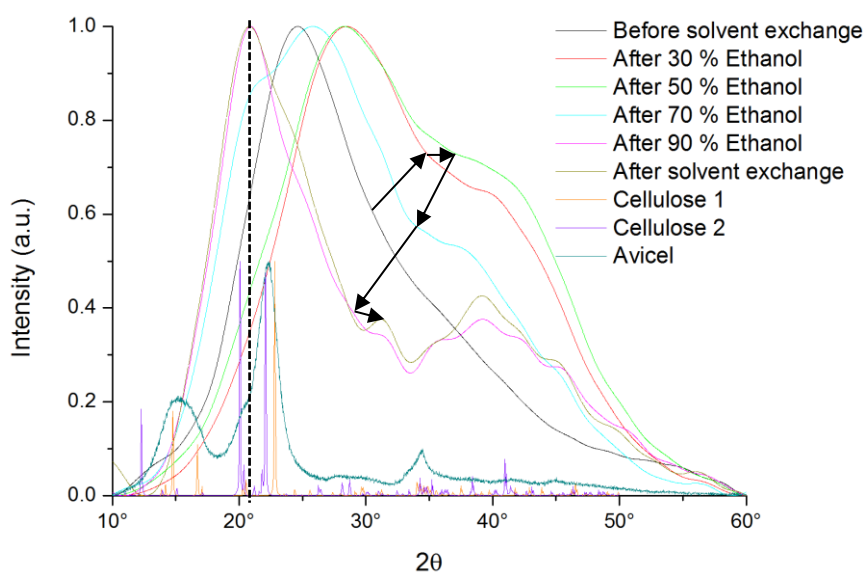
Fig. 32: XRD-spectra of the fractional solvent exchange of a 4 wt. % PG.

The PG 14 wt. % is displayed in Fig. 33. It is similar to the one described above, with the main peak of the spectra first shifting to the right and then further to the left than they had started out. Nevertheless the structure of the sample seems to stabilize a lot faster with the spectra moving way less in the later steps than they did for the 4 wt. % PG. During the solvent exchange the spectra develop a peak around 40° like the previous sample. Also the main peak shifts to about 21°, but is slightly further to the right than the FSEC 4 wt. %, indicating that probably some cellulose 1 is in the sample.
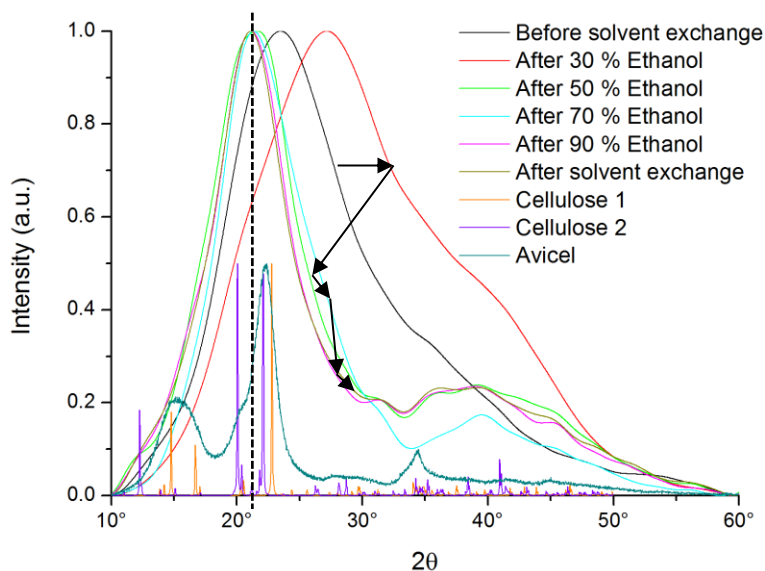
Fig. 33: XRD-spectra of the fractional solvent exchange of a 14 wt. % PG.

6.1.7 FSEC: overview from 4 wt. % to 14 wt. %

In the XRD-measurements above it has become evident that the samples change their composition when the mixture-ratio is changed. Depending on the literature the maximum cellulose that can be dissolved in BMIMCl, with the procedure as described in chapter 5.1.2, is supposed to be between 6 wt. % and 15 wt. % [13], [16].

For our measurements samples were prepared in steps of 2 wt. % from 4 wt. % to 14 wt. % in order to find out if and how the samples change for different mixing ratios. The results are displayed in Fig. 34. It has to be noted, that the dotted spectra of the FSEC 12 wt. % was recorded with a different X-ray diffractometer (*Siemens D5005 X-ray Diffractometer*) and therefore the comparison of intensities with the other spectra is only possible to a certain extent. Our results support Mazza [13] who found that the cellulose is only dissolvable until approximately 8.75 wt. % by turbidity measurements. For higher concentrations the cellulose is not fully dissolved but partly dispersed in the ionic liquid. Nevertheless, the spectra of the 10 wt. % sample shows no noticeable change compared to the lower concentrations, while for the samples of higher concentration the main peak around 23° becomes stronger which indicates cellulose 1. Furthermore, there is a distinct broadening around 15° visible which also indicates the presence of cellulose 1. These two clear changes suggest strongly the existence of cellulose 1 in our samples.
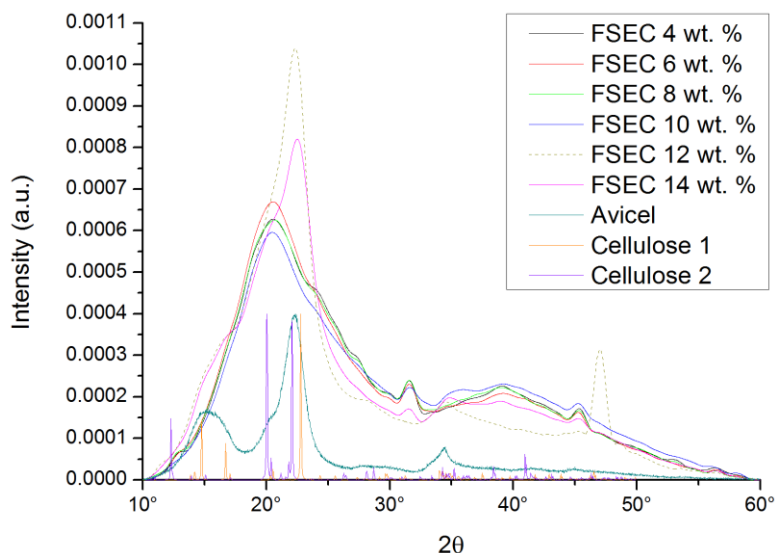
Fig. 34: XRD-spectra of FSEC with varying wt. %.

6.1.8 FSEC: comparing stirring times: 4 wt. % and 14 wt. % - 24 h vs. 68 h

One major problem of the samples is the spatial homogeneity. The samples originally produced were stirred for 24 hours. Such stirring times are usually sufficient for samples of low concentration but as the concentration rises and as the cellulose is not fully dissolved, the final samples are then not fully homogenous after 24 hours (see chapter 5.1.2 for method of preparation and sample pictures, see chapter 6.2 for optical microscope images of homogenous/heterogeneous PGs and FSECs). In avoidance of these distribution problems the samples were stirred longer (68 hours) resulting in improved homogeneity.

The comparison of FSECs of low and high concentration and for different stirring times is displayed in Fig. 35. It shows longer stirring time influences the cellulose quite strongly. The main aspect is that the long stirred cellulose seems to be more amorphous than the short stirred one. As the main peaks become lower and broader. But still the 14 wt. % 68h sample seems to contain more cellulose 1 in comparison to the spectrum of the 4 wt. % 68h FSEC.
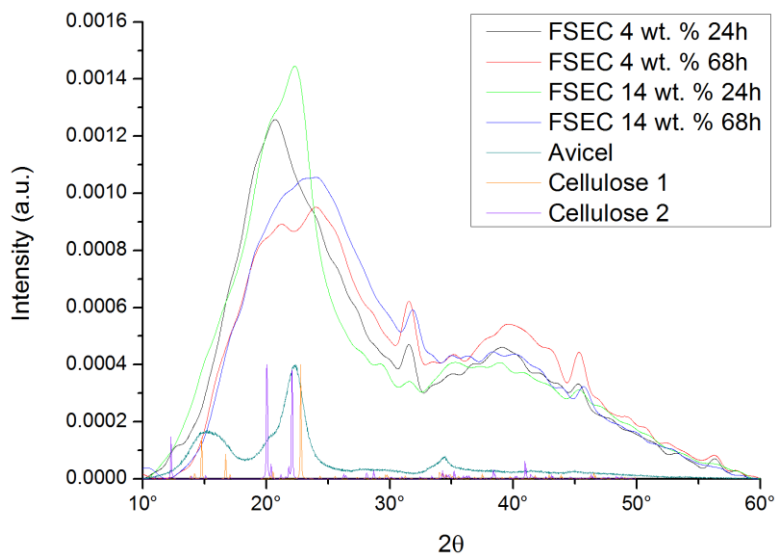
Fig. 35: XRD-spectra of FSEC with varying wt. % and varying stirring time.

6.2 Optical microscopy

The optical microscope is the easiest way to obtain images from samples. In order to get information on the composition and homogeneity of samples images from primary gels and FSECs which have been prepared by ultramicrotomy will be compared in this chapter. Images of native FSEC samples revealed no interesting results and are not displayed in this work.

6.2.1 Primary gel: Dissolving & Dispersion

As mentioned above, the mixing ratio of cellulose and ionic liquid influences the properties of the samples. High concentrations (above 10 wt. %) of Avicel cellulose are thought to be not fully dissolved by the ionic liquid. Fig. 36 shows the optical microscope image of a 4 wt. % 24 h and Fig. 37 is an image of a 14 wt. % 68 h primary gel. Both images are typical for such samples.

It can be seen, that in the low concentration sample (Fig. 36) no residues are left and the gel is homogeneous. The black and light circles (indicated by red arrows) are air bubbles in the gel.

In the high concentration sample (Fig. 37) a high number of small crystals can be seen (a few are highlighted by red arrows). Up to this point it can only be assumed that these small crystals are undissolved Avicel cellulose (of the type cellulose 1), which would agree with the results found in chapter 6.1. Anticipative it can be said, that the results of chapter 6.3 confirm this assumption fully.
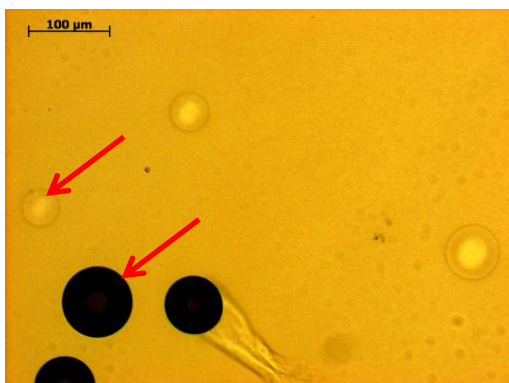
Fig. 36: Image of a 4 wt. % 24 h PG. Red arrows indicate air bubbles.
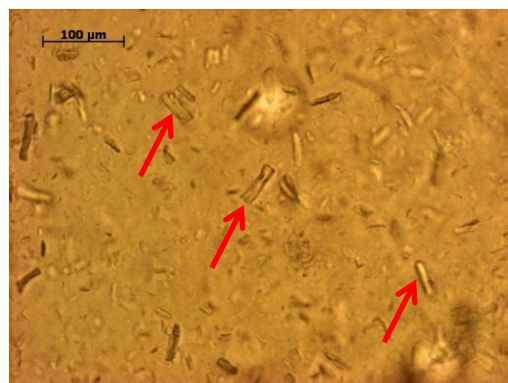
Fig. 37: Image of a 14 wt. % 68 h PG. Red arrows indicate crystals.

6.2.2 Distribution in dependence of the stirring duration

In chapter 6.1.8 the differences between short stirring and long stirring duration have been investigated with XRD. In this chapter the same is done via optical microscopy. Fig. 38 and Fig. 39 show images of the same primary gel with short and long stirring duration, respectively. These gels then went through the rest of the manufacturing process. As FSECs they were embedded in epoxy and cut in liquid with the ultramicrotome. The images of these cross-cuts are displayed in Fig. 40 for short and in Fig. 41 for long stirring duration.

Short stirring duration:
The optical microscopy image of short stirred PG (Fig. 38) shows areas of agglomerated crystals (indicated with A) and areas where the PG is homogeneous and no crystals can be seen (indicated

with B), suggesting that the Avicel in these regions has been fully dissolved. The ultramicrotome cut was performed in a region with an agglomeration. This region is clearly crystalline as can be seen in the image of the cut (Fig. 40) and is mainly undissolved Avicel (see chapter 6.3)

Long stirring duration:
The image of a long stirred PG (Fig. 39) shows none of these agglomerations. The crystals (three are indicated by black arrows) are evenly distributed over the entire sample which results in an ultramicrotome-cut (Fig. 41) which is a lot smoother than for the short stirring duration.
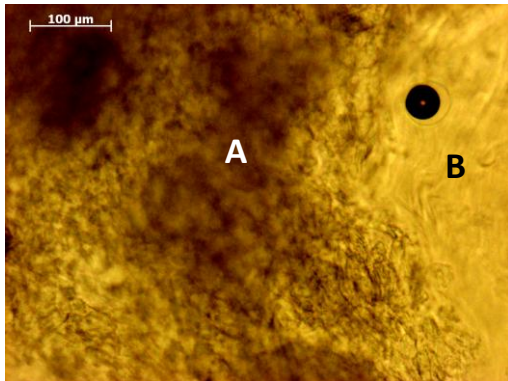
**Fig. 38: Image of a 14 wt. % 24 h PG.
The A indicates agglomerated crystals,
the B indicates homogeneous gel.**
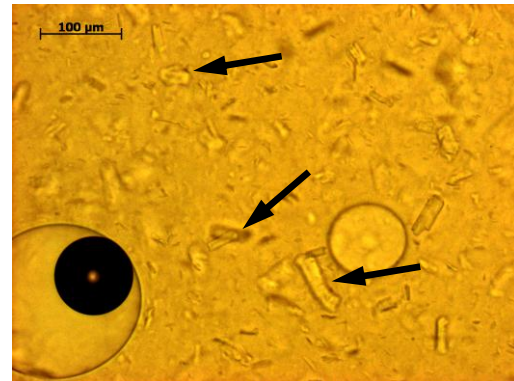
**Fig. 39: Image of a 14 wt. % 68 h PG.
The arrows indicate crystals.**
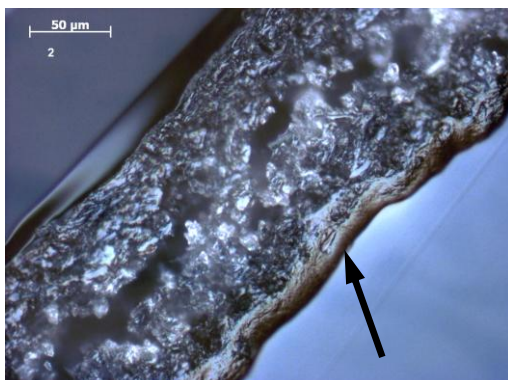
**Fig. 40: Image of a 14 wt. % 24 h FSEC, embedded in
epoxy. The arrow indicates the FSEC.**
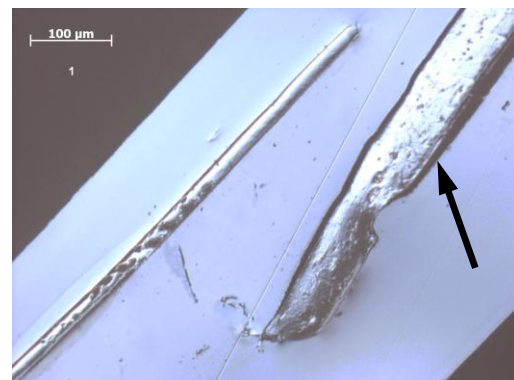
**Fig. 41: Image of a 4 wt. % 68 h and 14 wt. % 68 h FSEC,
embeddedin epoxy. The arrow indicates
the 14 wt. % 68h FSEC.**

In low concentration samples the Avicel is fully dissolved, leading to a clear gel. Higher concentrations cannot be fully dissolved resulting in a dispersion of crystals in the gel. The stirring time influences the homogeneity of the sample strongly. Short stirring time leads to agglomerations of crystals, while in long stirred samples the undissolved crystals are dispersed evenly over the sample.

6.3 Raman spectroscopy

Raman-spectroscopy is a straight-forward method for characterizing samples with respect to their chemical signature. For cellulose it allows retrieval of information on the band assignments [51], lattice structure [52], degree of crystallinity [53], quantitative analysis of the polymorphic modifications cellulose 1 and cellulose 2 [54], amorphous structure [52]. Raman-spectra of the ionic liquid BMIMCl can also be found in literature, further information can be found in reference [55].

In our investigations we mainly wanted to determine the structure (crystallinity, polymorphism, etc.) of the samples. For receiving quantitative measurements of the crystallinity it would be necessary to have well defined standardized samples to compare with – which are very complicated to establish and widely absent in the scientific field. Therefore, this chapter concentrates on obtaining qualitative results on the samples polymorphs. As with the previous investigations, samples from 4 wt. % to 14 wt. % have been examined. This chapter will start with comparing spectra of cellulose 1 and cellulose 2, discussing which peaks are usable for evaluating polymorphism and why this is possible. Then evaluations of various spectra will give a cellulose 1 / cellulose 2 ratio and the chapter will finish with a comparison of the newly obtained samples with the samples used in this project prior to this work.

6.3.1 Introduction: distinguishing between cellulose 1 and cellulose 2

The typical spectra of cellulose 1 and cellulose 2 can be found easily in the corresponding literature. Fig. 42 shows the Raman-spectra of both polymorphs. Also the typical frequencies for each polymorph are depicted graphically.
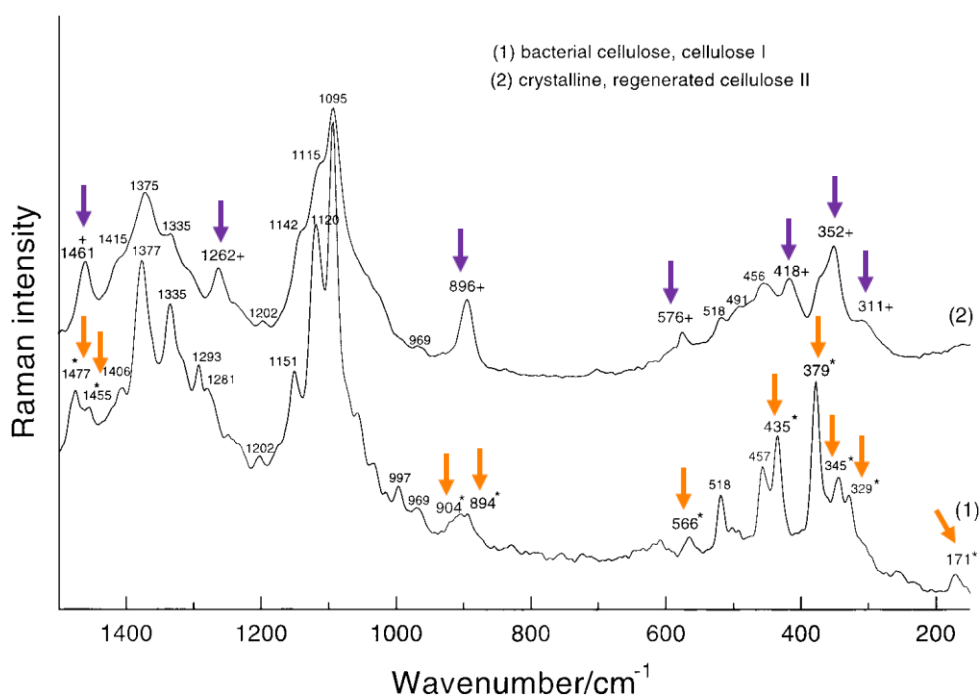
Fig. 42: FT-Raman spectra of cellulose polymorphs in the range 1500 - 150 cm^{-1} (typical frquencies highlighted: cellulose 1 (* and orange arrows), cellulose 2 (+ and purple arrows) [56].

The Raman frequencies of cellulose 1 and cellulose 2 and their vibrational assignments are listed in Table 3. The column on the right indicates if the peaks have been used for further evaluation and in which context (evaluation was conducted in two ways).

Table 3: First three columns: FT-Raman frequencies and their vibrational assignment for cellulose 1 and cellulose 2 in the range 1500 – 150 cm^{-1} [56]. Column on the right: These bands have been used for further evaluations.

Cellulose 1 Bacterial cellulose (cm^{-1})	Cellulose 2 Regenerated cellulose (cm^{-1})	Approximate assignment of the vibrational modes	Used for further evaluation
1476m∗		δ (CH$_2$) scissors	
	1461m+	δ (CH$_2$) scissors	
1455w∗		δ (CH$_2$) scissors and δ (COH)	
1406w	1415sh	δ (CH$_2$), δ (HCC), δ (HCO), δ (COH)	
1377ms	1373ms	δ (CH$_2$), δ (HCC), δ (HCO), δ (COH)	
1335m	1335mw, sh	ω (CH$_2$), δ (HCC), δ (HCO), δ (COH)	
1318 sh	1307 sh	ω (CH$_2$), δ (HCC), δ (HCO), δ (COH)	
1293w		ω (CH$_2$), δ (HCC), δ (HCO), δ (COH)	X (6.3.2)
1281 sh		ω (CH$_2$), δ (HCC), δ (HCO), δ (COH)	
	1262mw+	τ (CH$_2$), δ (HCC), δ (HCO), δ (COH)	X (6.3.2)
1251 vw, sh		τ (CH$_2$), δ (HCC), δ (HCO), δ (COH)	
1234 vw, sh		τ (CH$_2$), δ (HCC), δ (HCO), δ (COH)	
1202 vw	1202 vw	τ (CH$_2$), δ (HCC), δ (HCO), δ (COH)	
1151m		v (CC), v (CO) ring breathing, asymmetric	
	1142m, sh	v (CC), v (CO) ring breathing, asymmetric	
1120ms	1115ms, sh	v (COC), glycosidic; ring breathing, symmetric	X (6.3.3)
1095 vs	1095 vs	v (COC), glycosidic; ring breathing, symmetric	X (6.3.3)
	1042 vw, sh	v (CC), v (CO)	
1035 vw, sh		v (CC), v (CO)	
	1023 vw, sh	v (CC), v (CO)	
997w		ρ (CH$_2$)	
969 vw	969 vw	ρ (CH$_2$)	
904w, sh∗∗		δ (C(1) H(β))	
894 vw	896 mw++	δ (C(1) H(β))	
609 w		τ (CCH)	
	576 w+	δ (COC) ring	
556 w*		δ (COC) ring	
518 mw	518 w, sh	δ (COC) glycosidic	X (6.3.2)
502 vw		δ (COC) glycosidic	
493 vw	491 vw, sh	δ (COC) glycosidic	X (6.3.2)
457 mw	456 mw	δ (CCC), δ (CCO), ring deformation	
435 m*		δ (CCC), δ (CCO), ring deformation	
	418 mw+	δ (CCC), δ (CCO), ring deformation	
379 m*	373 mw, sh	δ (CCC), δ (CO), δ (CCO), ring deformation	
	352 m+	δ (CCC), δ (CO), δ (CCO), ring deformation	
345 mw*		δ (CCC), δ (CO), δ (CCO), ring deformation	
329 w*		δ (CCC), δ (CO), δ (CCO), ring deformation	
	311 w, sh+	τ (CCO)	
258 vw, sh		τ (COH)	
171 vw*		τ (COH)	
*+Frequencies are most suitable for following the polymorphic transformation of cellulose 1 (.) into cellulose 2 (+). **++Band shape is suitable for following the polymorphic transformation of cellulose 1 (**) into cellulose 2 (++).			

6.3.2 FSEC: cellulose 1 / cellulose 2 - ratio for different mixtures: integrative comparison of selected peaks

Raman spectra of FSECs in steps of 2 wt. % from 4 wt. % to 14 wt. % were taken in order to characterize the samples regarding there cellulose 1 and cellulose 2 content. In order to do this the spectra of each sample where recorded and significant peaks (for the cellulose polymorphs) were then selected to be integratively compared with each other. Two characteristic FSEC Raman spectra of cellulose 1 and cellulose 2 and the enlarged peaks, which were chosen for comparison, are displayed in Fig. 43. The red spectra is taken from a white spot of an inhomogeneous FSEC 14 wt. % that had be stirred for 24h (see crystalline agglomeration in Fig. 38) and which corresponds to a cellulose 1 spectrum. The black spectrum is taken from a FSEC 4 wt. % and matches a cellulose 2 spectrum.
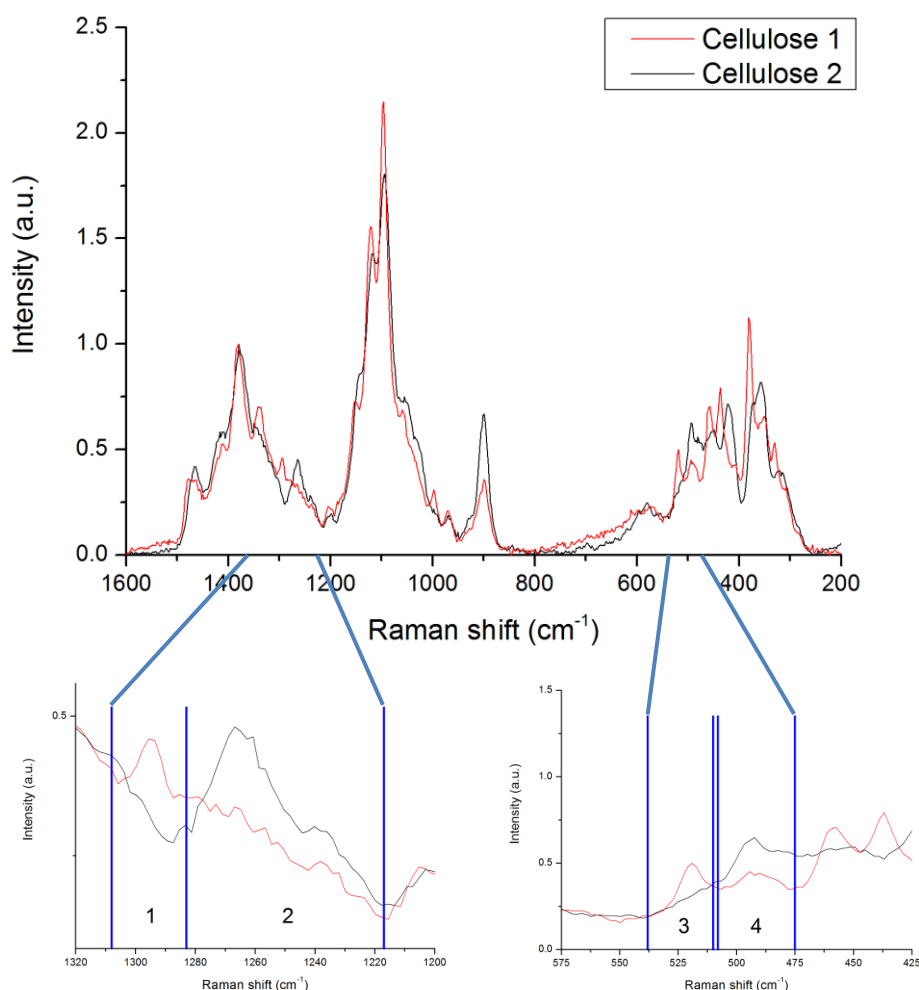
Fig. 43: Characteristic Raman spectra for cellulose 1 and cellulose 2 in FSECs, and the selected areas for further evaluation in this chapter.

Measurements of Avicel (microcrystalline cellulose 1) have also been conducted. Two characteristic spectra can be seen in Fig. 44. In comparison to the spectra in Fig. 43 the intensity rises strongly in the low frequencies due to fluorescence. Therefore only the peaks marked 1 and 2 were evaluated integratively.
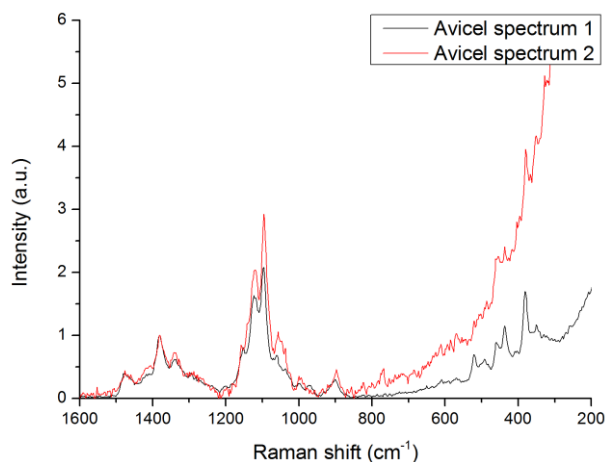
Fig. 44: Raman spectra of Avicel cellulose.

The relevant integrated areas of the Raman spectra were then set in relation to each other to enhance the significance of the results and plotted as a function of the wt. % of the sample (Fig. 45). The ratio is calculated for the vertical axis to correspond to the cellulose 1 / cellulose 2 ratio in the sample. From this it follows, that the samples with low concentration consist of only cellulose 2. At approximately 10 wt. % the samples start to include cellulose 1. Higher concentrations result in higher cellulose 1 content in the samples. This supports the findings up to here: in low concentrated samples the cellulose is fully dissolved and is in the polymorph cellulose 2 phase after regeneration (fractional solvent exchange). The maximum limit of dissolution is at approximately 8 wt. %. After this limit the cellulose is not fully dissolved in the gel wherein the residual Avicel cellulose (of the type cellulose 1) is dispersed. After regeneration the samples consist of cellulose 1 and cellulose 2.

For longer stirred samples (68 h) the differences between 4 wt. % and 14 wt. % equal out a bit more, probably because more of the cellulose is dissolved in a more homogeneously mixed gel. Avicel is far above the other values, as it consists only of the polymorph cellulose 1.
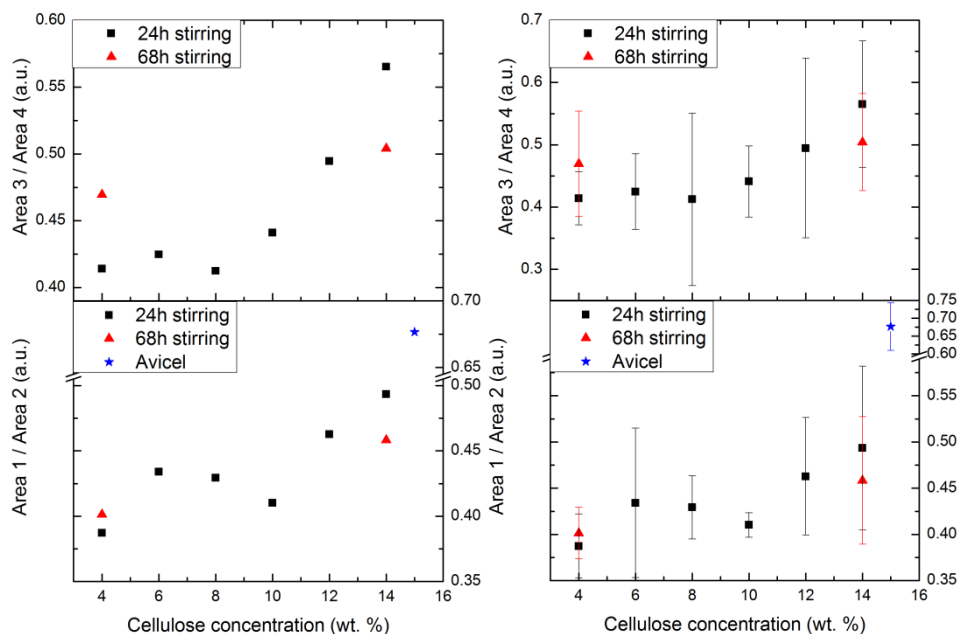
Fig. 45: Ratios of the areas from the Raman spectra for samples with different wt. %. Area ratios are equivalent to cellulose 1 / cellulose 2 – ratio. Left: without error. Right: with error.

An analysis of the deviation of the considered areas for integration between spectra of each sample is shown in Fig. 46. The comparable strong deviation of the results can be explained with inhomogeneity of the samples (compare with error bars in Fig. 45). The low concentration samples are more homogeneous and therefore show less deviation. Under 10 wt. % the deviation is relatively low. For higher concentrated samples the deviation rises strongly, indicating strong inhomogeneity. The rising deviation further supports the idea of undissolved Avicel in the sample. Pure Avicel shows a very low deviation and a strong homogeneity. It can be concluded, that longer stirring of high concentrated samples reduce their inhomogeneity.
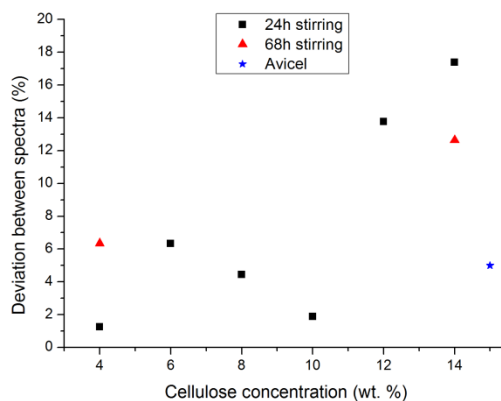
Fig. 46: Deviation between selected areas of Raman spectra for each analysed sample.

6.3.3   FSEC: cellulose 1 / cellulose 2 - ratio for different mixtures: peak ratio

The same spectra (6 samples from 4 wt. % to 14 wt. %) as in the previous chapter (6.3.2) were used for evaluation. Unlike before, the calculation now compares the height of two peaks (after a three point baseline was subtracted and the spectra were normalized). In measurements done by Schenzel et. al it can be seen, that the ratio of the peaks change, depending on the ratio of cellulose 1 to cellulose 2 [54]. The selected peaks are shown in Fig. 47.
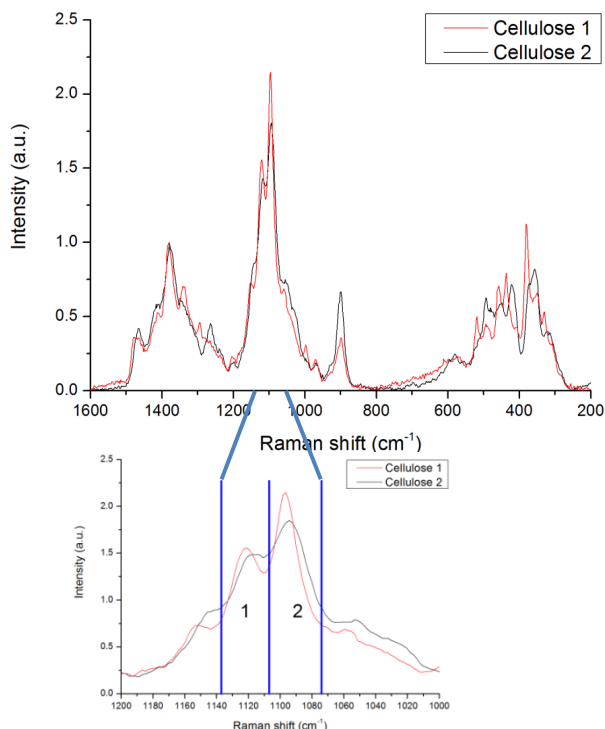
Fig. 47: Characteristic Raman spectra for cellulose 1 and cellulose 2; and the two peaks selected for further evaluation in this chapter.

The higher peak was divided by the lower one, number 2 and 1 in Fig. 47. respectively. The results are displayed in Fig. 48. Again they confirm the theory of fully dissolved Avicel turning into cellulose 2 for low concentrations. At higher concentrations cellulose 1 can be found in the samples, indicating undissolved Avicel crystals in the sample. As this evaluation is less reliable as the one above (chapter 6.3.2) the results diverge more (as can be seen especially for FSEC 12 wt. %).
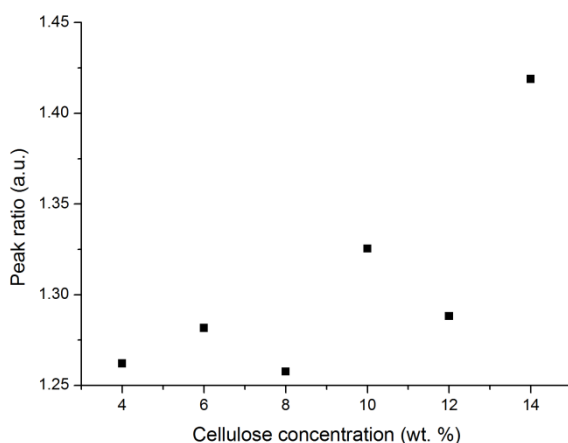
Fig. 48: Peak-ratios from the Raman spectra for samples with different wt. %.

6.3.4   Mapping

Mapping of a part of a FSEC 14 wt. % was carried out due to the known spatial inhomogeneity also reflected in the strong deviations in Fig. 45. For this the spectra were compared and the result can be seen as map. In Fig. 49 the left image is an optical microscope image with the superimposed

mapping, the right image shows the mapping in larger resolution. The spectra that were selected for the mapping can be seen in Fig. 50.

The reason that the difference between cellulose 1 and cellulose 2 can be identified so easily is definite proof that the two polymorphs can be clearly distinguished with Raman spectroscopy. Furthermore, the map shows a cellulose 1 crystal embedded in a cellulose 2 matrix and provides further evidence for a solubility limit and undissolved Avicel crystals being the source of the cellulose 1 in high concentration samples.
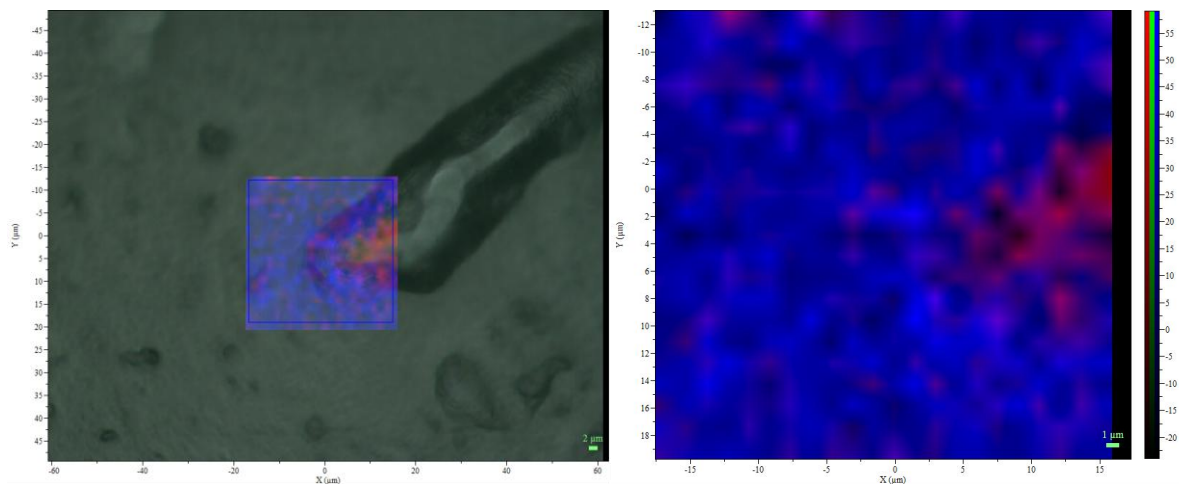
Fig. 49: Left image: optical microscope image with superimposed map. Right image: Mapping of the selected region.
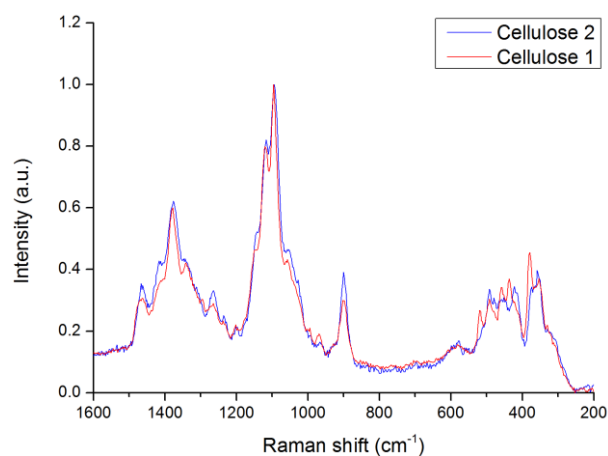
Fig. 50: Raman spectra: the selected spectra for mapping.

6.3.5   Comparing standard FSEC with samples produced by Judith Dohr (14 wt. %)

Raman measurements were also conducted on samples produced by Judith Dohr [42] in order to make a transition to the samples used in her and Thomas Ganners' [24] master thesis. These samples were not produced in the very same way as the ones in this thesis, the process is described in chapter 5.1.1. Two spectra of Judith Dohrs sample are compared with the spectra of two new samples and are displayed in Fig. 51. FSEC 14 wt. % is characteristic for cellulose 1 and FSEC 4 wt. % for cellulose 2. Both curves have a relatively good overlap, indicating that the previously used samples are inhomogeneous, and consist of both cellulose polymorphs.
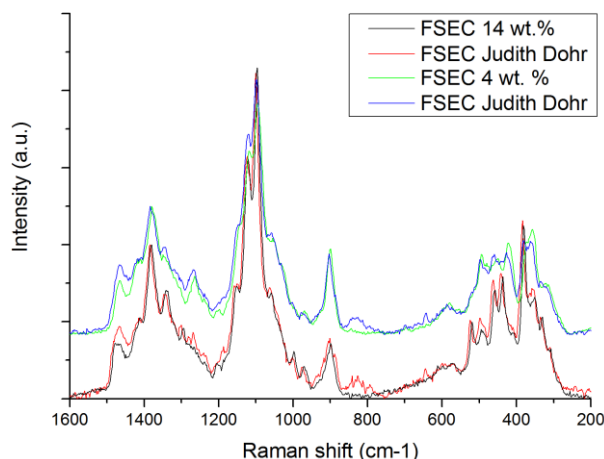
Fig. 51: Raman spectra: comparing new samples with Judith Dohrs samples.

6.3.6   Why Raman and not IR?

Raman spectroscopy has some major advantages over IR spectroscopy, even though in cellulose all vibrational modes are potentially Raman- and infrared-active. With Raman spectroscopy the low-frequency region is easily observed, while causing difficulties in infrared spectra. Furthermore, systems with high polar bonds (e.g. water) have intense infrared bands, but weak Raman intensity due to the relatively low polarizability. This leads to water nearly not influencing the Raman spectra of cellulose. Lastly, cellulose is often optically heterogeneous and scatters light strongly. In IR spectroscopy it is problematic when processes other than absorption cause attenuation of the beam. Scattering losses varying with the frequency over the IR region are caused by the refraction index going through large changes near absorption bands. For Raman spectroscopy these refraction index changes do not present a problem because the excitation frequencies and absorption bands are far from each other [51].

6.4   Scanning electron microscopy

Scanning electron microscopy allows morphological (shape, size, etc.) and chemical (via X-ray analysis) characterization. A major problem is that the samples have to be conductive or at least coated to avoid charging. Alternatively the sample can be metal shadowed or stained [57]. Another approach is the ESEM (environmental SEM) which releases the SEM of the restraints of high vacuum and even allows measurements in a changeable atmosphere. But the ESEM has the drawback of resolution loss.

During this work FSEC samples were embedded, cut with Ultramicrotomy and then coated with carbon to view with a SEM, but no clear and reliable results could be obtained due to the mentioned reasons.

6.5   Transmission electron microscopy

This method enables the investigation of ultra-thin specimen. In cellulose shapes and size distribution of microfibrils and crystalline nanoparticles can be retrieved with this method [57], [58]. The difficult part about these measurements is the preparation of the thin samples as the resolution of the TEM can be limited by the sample thickness. Different methods have been reported in the literature. Kirshnamachari et. al [57] prepared the sample in a way that the cellulose whiskers were embedded in a latex matrix which resulted in sufficient contrast. Elazzouzi-Hafraoui et. al [58] used negative staining and cryo-TEM for their investigations of crystalline nanoparticles.

This chapter concentrates on obtaining quantitative results of the crystal size and distribution in the FSEC samples. Again specimen from 4 wt. % to 14 wt. % (in steps of 2 wt. %) have been examined. The ultrathin cuts which are necessary for TEM investigations were prepared by staining with Ruthenium and ultramicrotome-cutting in liquid with an oscillating diamond knife.

6.5.1   Preliminary investigations

The goal of the preliminary investigations was to find out if it was possible to distinguish FSEC 4 wt. % and FSEC 14 wt. % with the TEM and the applied staining method. The results can be seen in Fig. 52. The left image (FSEC 4 wt. %) shows only very little spots compared to the right image (FSEC 14 wt. %). If assumed that these black spots are cellulose crystals then this further promotes that high concentration samples consist of undissolved Avicel crystals (cellulose 1) embedded in a cellulose 2 matrix. Above all it shows that measurements with the TEM are probably possible.
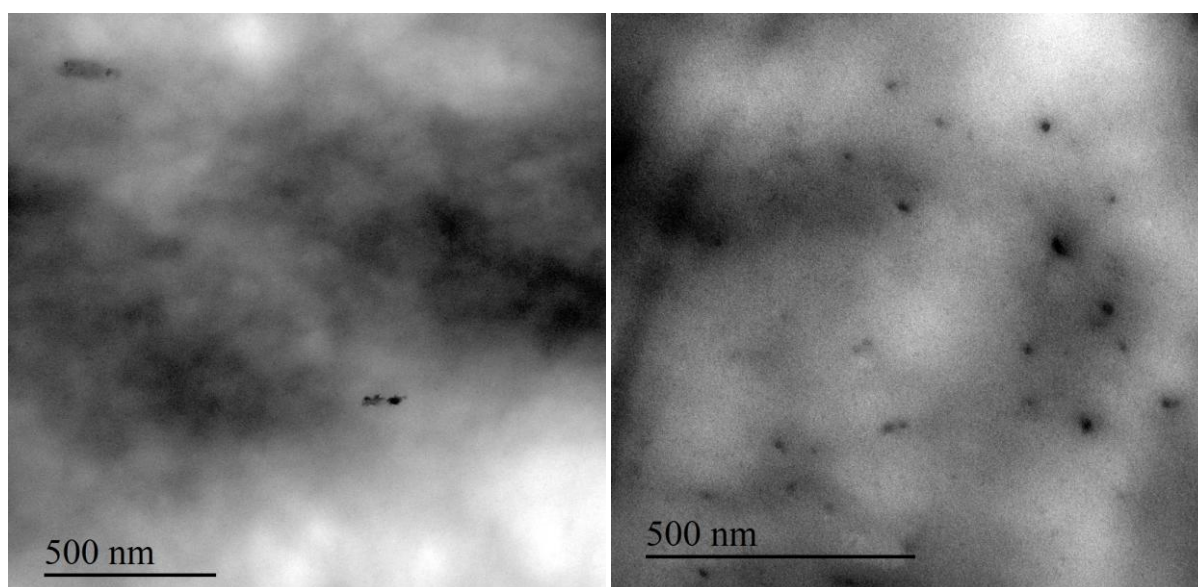
Fig. 52: TEM images of FSEC 4 wt. % (left) and FSEC 14 wt. % (right). Black points are cellulose crystals.

High-resolution images (Fig. 53) of these black spots were taken. The black spots clearly show lattice fringes (green arrows), confirming that the black spots are of crystalline nature. With these results it is clear that the TEM is a suitable method for evaluating particle /crystal distribution in the samples.
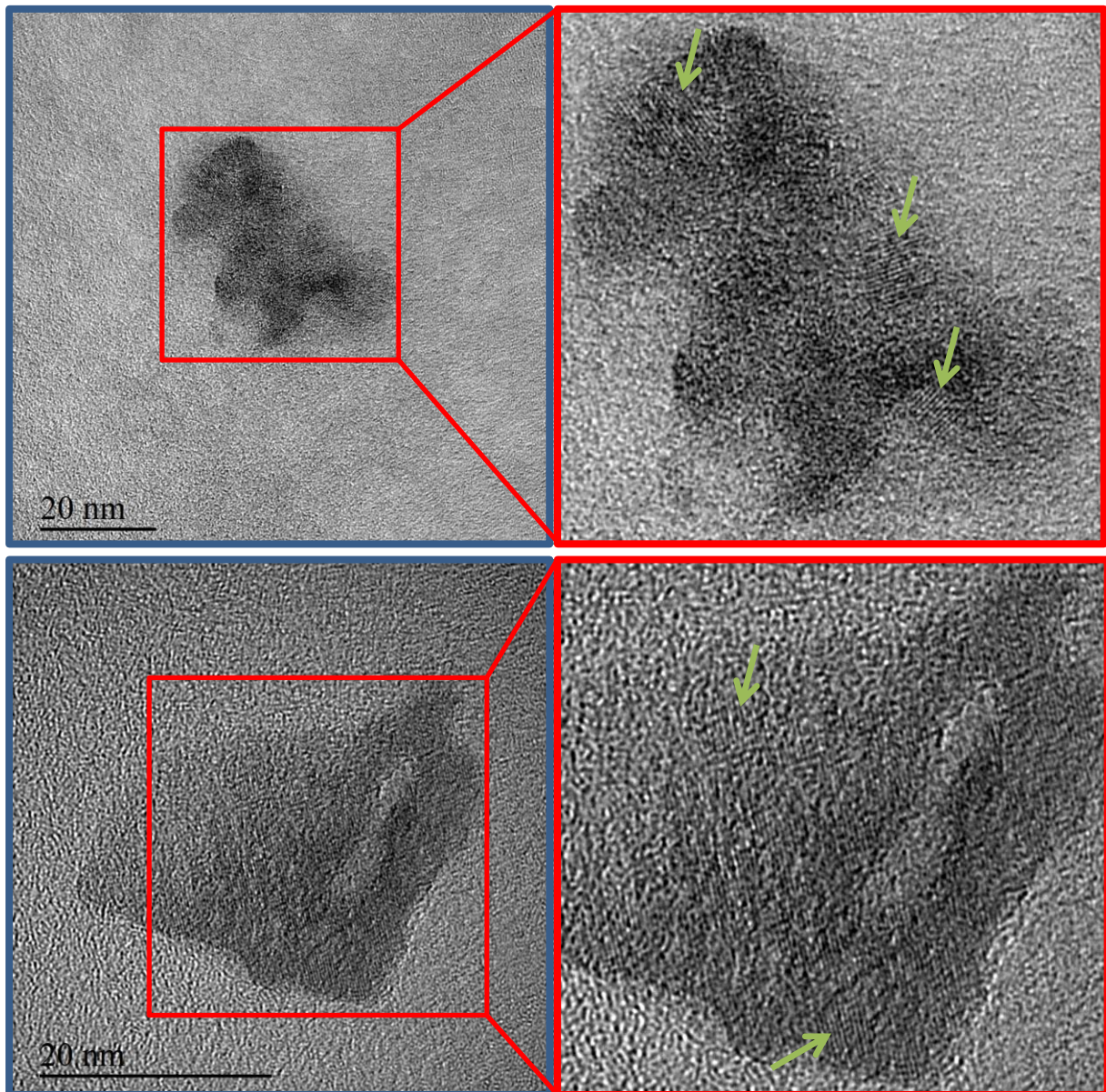
Fig. 53: High-resolution TEM images of two cellulose crystals. Left: recorded image. Right: enlarged images showing lattice spacing. Green arrows indicate areas with visible lattice spacing.

6.5.2 Crystal distribution in FSECs: overview from 4 wt. % to 14 wt. %

After receiving the positive results of the preliminary investigations a complete set of FSEC samples from 4 wt. % to 14 wt. % (in steps of 2 wt. %) was prepared for measurements. Images were recorded with the TEM and then evaluated graphically for particles / crystals. The result is shown in Fig. 54. Unfortunately the evaluation of the FSEC 12 wt. % was not successful, but the others yielded interesting results. The particles per µm² stay relatively constant for low concentrations. At 10 wt. % the concentration starts to rise slightly. The FSEC 14 wt. % shows a high particle density, indicating

relatively large number of undissolved Avicel crystals in the sample. This entirely supports and confirms all findings in previous chapters. The comparison with the Raman based characterization of the cellulose 1 / cellulose 2 ratio (Fig. 45) reveals a strong agreement. This suggests that the small crystals observed via TEM are cellulose 1, meaning an increasing crystalline content as expected.
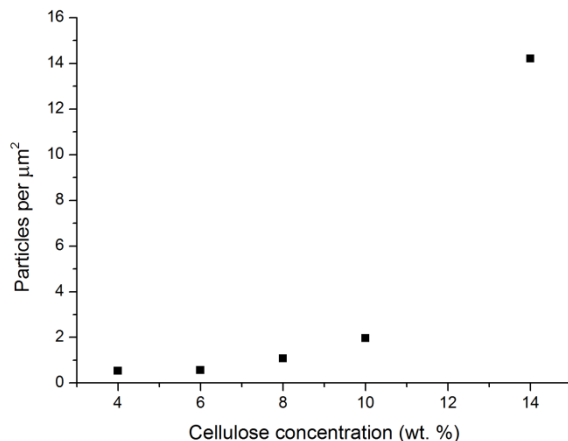
Fig. 54: Particles per µm² for samples with different wt. %. Evaluated from TEM images.

6.6 Atomic force microscopy

Evaluating AFM-images for sample characteristics like crystal size, crystal distribution, etc. is always risky of not being representative, as the images only show small regions of the surface. This is especially problematic when the samples are inhomogeneous. For homogeneous samples it can be used to confirm results of measurements conducted by other means [58].

The specimens undergo an embedding process and cutting with the ultramicrotome as they are supposed to be ultra-flat for the in-situ visualisation of enzymatic degradation. After this the samples might have a thin film of smeared cellulose due to the process of cutting. So the first step was to look at the native surface of the samples. Then cross sections were evaluated in dry environments and finally in the liquid cell.

6.6.1 Native surface measurements of FSEC in dry environment

The revised preparation process of the cellulose samples generates very flat samples. They are flat enough to allow AFM-measurements of their native surface (Fig. 55). The height images of the FSEC 4 wt. % reflect the finer structured surface compared with the FSEC 14 wt. %. The phase images show this even more. The phase image of FSEC 4 wt. % also shows some brighter spots which could indicate a different crystal phase or contamination. Nevertheless the surface is not representative for the cut samples, as it is not entirely clear what happens to the surface during the manufacturing. The native surface of the FSEC is therefore not suited for characterizing the samples, embedding, ultramicrotome-cutting and viewing the cross section is necessary to further investigate sample properties.
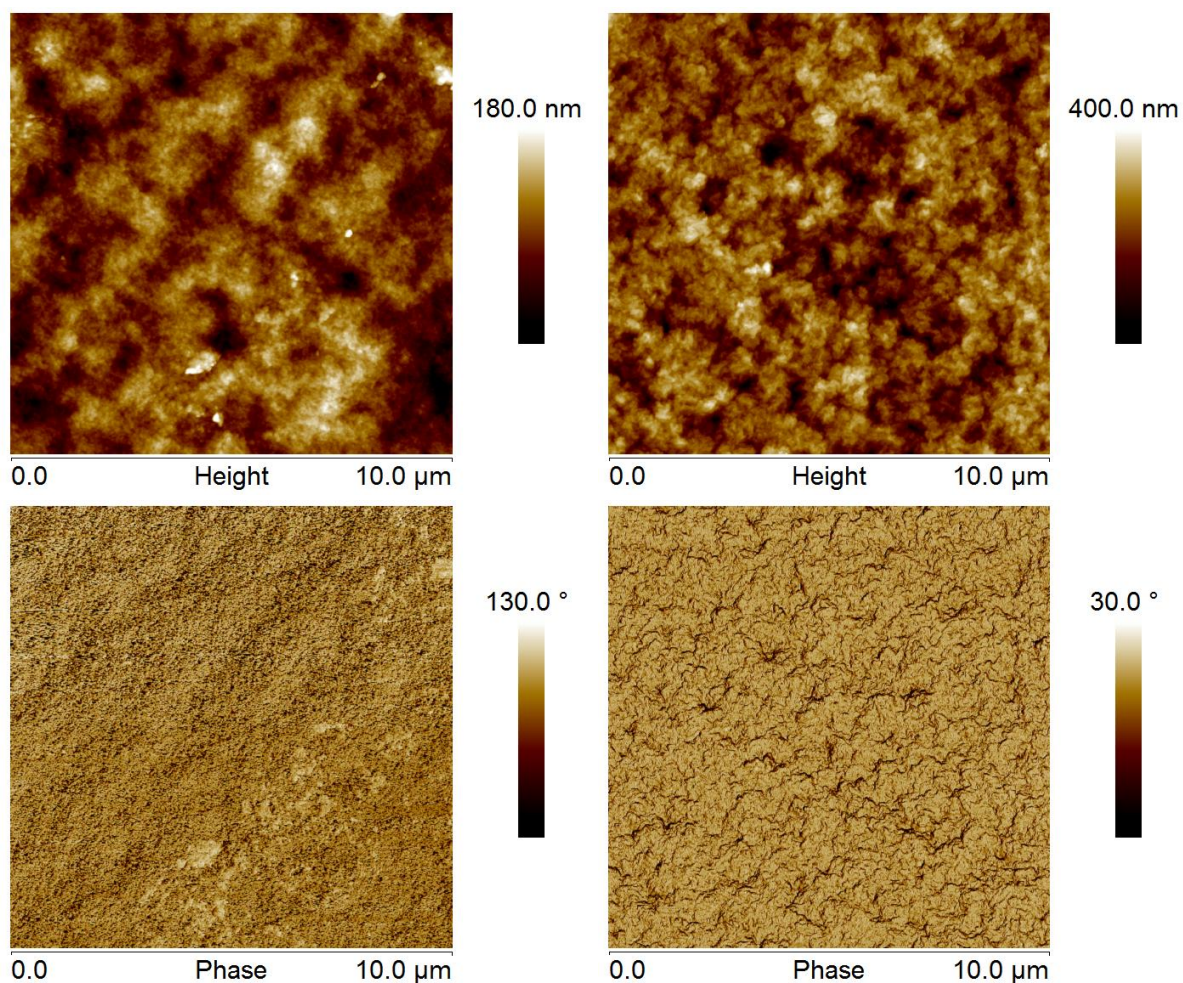
Fig. 55: 10 µm AFM height images (top) of the native surface of FSEC 4 wt. % (left) and FSEC 14 wt. % (right). The respective phase images are below.

6.6.2 Dry ultramicrotome cuts in dry environment

Three samples (FSEC 4 wt. % 24 h, FSEC 14 wt. % 24 h, FSEC 14 wt. % 68 h) were embedded in resin and prepared for AFM imaging. The corresponding height and phase images are displayed in Fig. 56. The height images show the direction the samples were cut, a preferential direction is visible. The phase images (at the right) display a finer structure for the low concentration and the long stirred sample than for the high concentration short stirred one, indicating a finer structure and smaller crystallites.
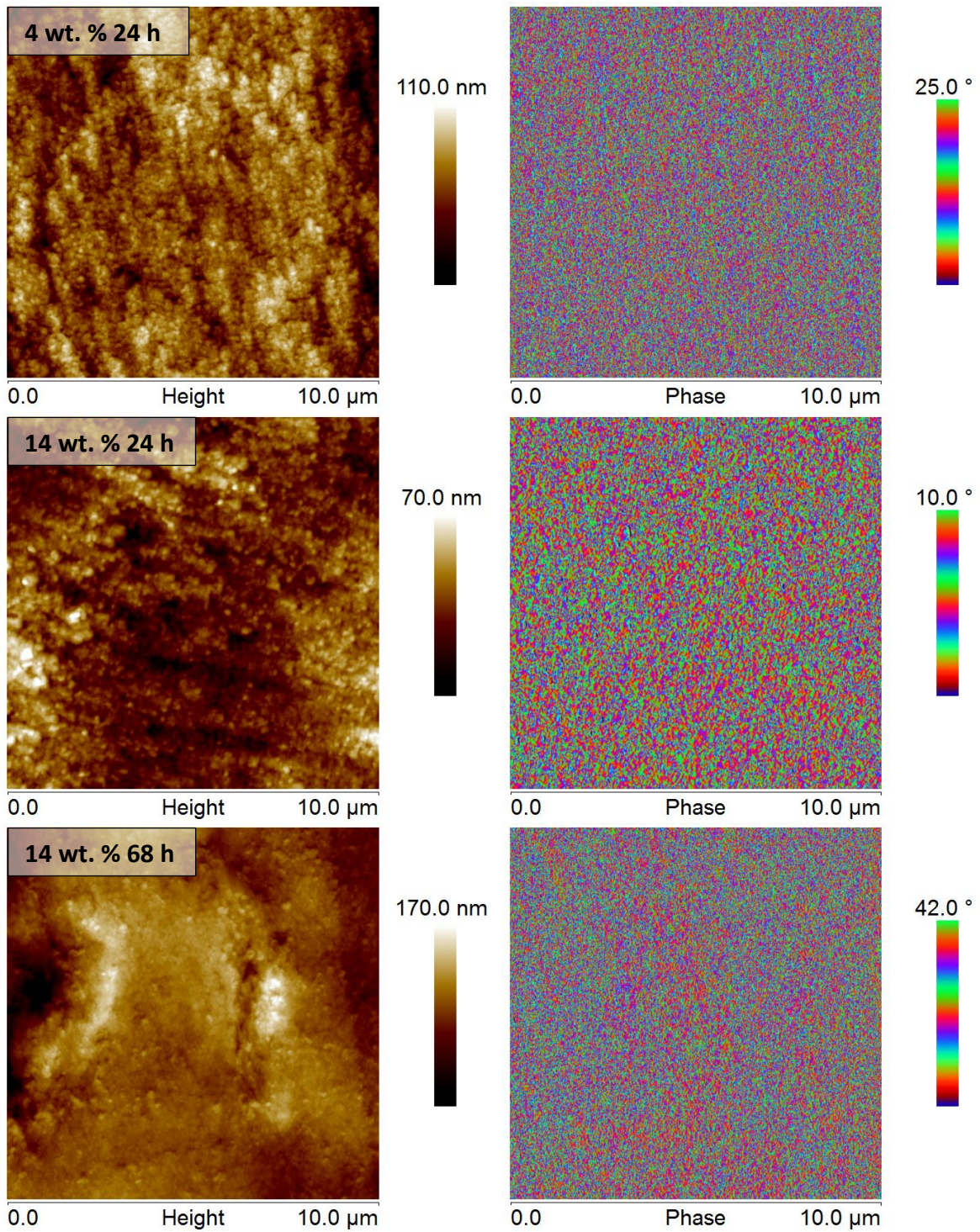
Fig. 56: 10 µm AFM height images (left) and phase images (right) of FSEC 4 wt. % 24 h (top), FSEC 14 wt. % 24 h (middle) and FSEC 14 wt. % 68 h (bottom).

6.6.3 Wet ultramicrotome cuts in the liquid cell

Two samples were embedded in epoxy, precut, immersed in a buffer solution (NaC) and then cut with the ultramicrotome under liquid conditions. The samples were then examined with the AFM in the liquid cell, which was also filled with buffer solution.

10 µm images are displayed in Fig. 57. The FSEC 4 wt. % shows a curved surface (with a radius of approximately 110 µm) which is due to further swelling after ultramicrotomy while the other sample is generally flatter but with a higher roughness. An analysis of the roughness of these pictures is in Table 4. Before analyzing a plane fit of the second order was executed on the FSEC 4 wt. % in order to reduce the influence of the curved surface on the results. The higher concentrated cellulose substrate has a higher general Z-range and also shows a higher roughness than the low concentrated one. The phase image (Fig. 57) of the FSEC 14 wt. % shows regions of the same color (black arrows) indicating different material composition in these regions and an inhomogeneous sample. The phase image of the FSEC 4 wt. % is more regular in comparison, except for some spots which are of topological cause.

Table 4: Roughness analysis of two FSEC samples (as displayed in Fig. 57).

Sample type	Z-range	R_q
FSEC 4 wt. % 68 h	263 nm	17 nm
FSEC 14 wt. % 68 h	356 nm	38 nm

Smaller regions were also scanned, 1 µm images are shown in Fig. 58 (same samples as above). The height images of both samples show a preferential direction which was probably caused by the ultramicrotomy cutting. The results of a roughness analysis are displayed in Table 5. Again the FSEC 14 wt. % is rougher than the lower concentrated sample. Nevertheless the difference is significantly less than in the big scan, which can be explained by the selected imaging region and the fact that images of 1 µm are less representative. The phase images reflect the same behavior as the phase images of the 10 µm scans. The FSEC 14 wt. % shows regions of same colors, while the FSEC 4 wt. % is more uniform. This indicates that the low concentrated specimen are more homogeneous in their composition.

Table 5: Roughness analysis of two FSEC samples (as displayed in Fig. 58).

Sample type	Z-range	R_q
FSEC 4 wt. % 68 h	83.4 nm	10.1 nm
FSEC 14 wt. % 68 h	77.7 nm	11.6 nm
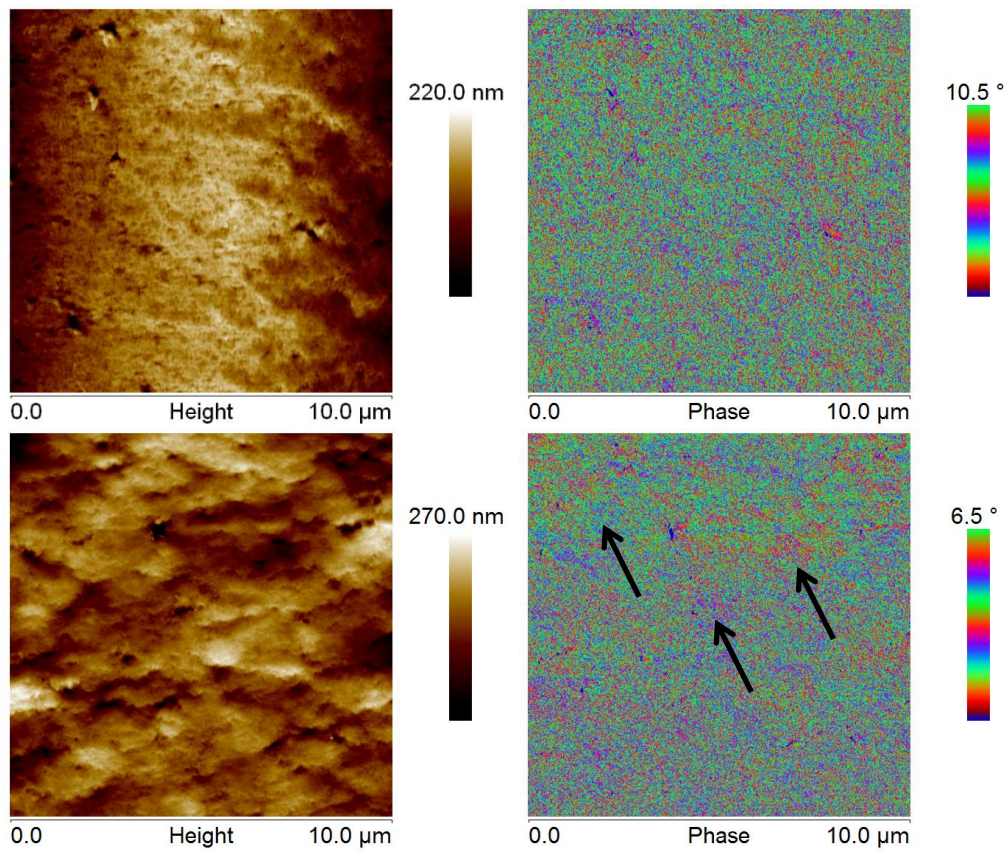
Fig. 57: 10 µm AFM height images (left) and phase images (right) of FSEC 4 wt. % 68 h (top) and FSEC 14 wt. % 68 h (bottom). Black arrows indicate inhomogeneities.
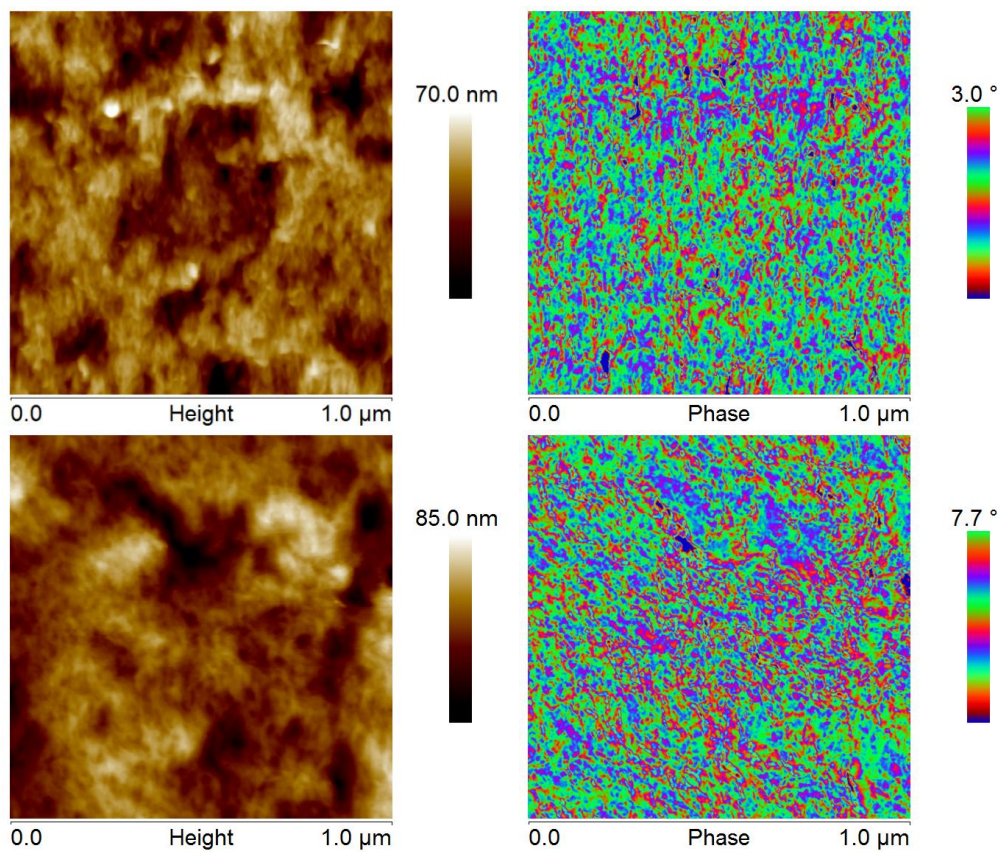
Fig. 58: 1 µm AFM height images (left) and phase images (right) of FSEC 4 wt. % 68 h (top) and FSEC 14 wt. % 68 h (bottom).

6.7 Alternative sample: spin cast cellulose

The cellulose samples which are usually used for the in situ visualization of enzymatic degradation take long to prepare, as they undergo many steps until they are usable for measurements. Nevertheless they have the big advantage of tunability, allowing production of samples with specific properties. For preliminary testing a fast and easy to use substrate is desirable. This has been uncovered with the spin cast cellulose. It is a fast and relatively simple to produce alternative. The process of production is described in chapter 5.2. Spin cast cellulose samples are characterized in this chapter.

6.7.1 X-ray diffraction

The X-ray diffraction of spin cast cellulose is part of an ongoing master thesis by Stephanie Rošker.

6.7.2 Raman spectroscopy

Raman spectra were taken for the spin cast samples (Fig. 59). In lower frequencies the intensity rises strongly (as in Avicel, see chapter 6.3.2) due to fluorescence effects. Therefore only the area 1 and area 2 (see Fig. 43) could be used for further evaluation. Even though the spectra look similar to the ones taken from FSEC samples the intensities are distributed differently due the different composition.
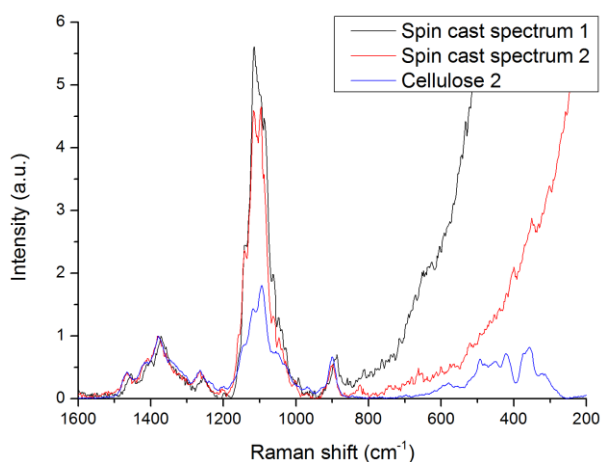
Fig. 59: Raman spectra of spin cast cellulose and cellulose 2 (FSEC 4 wt. %).

The two regions mentioned above were then used for further evaluation. They were integrated and set into relation. The result can be seen in Fig. 60 were it is compared with the results of the FSEC samples. It can be concluded that the spin cast sample is similar to the low concentration FSEC, being of the polymorph cellulose 2.
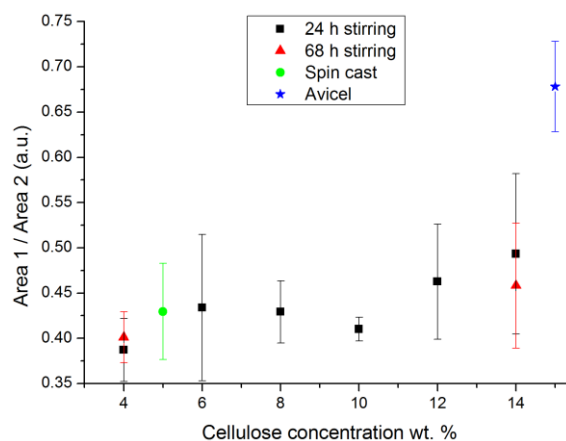
Fig. 60: Ratios of the areas from the Raman spectra for spin cast cellulose compared with standard samples and Avicel.

6.7.3 Transmission electron microscopy

TEM investigations of spin cast cellulose are part of an ongoing master thesis by Stephanie Rošker.

6.7.4 AFM-Analysis of the topology in dry and liquid environments

Dry environment:

Images of the sample in normal environment have been taken (Fig. 61). A fine structure can be seen in these measurements. The hydrophilicity of the cellulose makes measurements difficult, decreasing the possible resolution. Roughness analysis yields a Z-range of 8.4 nm and an average roughness of 1.1 nm.
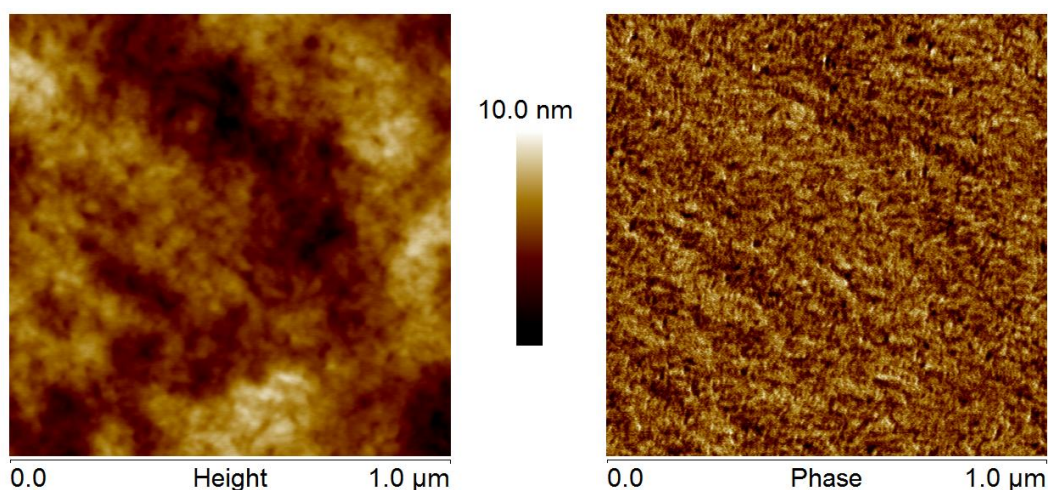
Fig. 61: 1 µm AFM height image (left) and phase image (right) of spin cast cellulose.

Liquid environment:

The dry samples were then immersed into the liquid cell which was filled with simple distilled water. Measuring in liquid raised the resolution immensely, making it possible to visualize the fascinating fibrillar structure of the spin cast samples (see AFM 3D-height image : Fig. 62) with a lateral feature of approximately **1.5 -2 nm** diameter (see green arrows in Fig. 63).
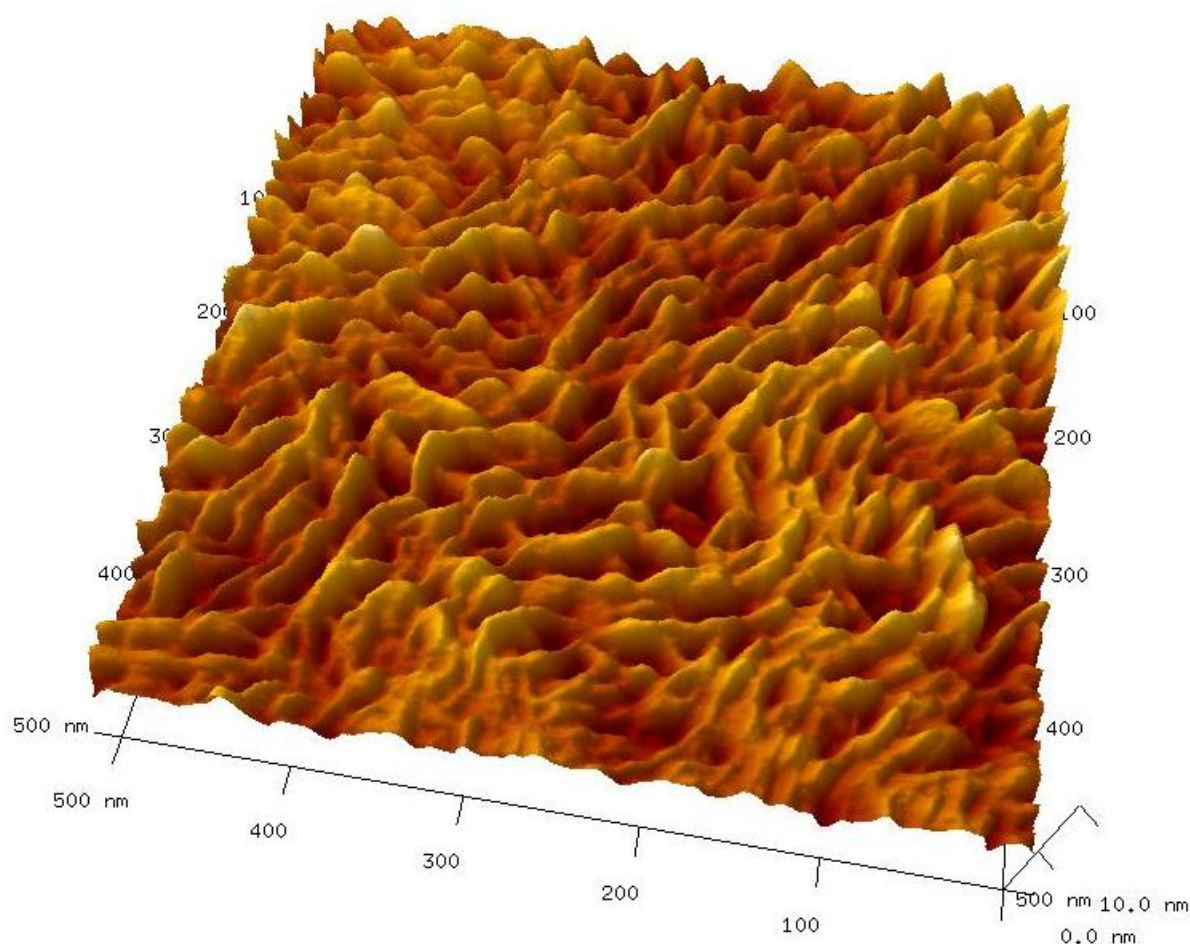
Fig. 62: 500 nm AFM 3D-height image of spin cast cellulose in liquid cell.

The fibrillar structure swelled while immersed in water. Fig. 63 shows the spin cast sample directly after immersing and approximately 45 minutes after. The blue arrows show a characteristic fiber which increased its size during incubation in water. In addition to single fibers also certain regions swelled more than others (red circles), indicating a vertical swelling. After about 30 minutes the swelling was observed to be widely saturated.

A roughness analysis is displayed in Table 6. It shows that the total Z-range (due to irregular horizontal swelling) rises. The average roughness changes only slightly.

Table 6: Roughness analysis of swollen spin cast cellulose (as displayed in Fig. 63)

Immersion time	Z-range	R_q
5 minutes	13.9 nm	1.5 nm
45 minutes	17.8 nm	1.6 nm
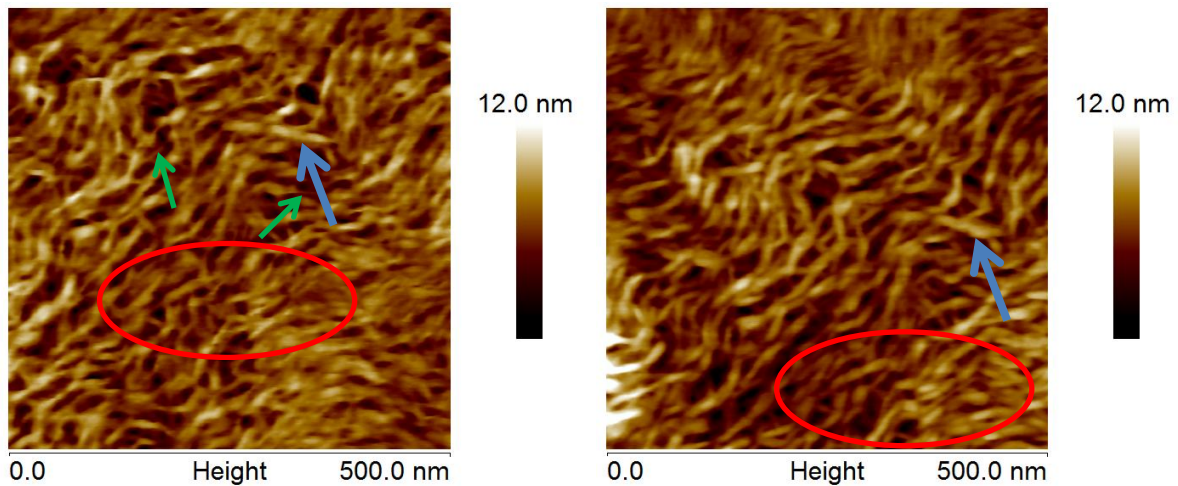
Fig. 63: 500 nm AFM height images of spin cast cellulose in liquid cell. Freshly immersed (left) and after 45 minutes in liquid (right). Blue arrows show swelling of fibres. Red circles show swelling of regions. Green arrows indicate features with diameter smaller than 2 nm.

Phase imaging (Fig. 64) reveals furthermore that the quality is improved and stable once the fibers are widely saturated (noise and resolution). This makes the spin cast cellulose a very promising potential substrate for real-time in situ measurements of enzymatic cellulose degradation.
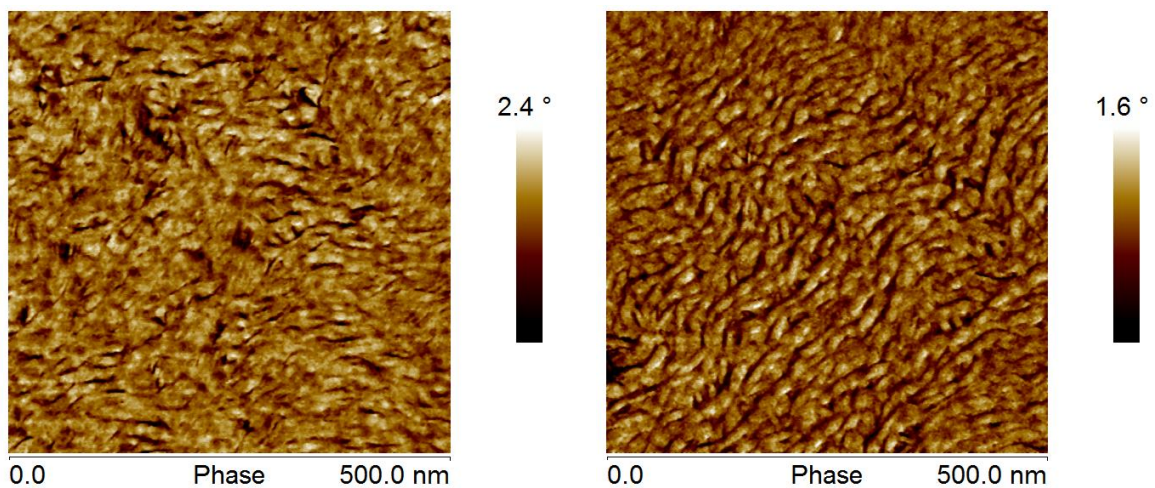
Fig. 64: 500 nm AFM phase images of spin cast cellulose in liquid cell. Freshly immersed (left) and after 45 minutes in liquid (right).

Also, amplitude imaging (Fig. 65) looks very helpful with these samples and allows for lateral resolution below 2 nm in liquid conditions. This resolution should make it possible to image single cellulase on the substrate.
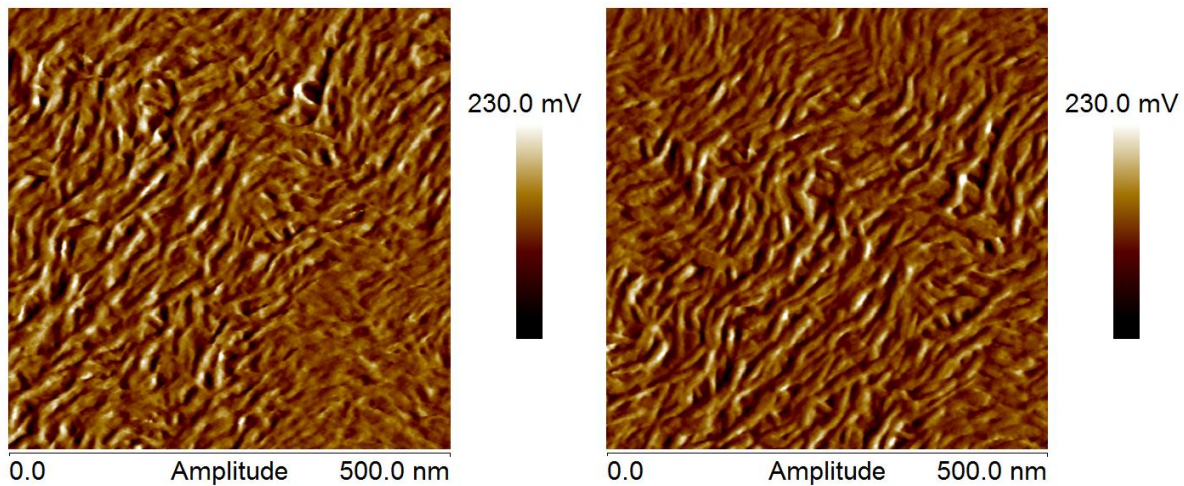
Fig. 65: 500 nm AFM amplitude images of spin cast cellulose in liquid cell. Freshly immersed (left) and after 45 minutes in liquid (right).

6.7.5   AFM-Analysis of thickness

The spin cast cellulose samples consist of multiple layers spin casted onto a sample carrier. The sample examined in this chapter is comprised of four layers. All layers were scratched through to the sample carrier in order to further characterize the samples regarding total thickness and layer thickness. In the first step AFM-images were recorded in a dry environment and evaluated. The next step was to immerse the sample in water, allow it to swell, and find the same place again for measuring. Two AFM 3D-images can be seen in Fig. 66, displaying the step from the substrate to the spin cast cellulose. The image of the dry sample (Fig. 66 left) was taken in a dry environment and the sample is not swollen. In liquid the sample is clearly swollen (Fig. 66 right). In both images steps are visible, in accordance to the manufacturing process.
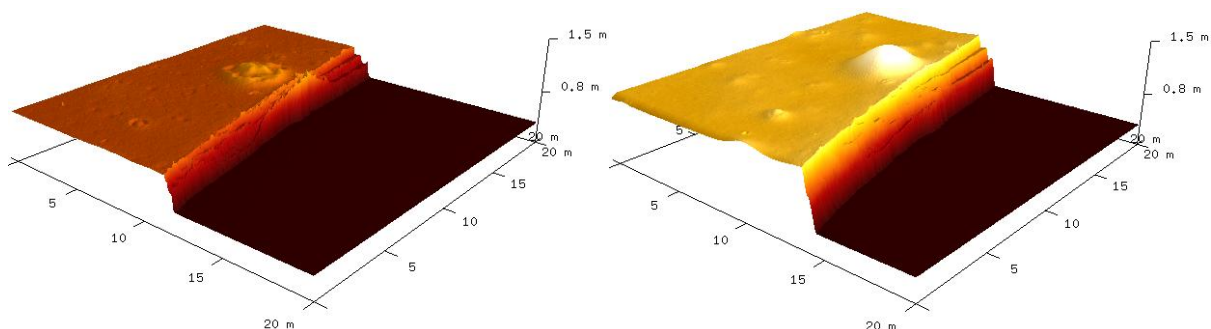
Fig. 66: 20 µm AFM 3D-height image of spin cast cellulose dry environment (left) and immersed in liquid (right).

The evaluation of the height is displayed in Table 7. The thickness increases by approximately 60 % of the original thickness. Interestingly the layers do not swell regularly in liquid. The top layer (approx. 125 nm) was a lot thinner than the two bottom layers (approx. 195 nm). This is probably caused by the chemichal structural changes during the multistep production of the spin cast cellulose.

Table 7: Height analysis of spin cast cellulose (as displayed in Fig. 66).

Measurement type	Total thickness	Layer thickness
Dry environment	431 ± 15 nm	115 ± 9 nm
Liquid cell	685 ± 25 nm	173 ± 29 nm

Fig. 67 shows the phase images of the steps. The phase difference between the sample carrier material and the cellulose is stronger and more recognizable in the wet environment. This suggests that chemical differences are easier to show in liquid than with a soft tip in dry environment. In turn this suggests, that cellulase should be distinguishable from the cellulose substrate when imaging in the liquid cell.
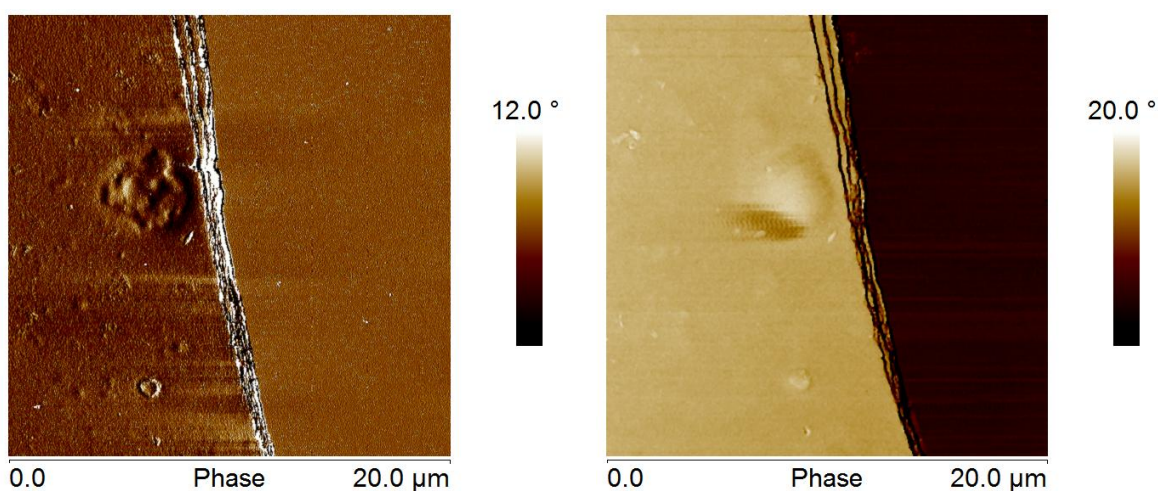
Fig. 67: 20 μm AFM phase image of spin cast cellulose dry environment (left) and immersed in liquid (right).

6.8 Summary

6.8.1 FSEC

The results will be compared by mixing ratios.

4 wt. % - 8 wt. %:
The Avicel is nearly completely dissolved during the stirring. After the solvent exchange the samples are very homogeneous and of the polymorph cellulose 2 with a high content of amorphous volumes. The ultramicrotomy cuts show very homogeneous and fine structure. The analysis performed with the TEM showed very few particles.

10 wt. % - 14 wt. %:
It was confirmed that the maximum solubility of Avicel in the ionic liquid BMIMCl is at approximately 8 wt. %. At higher concentrations Avicel is not fully dissolved in the ionic liquid. The stirring duration massively influences the homogeneity of the sample. Short stirred samples show large

agglomerations of undissolved crystals, while in long stirred ones the crystals are finely dispersed in a cellulose 2 matrix. This is also essential for imaging in the AFM as on the one hand the crystal agglomerations in the short stirred samples are difficult to cut, resulting in surfaces not suitable for the AFM. On the other hand long stirred samples show both crystal polymorphs cellulose 1 and cellulose 2 which makes them ideal for investigations of enzymatic degradation due to the increased crystalline content. The amount of cellulose 1 (crystalline areas) is controllable by the mixing ratio of Avicel to cellulose. The more Avicel is used the more cellulose 1 remains undissolved in the sample. This can be seen in the Raman curves which show the relative cellulose 1 to cellulose 2 ratios, and also in the TEM analysis which indicates a strong rise in particles for higher concentrations.

Furthermore, Raman-mapping showed that the crystals really are of the type cellulose 1 and are embedded in a cellulose 2 matrix. This indicates that the crystals are undissolved Avicel.

6.8.2 Spin cast cellulose

The Raman results for the test substrate spin cast cellulose suggest that they are of a very amorphous cellulose 2. It is a very finely structured surface with fibers varying diameter (1.5 – 15 nm). A big advantage of this sample is that also absolute measurements are possible. The thickness of the sample as well as the step size was analyzed during measurements. However, the drawback of such substrates is the limited layer thickness which limits the experimental possibilities such as long time observations and evolution of degradation in great depths. Nevertheless, it is highly suited to pretest the effect of new enzymes on cellulose before a time consuming but sophisticated FSEC substrate is used.

7   Enzymatic hydrolysis of cellulose

The in-situ visualisation of enzymatic hydrolysis is an important step forward in understanding what happens when enzymes are deployed on the cellulose surface. These measurements base on the research done by Judith Dohr [42] and Thomas Ganner [24]. In Judith Dohrs master thesis she describes the changes in morphology after enzymatic degradation, drying the sample between each measurement. Thomas Ganner then introduced a liquid cell, allowing in-situ measurements in liquids. The liquid cell enables to follow exactly the degradation processes and a theory explaining occurring synergism effects was found [24].

All enzyme solutions and buffer solutions were prepared by DI Manuel Eibinger and DI Dr. Patricia Bubner from the Institute of Biotechnology and Bioprocess-Technology. AFM-imaging was done with a Dimension 3100 (Digital Instruments, VEECO) with a Hybrid X-Y-Z closed loop scan head and a Nanoscope IVa controller. The liquid cell used is an in-house construction and all measurements were conducted at room temperature (22° C). A more detailed description is given in chapter 3.6.

The procedure of measurement was essentially always the same. The ultramicrotomy cut sample would be removed from its sample vial (where it was immersed in buffer solution) and put into the liquid cell where it was fastened with screws (fixation can be seen in chapter 3.6.4.4). An appropriate amount of buffer solution would be immediately added to prevent the cellulose surface from drying (high risk of mechanical stress and strain). The next step would be to align the AFM for measurement and search for a suitable place for further examination. Then a defined enzyme concentration was added with a micropipette and continuous AFM-imaging would capture the cellulose degradation.

Various measurements were conducted and will be described in this chapter. It will start with observations upon single enzymes (CBH1, CBH2). Then enzyme combinations will be studies (CBD and CBH1, supernatant). And the chapter will finish with the research conducted on cellulosomes. Spin cast cellulose was used first as test vehicle with cellulosomes before measurements on standardized cellulose samples started.

7.1   CBH1 on FSEC 4 wt. % and on FSEC 14 wt. %

CBH1 is an exo-glucanase which degrades cellulose chains by starting from its reducing end (see chapter 2.3.1.1). For this the reducing end has to be accessible for CBH1 to become active. If the enzyme finds a reducing end on a chain it binds to it with a binding domain. Then it can move along the chain powered by the energy output from hydrolysis. Amorphous cellulose is not reduced by CBH1 as a consequence of the necessity for a reducing end.

The enzymatic reaction of CBH1 was observed on FSEC 4 wt. % and FSEC 14 wt. %. This was done for two reasons: to watch the enzymatic activity and to confirm that the low concentration cellulose substrates are highly amorphous. The AFM-images of these measurements are displayed in Fig. 68. The FSEC 4 wt. % shows practically no change in topology while holes start to form on the FSEC 14 wt. % sample. These findings confirm that the low concentration cellulose substrates are mainly of amorphous cellulose 2. A

section of each image was taken and compared in Fig. 69. The exact sections could not be compared as the samples underwent a lot of drift during the imaging. Nevertheless it can be seen, that the FSEC 14 wt. % undergoes enzymatic degradation while the FSEC 4 wt. % stays mostly unchanged.
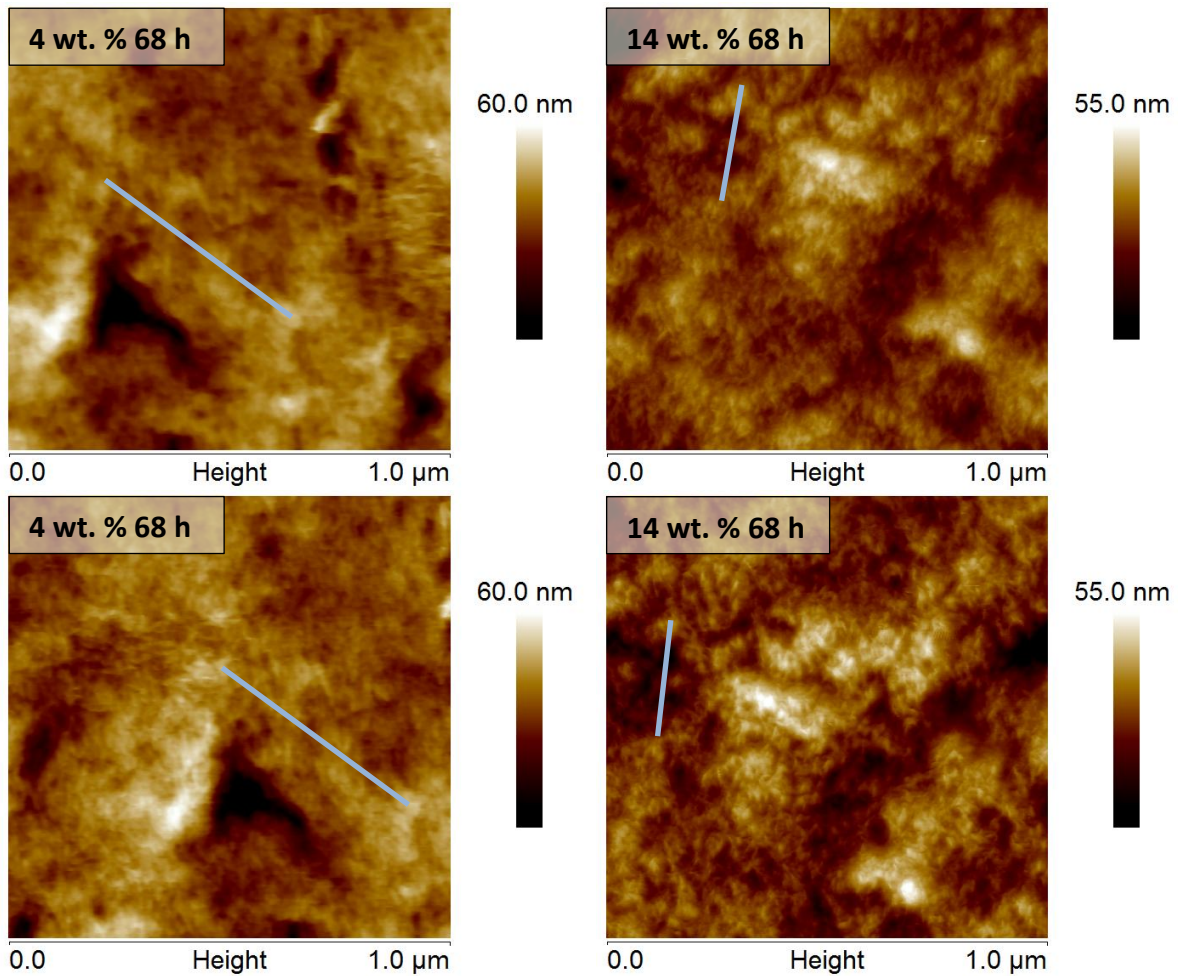
Fig. 68: 1 µm AFM height images of FSEC 4 wt. % (left) and FSEC 14 wt. % (right) before enzymes were added (top) and 2 hours after enzymes were added (bottom). Blue lines indicate section for further analysis.
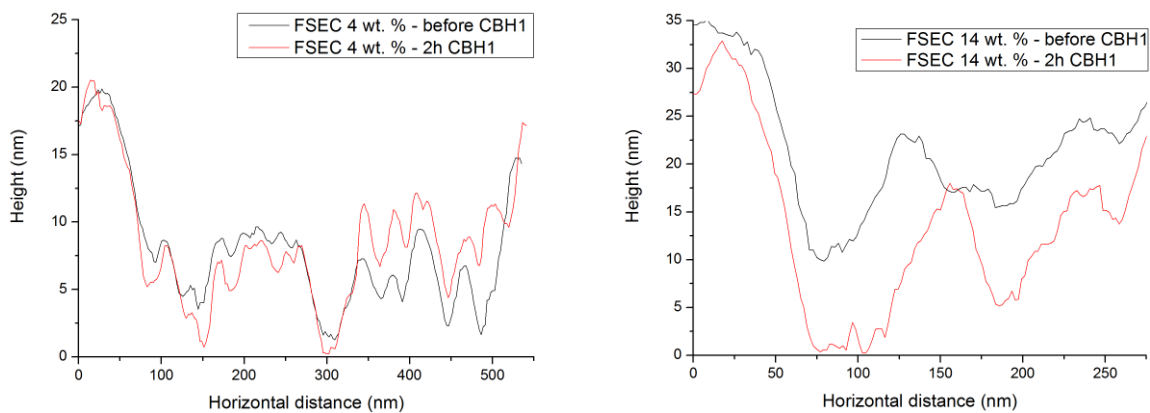
Fig. 69: Sections of the AFM height images along the blue lines indicated in Fig. 68. Before CBH1 and 2 hours after CBH1.

A roughness analysis was carried out (Table 8). On the one hand for the low concentration sample the roughness does not significantly change. The change in Z-range during two hours CBH1 exposure can be explained by sample drift. On the other hand for the high concentration sample the Z-range increases strongly (+74 %) while the average roughness does not undergo too much change.

Table 8: Roughness analysis of FSEC 4 wt. % and FSEC 14 wt. % before and after 2 hours of CBH1.

	FSEC 4 wt. %		FSEC 14 wt. %	
	Z-range	R_q	Z-range	R_q
Before CBH1	83.1 nm	7.8 nm	54.5 nm	6.3 nm
2h of CBH1	75.7 nm	7.3 nm	73.9 nm	7.4 nm

To conclude, CBH1 only degrades crystalline areas which is in agreement with literature and previous work done at the FELMI with the same cellulose / cellulose system. The low concentration cellulose samples (FSEC 4 wt. %) are amorphous / cellulose 2 and therefore not degraded by CBH1. Nonetheless the high concentration samples are a mixture of amorphous / cellulose 2 / cellulose 1 and therefore degradation by CBH1 can be observed.

7.2 CBH2 on FSEC 4 wt. % and on FSEC 14 wt. %

CBH2 is known as an exo-glucanase, while T. Ganner [24] also found endo-glucanase behaviour. He further suggests that CBH2 mainly degrades amorphous cellulose [1].

The systematic methodology of these measurements is a bit more elaborate then of the previous measurements. In order to become as thorough results as possible the following procedure was followed for a FSEC 4 wt. % and a FSEC 14 wt. % sample:

| Sample Preparation (UM etc.) | → | Liquid cell AFM | → | 24h CBH2 incubation | → | Liquid cell AFM | → | Rinse and dry sample | → | Dry environment AFM |

All steps in this chapter were performed at room temperature (22° C). The rinsing was performed with buffer solution and the sample was pre-dried for a few seconds with a CO_2-Spray before air drying for 24 hours (FSEC 4 wt. %) and 48 hours (FSEC 14 wt. %).

The measurements on the FSEC 4 wt. % are displayed in Fig. 70. The topology changes massively after the 24 hours of CBH2 incubation. Before enzymatic degradation the surface is rough but relatively flat with some holes and cuts, probably due to the UM-cutting. The aim was to find the same place again after 24 h CBH2 incubation to also be able to look at localized changes. This turned out to be impossible because after 24 h of CBH2 degradation the surface showed an entirely different topography. The surface was now nodular with higher height differences. Furthermore, imaging in liquid after 24 h incubation was difficult as the cellulose sample was a lot softer and fringier than before. After rinsing and drying (Fig. 70 bottom) the sample still displays the same nodular properties (in dry environment) as in the liquid AFM-image, but with better resolution. Imaging became easier as the cellulose dried and hardened so better quality images could be

achieved. A roughness analysis of the sample is displayed in Table 9 (author's note: the images used for evaluating the roughness were 10 µm AFM height images and are not displayed in this work). As can already be seen in the images the Z-range as well as the roughness increase massively due to the degradation. There is very little difference between the liquid cell measurement and the dry measurement (after degradation). The sample was found to be generally still quite homogeneous.
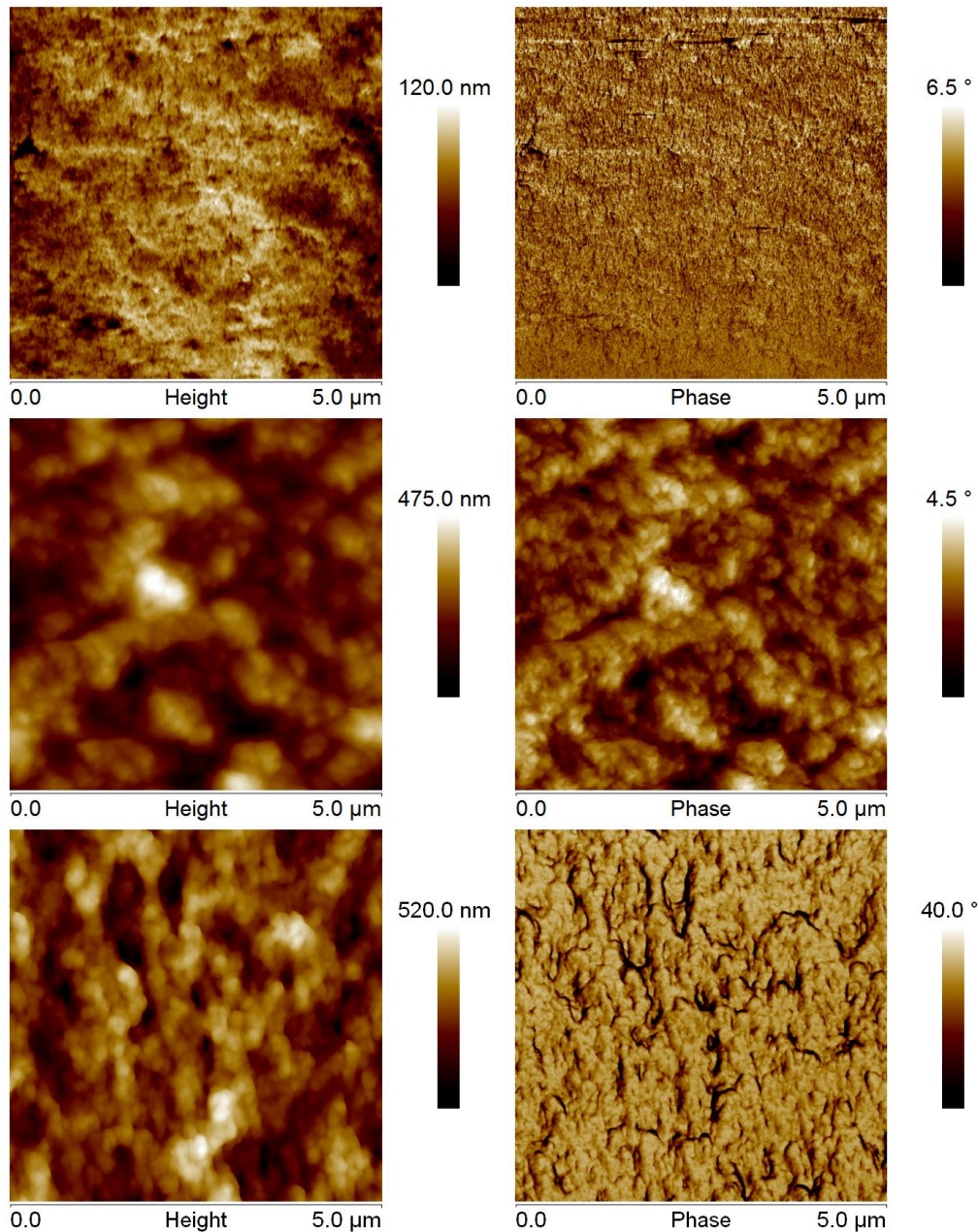
Fig. 70: 5 µm AFM height images (left) and phase images (right) of FSEC 4 wt. % 68h. In liquid before CBH2 (top), in liquid after 24 h CBH2 (middle), dry after 24 h CBH2 and rinsing (bottom).

The images recorded on FSEC 14 wt. % are shown in Fig. 71. Before enzymatic degradation (top images) the surface is relatively flat, but with some very deep holes (because of UM-cutting). After 24 h of CBH2 incubation the samples topology (Fig. 71 middle) has entirely changed. Moreover, the texture has changed massively. The sample has become very soft with fringes hanging from the surface. These changes make imaging nearly impossible, only allowing very poor image quality. After

rinsing and drying for 48 hours dry environment AFM-images were captured (Fig. 71 bottom). They show a lumpy surface, with no clear structures. The surface was noticeably soft and imaging was very difficult and tricky to perform due to the samples texture. The samples roughness was also evaluated and is shown in Table 9 (author's note: the roughness analysis was performed on selected areas of 10 μm AFM height images which are not displayed in this work). The variation in Z-range can be explained by the fact that in each step different positions on the sample were measured. The average roughness increases after the degradation by CBH2.
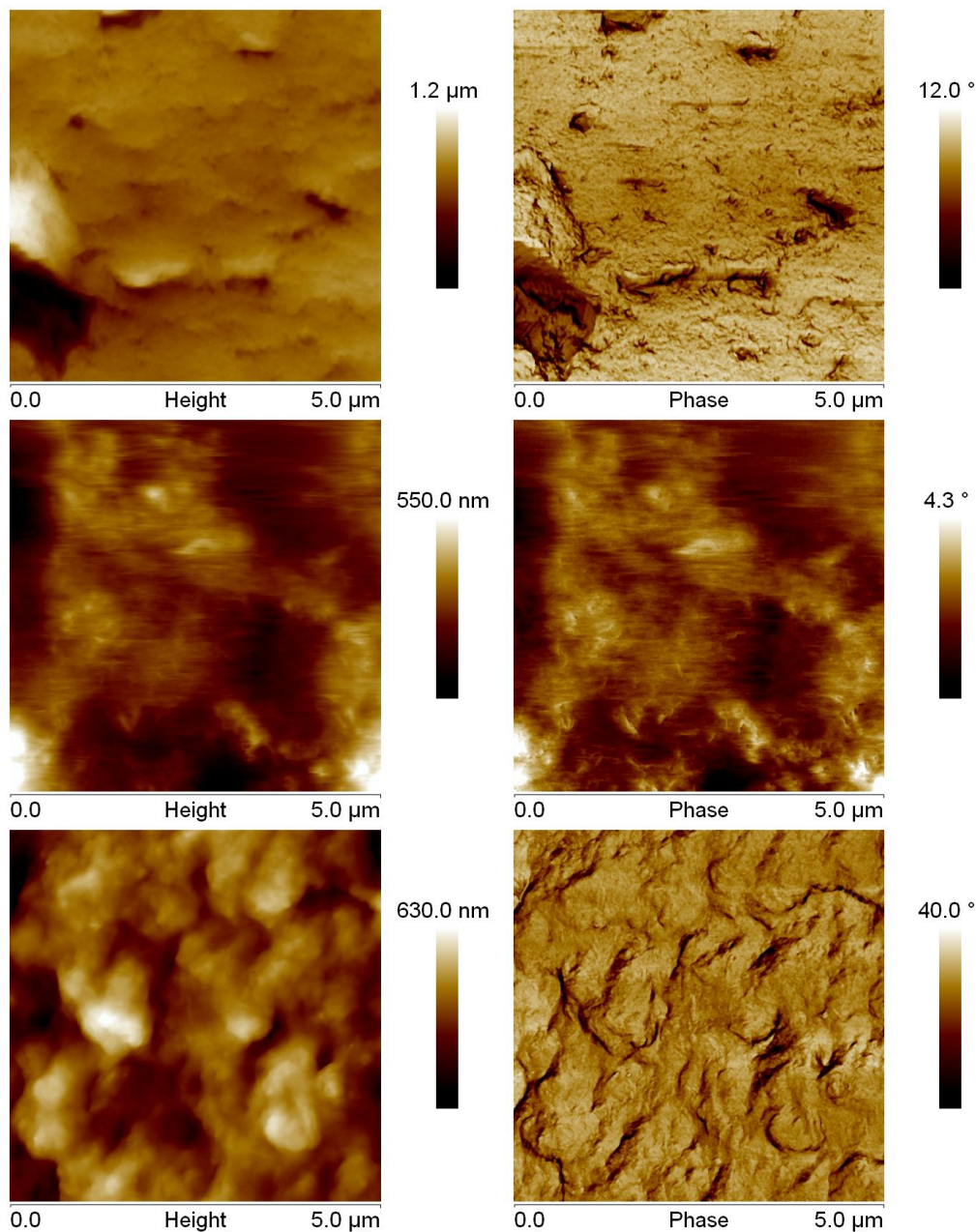
Fig. 71: 5 μm AFM height images (left) and phase images (right) of FSEC 14 wt. % 68h. In liquid before CBH2 (top), in liquid after 24h CBH2 (middle), dry after 24h CBH2 and rinsing (bottom).

Table 9: Roughness analysis of FSEC 4 wt. % and FSEC 14 wt. % before and after 24h of CBH2; liquid cell and dry environment measurements.

	FSEC 4 wt. %		FSEC 14 wt. %	
	Z-range	R_q	Z-range	R_q
Before CBH2 (LC)	259 nm	17 nm	783 nm	90 nm
After 24 h CBH2 (LC)	540 nm	72 nm	1018 nm	145 nm
Dry, after 24h CBH2 (dry)	575 nm	77 nm	728 nm	106 nm

In summary, CBH2 degrades both samples strongly. The 4 wt. % undergoes a complete topological change, with the sample still being relatively stable after the degradation process. The 14 wt. % sample changes both in topology and in texture. After 24h of CBH2 it is completely soft, spongy and fringed, making AFM-imaging very difficult. It should be mentioned, that with these substrates only relative degradation is measurable as no fixed indicator is given. Stephanie Rošker from the FELMI is currently developing substrates which will allow absolute degradation measurements. These findings confirm T. Ganners' [1] suggestion, that CBH2 mainly degrades amorphous cellulose. The fringes which were found in the FSEC 14 wt. % degradation are probably undissolved crystalline cellulose 1.

7.3   CBD and CBH1 on FSEC 14 wt. %

Cellulose-binding domains and a catalytic core domain are the two functional domains of CBH1 [21]. It is supposed to be responsible for making the cellulose accessible to the enzyme and does not react with the substrate by itself. It was found that the effective enzyme-concentration on insoluble cellulose substrates is increased in the presence of CBD [25].

Measurements were conducted in order to find the influence of CBD on the enzymatic degradation of CBH1. For this a FSEC 14 wt. % was observed in the liquid cell. After taking a stable image the CBD was added. The sample was then monitored for two hours. Then the CBH1 was added and the degradation was watched for another 3.5 hours. During all this time the sample was drifting considerably, therefore it was necessary to adjust the offset permanently. Selected AFM images are shown in Fig. 72. An according analysis of the sample roughness is shown in Fig. 73.

The AFM images show practically no difference after 2 hours of CBD exposure (compare Fig. 72 top and middle). The topology and texture are the same as before adding CBD. During the two hours of the roughness undergoes some changes (Fig. 73 between the two blue arrows). The reason of this roughness-change could be found in swelling by the CBD, but might as well be influenced by the drift of the sample.

No immediate effects could be observed after CBH1 was added; it takes some time for the enzymes to diffuse to the cellulose surface and interact with the cellulose. The changes of surface roughness that can be seen in Fig. 73 between minute 130 and minute 190 are probably caused by adjustments of the AFM parameters which were done while measuring. After approximately 60 minutes of CBH1 a slight increase of surface roughness can be observed. The roughness starts to increase strongly

about 1.5 h after the CBH1 was added indicating strong enzymatic degradation. The topology is strongly changed with big fractions being degraded (Fig. 72 bottom). Also the texture becomes softer and fringed, making it more difficult to get stable and reliable AFM images. This is recognizable (indicated by green arrows in Fig. 72 bottom)
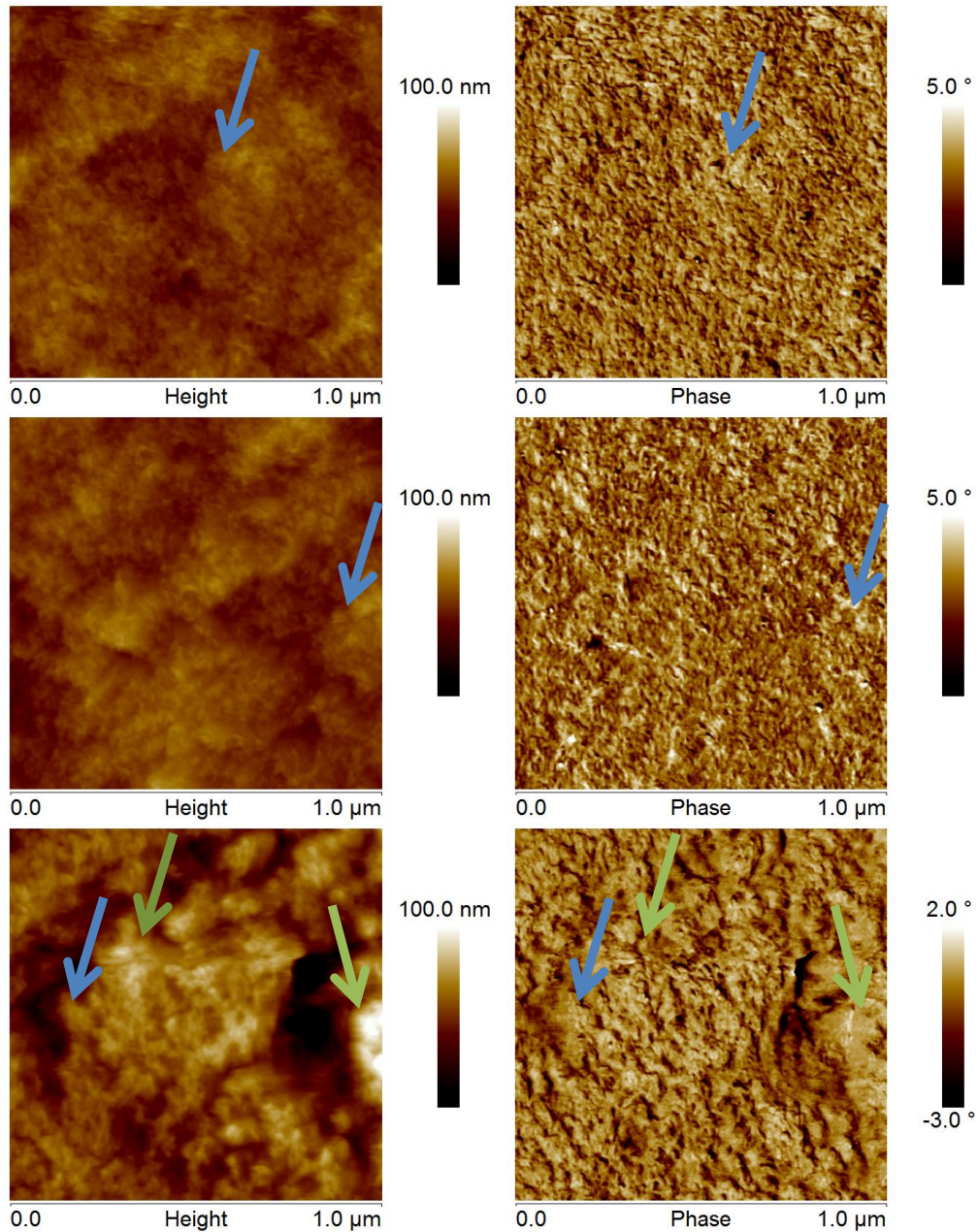
Fig. 72: 1 µm LC-AFM height images (left) and phase images (right) of FSEC 14 wt. % 68 h. Before CBD (top), after 2 h CBD and before CBH1 (middle), after 5.5 h CBD and 3.5 h CBH1 (bottom). Blue arrows point to the same spot. Green arrows indicate soft and fringed regions.
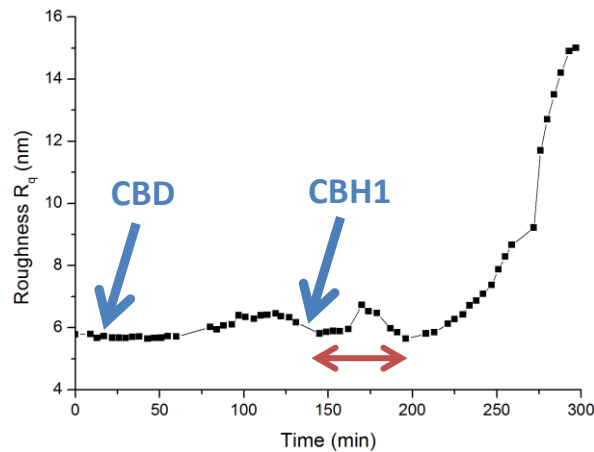
Fig. 73: Roughness of FSEC 14 wt. % during incubation by CBD and CBH1. Blue arrows indicate addition of CBD and CBH1. Red arrow indicates time between addition and activity of CBH1.

7.4 Supernatant of Trichoderma Reesei

Studies on the supernatant of Trichoderma Reesei on high concentrated cellulose samples have previously been performed by Thomas Ganner [24]. This chapter will describe the measurements performed with supernatant on FSEC 4 wt. % and spin cast cellulose and set the results in relation to those of T. Ganner.

Fermentation supernatant was SVG17 with a concentration of 36 µg per mg substrate and was provided by Manuel Eibinger from the Institute of Biotechnology and Bioprocess-Technology.

7.4.1 Supernatant on FSEC 4 wt. %

The supernatant has been deployed on a FSEC 4 wt. % and the time evolution was imaged in the LC-AFM (Fig. 74). The images displayed were taken at varying time intervals. In this run the time for the enzymes to reach the sample was quite long – first results were observable after 1.5h. In the next hour the height images became blurrier, indicating a binding of the enzymes on the cellulose surface. After that the enzymes started to degrade the cellulose rapidly. This can also be seen in the roughness analysis (Fig. 76) where the roughness is rather constant for nearly three hours and then starts to rise quickly. The height profile of a section during degradation is shown in Fig. 75. The relative distance between the lines is not entirely reliable as an absolute comparative value does not exist.

Two 3D height images are displayed in Fig. 77 for the purpose of showing how much the topology changes during enzymatic degradation. The left image shows the samples surface before supernatant was deployed, the right one was taken after five hours of degradation.
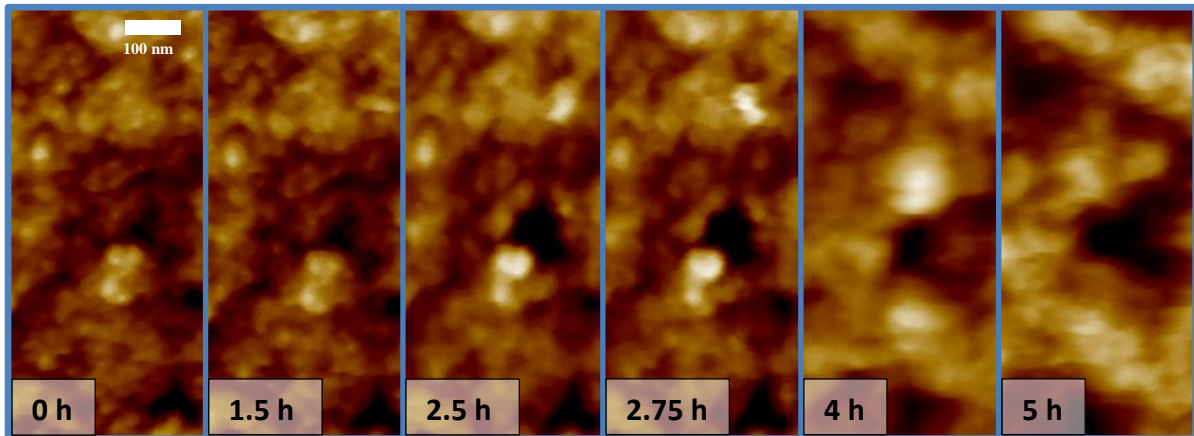
Fig. 74: AFM height images of cellulose at different times during supernatant degradation. Z-scale 0 h – 2.75 h: 22 nm, Z-scale 4 h – 5 h: 100 nm. Grey boxes indicate incubation time.
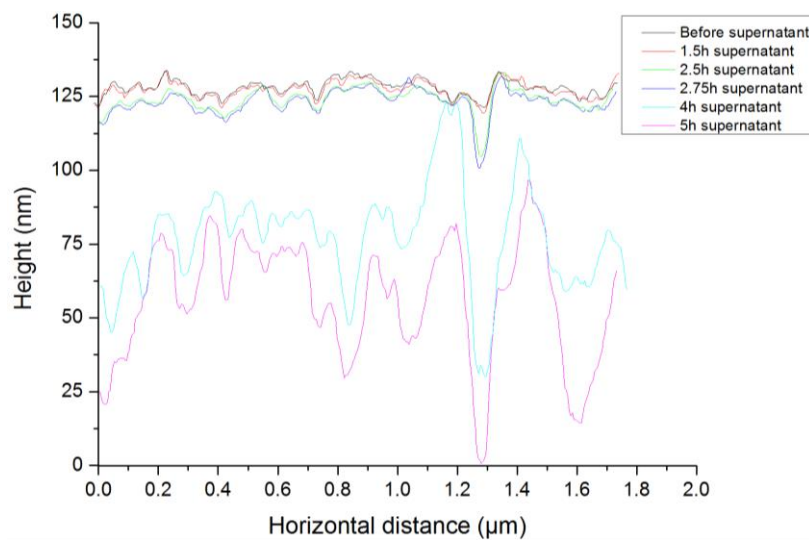
Fig. 75: Height profile of FSEC 4 wt. % during degradation by supernatant.
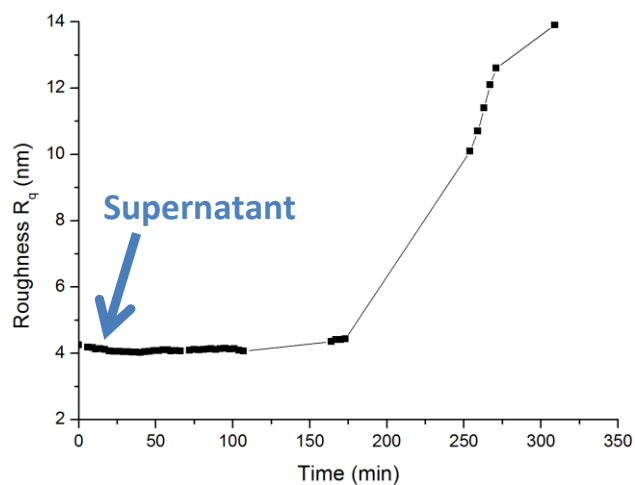
Fig. 76: Roughness of FSEC 4 wt. % during degradation by supernatant. Blue arrow indicates addition of supernatant.
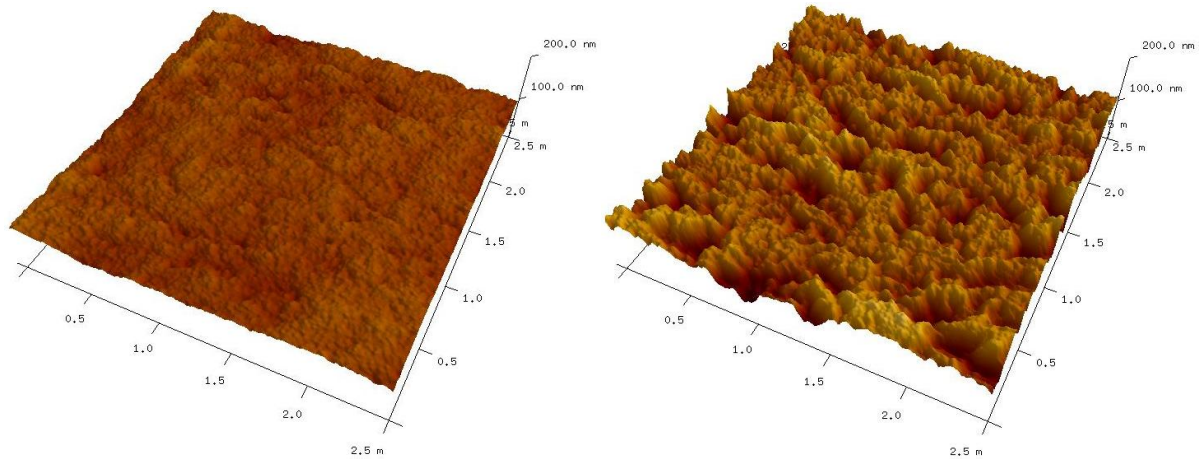
Fig. 77: 2.5µm AFM height images before degradation (left) and after 5 h of supernatant.

7.4.2 Supernatant on spin cast cellulose

In order to observe the supernatant degradation of spin cast cellulose a specimen was scratched with tweezers. Then the sample was immersed into the LC which was filled with buffer solution and given some time to swell. The scratching was done to also enable thickness measurements in addition to surface observations. Therefore the analysis in this chapter is split into two parts: degradation and swelling.

Supernatant of Trichoderma Reesei was added in a concentration of 2 µg / mm².

Degradation:

The time evolution was studied in the LC-AFM (height images: Fig. 78; phase images: Fig. 79). The blue arrow shows the same spot (drift was very strong). The degradation starts very fast, already after 30 minutes the samples surface has lost most of its fibrillar structure (compare Fig. 62) and has become slightly nodular. The topology changes more and more as the time passes. Degrading the samples surface and changing it completely. After 2.5 h the sample is barely recognizable. After nearly two hours also the texture starts to change and the sample becomes softer, this is especially visible in the phase images (Fig. 79 bottom right).
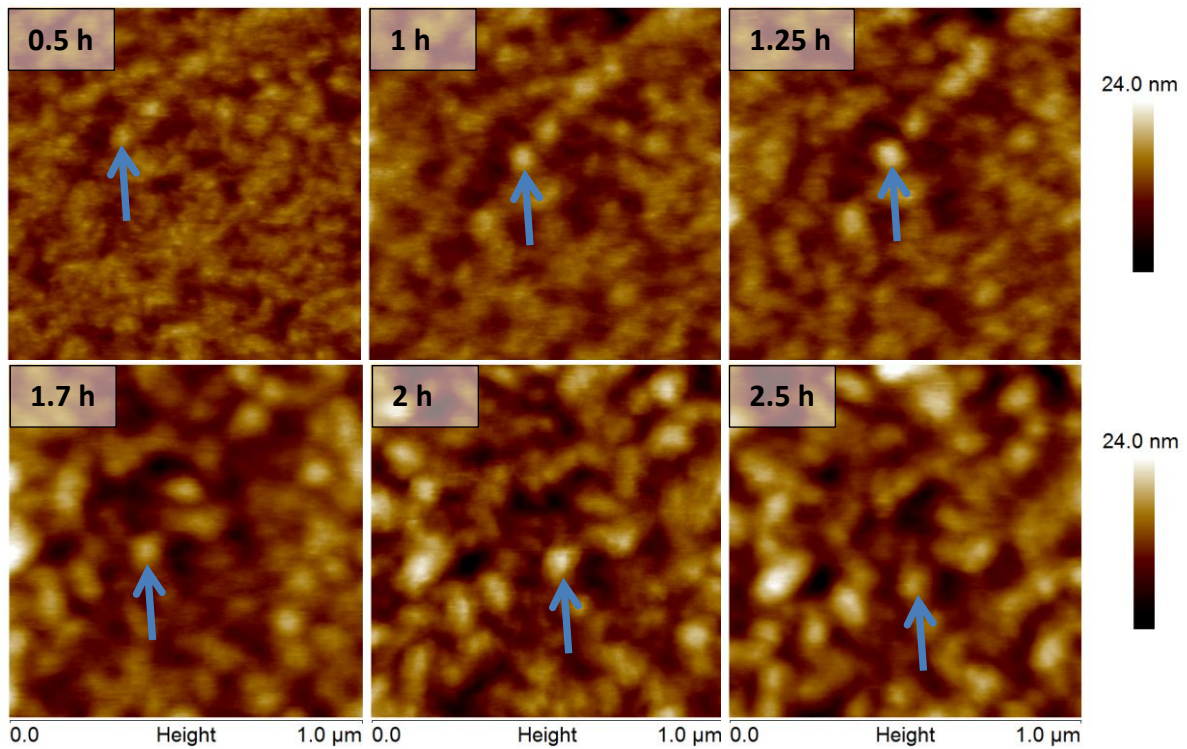
Fig. 78: 1 μm AFM height images of spin cast cellulose during degradation by supernatant. The grey boxes indicate incubation time, blue arrows show the same spot on the images.
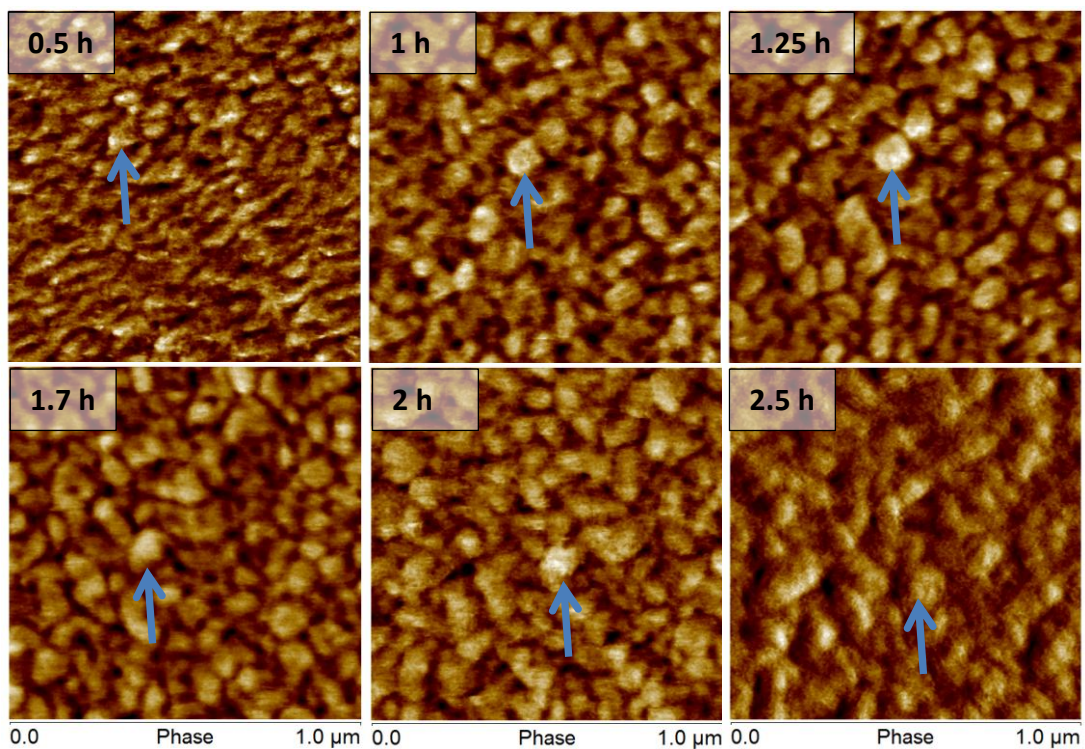
Fig. 79: 1 μm AFM phase images of spin cast cellulose during degradation by supernatant. The grey boxes indicate incubation time, blue arrows show the same spot on the images.

Swelling:

Two 3D-height images of a step in the spin cast cellulose are displayed in Fig. 80. The topology changes from a relatively flat surface with well-defined straight steps to a rough surface with holes and fringed steps. The edges become very fringed and difficult to measure. This leads to the conclusion, that edges are preferred by enzymes due to easier access. The degraded surface also shows some holes. Many of these holes coincide with elevated regions of the sample before the supernatant was applied. This suggests that the elevated regions are bubbles with a thin coating. When the supernatant is applied it removes the coating and exposes the holes.
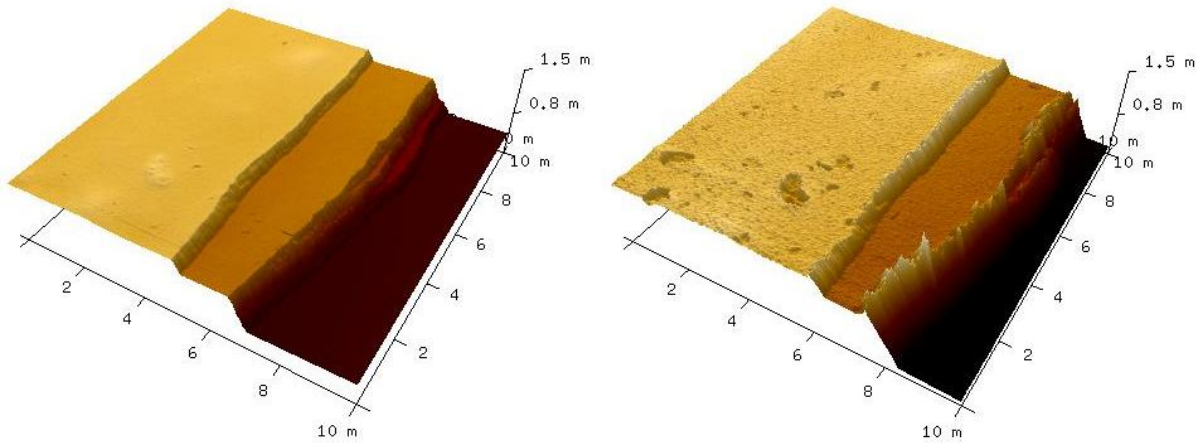
Fig. 80: 10 µm AFM 3D-height images of a scratched step in spin cast cellulose before (left) and after 2.5 h of supernatant (right).

Height profiles of the scratched edge before and after degradation are compared in Fig. 81, and values are displayed in Table 10. The total thickness rises even though the sample is degraded by the supernatant. This effect was expected and can be explained by cellulase diffusing into the cellulose and loosening the cellulose structures and thereby increasing its thickness.
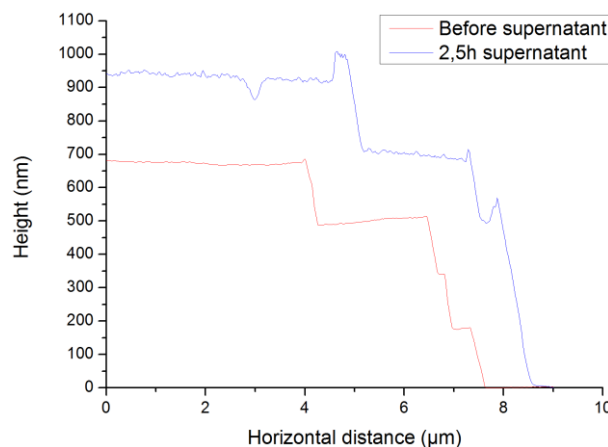
Fig. 81: Height profile of a step in spin cast cellulose before and after 2.5 h of degradation by supernatant.

Table 10: Height analysis of spin cast cellulose during supernatant degradation (as displayed in Fig. 80).

Measurement	Total thickness	Layer thickness
Before supernatant	685 ± 8 nm	174 ± 7 nm
After 2.5 h supernatant	937 ± 12 nm	223 ± 15 nm

7.5   Summary: Trichoderma Reesei

A short summary on the results of Trichoderma Reesei in context with its application on different substrates will be given.

CBH1:

This enzyme is known to prefer crystalline cellulose [1]. Applied on a highly amorphous sample (FSEC 4 wt. %) practically no degradation could be observed. When the same measurement was conducted with a sample with mixed cellulose phase (FSEC 14 wt. %) a comparably strong degradation was found. This proves the increasing crystalline content (cellulose 1 via undissolved Avicel) for higher concentrations and thereby the tunability of the FSEC substrates which was the main aim of the study!

CBH2:

CBH2 is supposed to mainly degrade amorphous cellulose. After 24 hours of incubation at room temperature both samples (FSEC 4 wt. % and FSEC 14 wt. %) had been degraded strongly and had drastically changed their topology. The surface of FSEC 4 wt. % was strongly degraded but still stable and measurements were easily possible as the texture had not changed noticeably. The FSEC 14 wt. % showed very different behavior. After 24 hours of CBH2 not only the topology had changed strongly, but also the texture had gotten very soft and fringed. So both samples have undergone strong topological changes, while only the FSEC 14 wt. % also changed its texture strongly. This supports CBH2's preference of amorphous cellulose.

CBD and CBH1:

The CBD itself did not change the substrate noticeably. But the added CBH1 degraded the surface rapidly. The addition of CBD seems to increase the degradation speed, as has been suggested by [25].

Supernatant:

Supernatant was applied on a FSEC 4 wt. % and on a spin cast cellulose. Both show rapid degradation by the supernatant (as expected) due to the synergistic effects between CBH1, CBH2 and EG. These experiments confirm further that the artificial FSEC substrates behave very similar compared to natural substrates which proves the suitability for in-situ experiments.

Interestingly the spin cast cellulose enabled the possibility of showing that the substrate swells due to the enzymes in the solution. This has been suspected before, but proof was difficult as only relative measurements were possible.

Substrates:

The FSEC samples make it possible to observe degradation of different cellulose polymorphs at the same time. This is especially interesting for synergistic effects where different enzymes work hand in hand and therefore increase degradation speed.

The spin cast cellulose samples are very practical as fast and easy to use test substrate as only very little preparation is necessary before they can be used in the LC-AFM.

7.6 Cellulosomes

Cellulosomes are cell bound multi-enzyme complexes which deconstruct cellulose and hemicellulose [26]. No in situ AFM measurements of cellulosomes are published even though extensive research is being conducted. In a first proof of concept performed it seemed to be possible to measure cellulose degradation. Further measurements lead to the discovery, that in situ imaging of cellulosomes is a lot more difficult than initially thought to be. Various error sources and troubleshooting approaches were considered and tried. Eventually, after extensive research and taking over 560 AFM images the main problems could be identified but not eliminated.

This chapter will briefly show results of the proof of concept and then deal with describing the systematic approach in identifying the error sources.

7.6.1 Proof of concept on spin cast cellulose

The feasibility study was performed on a spin cast cellulose sample. The buffer solution used was 50 mM Na-citrate, pH 5.0 buffer with 12 mM $CaCl_2$ and 5 mM cysteine-HCl. Three interesting effects were visualized. The first is just simple degradation of cellulose fibers. Secondly, agglomeration (possibly cellulosomes) was observed. Finally the combination of the two was also observed, with first agglomeration and then degradation (Fig. 82).The blue arrows indicate possible cellulosomes.
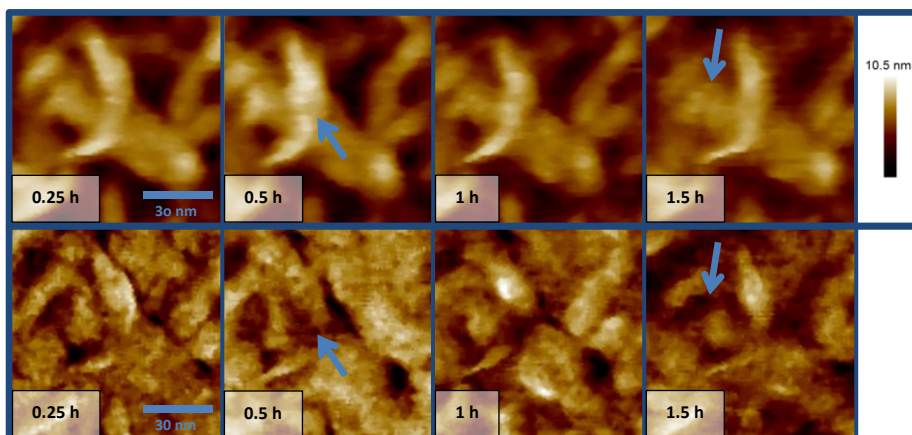
Fig. 82: AFM height (top) and phase (bottom) images of agglomeration and degradation during cellulosome incubation. Phase bar is not displayed because of strongly varying phase values.

Eventually after measuring for approximately two hours the topology and texture had changed drastically, as is shown in Fig. 83.
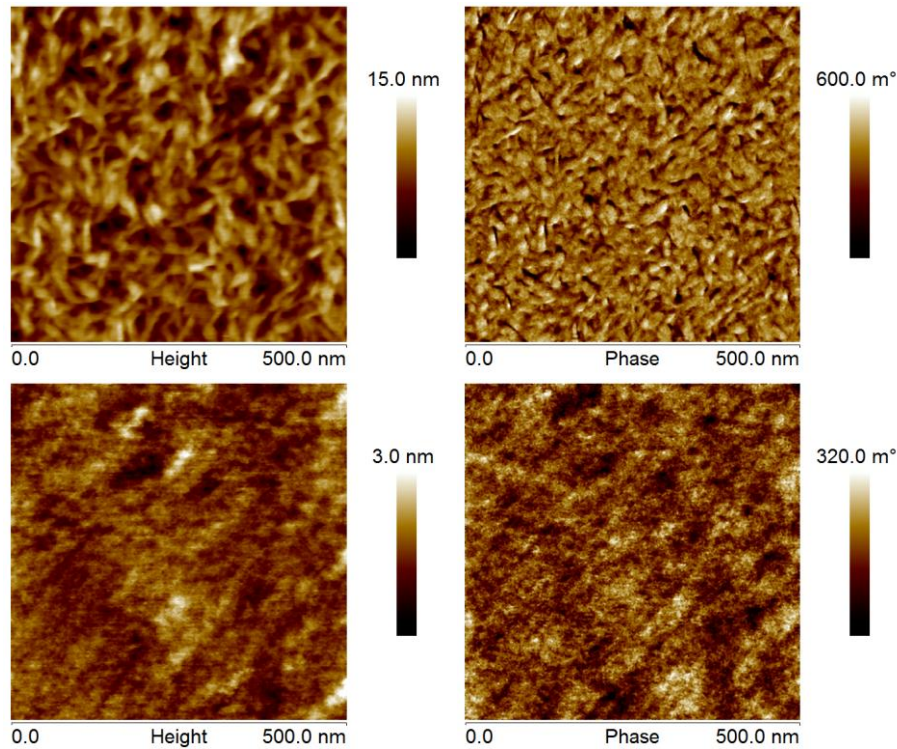
Fig. 83: AFM height (left) and phase (right) images, before (top) and after two hours of cellulosome incubation (bottom).

7.6.2 Proof of concept on FSEC 14 wt. %

The next measurement was tried on a FSEC 14 wt. % and started yielding the first problems. The time development is displayed in Fig. 84. After 1.25 h white lines started to appear (indicated in Fig. 84 by the blue arrow) while imaging, but only for a few minutes. When they stopped the image quality had dropped significantly indicating a tip problem, maybe something partly binding with the tip. Nevertheless measurements were carried on and lead to new problems with unusual artefacts appearing on the left side of the image (indicated in Fig. 84 by the green arrow). This also seemed to be a tip related problem, as it only occurred on the right side. The images shown were all captured in retrace, so these artifacts might be caused by something soft hanging on the tip and flipping side every time the cantilever changes direction.
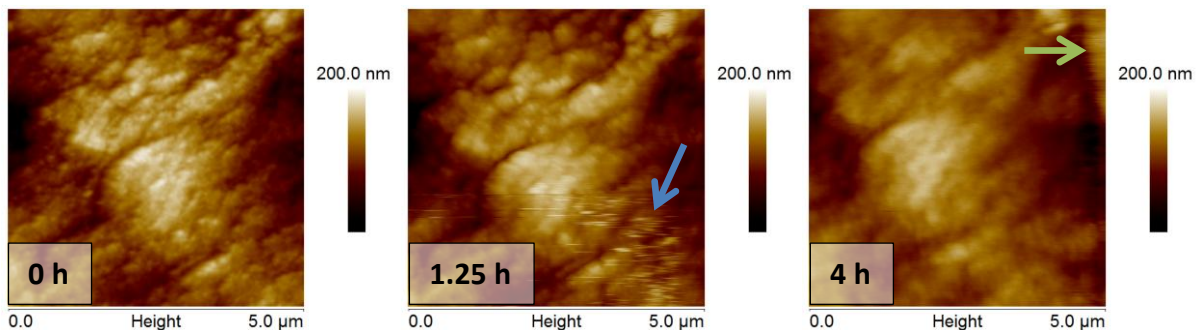
Fig. 84: AFM height image of FSEC 14 wt. % during cellulosome incubation. Before (left), after 1.25 h (middle), after 4 h (right).

7.6.3   Troubleshooting

Going precisely through all measurement steps (over 560 AFM images were taken in the process) and which results they yielded would take up too much room, therefore this chapter will summarize and show the main problems which occurred and the measures which were tried in order to conquer them. Fig. 85 shows the influential components of AFM imaging when capturing images of cellulose degradation by cellulosomes. All of these have been altered or tried during the measurements conducted and are described in extent in the following subchapters.
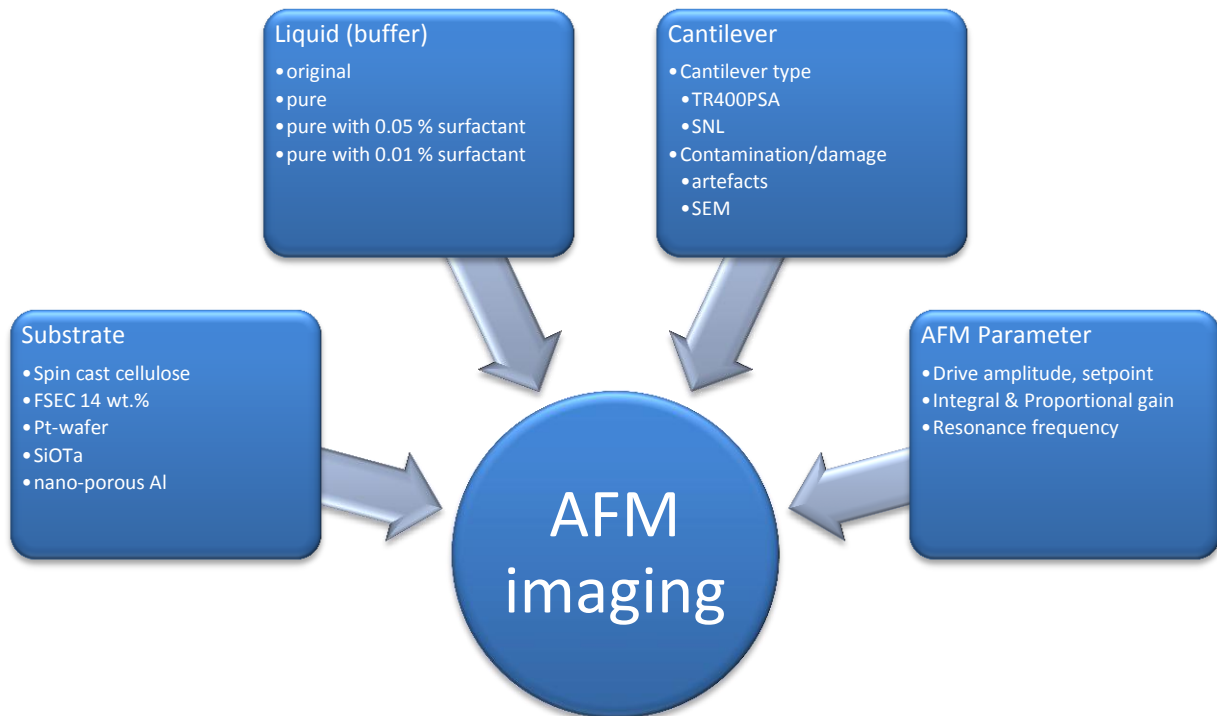
Fig. 85: Scheme of the influential components of AFM imaging for cellulosomes.

7.6.3.1   Substrate

The two cellulose substrates (FSEC and spin cast) both showed the behavior off white lines (Fig. 84 middle) when the cellulosomes had diffused to the measured region and artefacts on the right side where the tip changed direction (Fig. 84 right). With the cellulose substrate statements about the cantilever and the buffer solution are difficult to find. Therefore measurements were also conducted on substrates that would not be degraded by the cellulosomes or chemically attacked by the buffer solution.

A prestructured Pt-wafer was also used as sample and observed with standard buffer and cellulosomes added. After a while particles of varying size (15 – 150 nm) deposited on the surface. These particles on the Pt-wafer are not entirely fixed to a certain position and can also be seen on other substrates like SiOTa. The problem is that it is not clear what these particles are as they could be cellulosomes, parts of destroyed cellulosomes, buffer residue or precipitated buffer solution (see Fig. 86).

Porous Al was used as a standard reference. First the porous Al was measured with a SNL tip. Then the same tip was used for measuring a cellulose sample with cellulosomes. Finally the tip was used again for measuring the porous Al. This was done to find out if the tip gets damaged or contaminated, but this did not yield usable results as the SNL cantilever are generally not very usable.
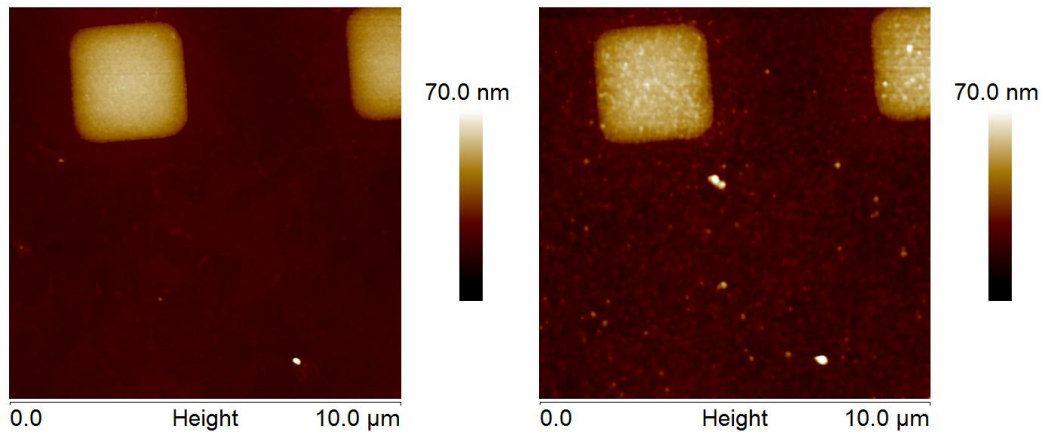
Fig. 86: 10 µm AFM height images of a prestructured Pt wafer before (left) and after (right) 7 hours cellulosome incubation.

7.6.3.2 Liquid (buffer solution)

Different kinds of buffer solutions were tried. The more components a buffer is made of, the more risky it gets for measuring in the AFM as undissolved residues or precipitated buffer solution can obscure the real surface. It quickly became clear, that the buffer is a source of problems. Therefore multiple buffers were tried, with varying results.

A cleaner buffer composed of 50 mM acetate pH 5.0, 12 mM $CaCl_2$ did not yield any noticeable positive changes.

Another approach was to add a surfactant to the buffer solution. 0.05 % TWEEN was added to the simple buffer, but the concentration was too high and bubbles started to agglomerate around the tip holder (Fig. 87), making measurements impossible.
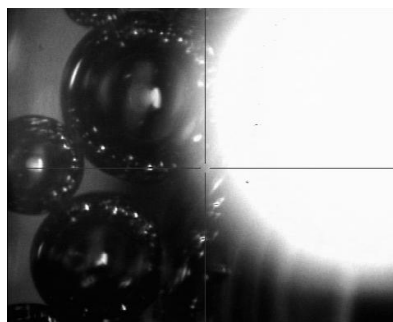
Fig. 87: Optical microscope image of the internal AFM optical microscope showing bubbles caused by surfactant agglomerating around the tip holder.

Reducing the surfactant to 0.01 % not only made imaging possible but actually yielded images of fascinating resolution and quality. An example showing spin cast cellulose is displayed in Fig. 88.

The variations of buffer solution (simpler, cleaner buffer; adding surfactants) which were tried out, did not resolve the imaging problem. Despite that with surfactants great resolution and quality were possible, once cellulosomes were added problems would arise. The image quality would become blurry and furthermore white lines and artefacts would appear (see Fig. 84).
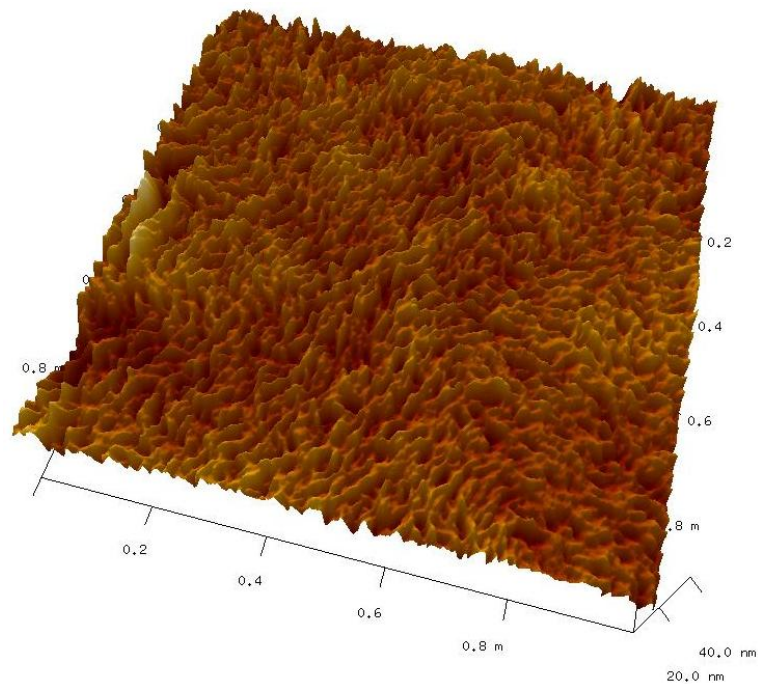
Fig. 88: 1 μm 3D AFM height image of spin cast cellulose in simple buffer with 0.01 % TWEEN.

7.6.3.3 Cantilever

Consideration was also given to the influence of the cantilever as well as its interaction with the buffer and the cellulosomes. Attachment of cellulosomes and/or buffer residue to the tip was considered and several measurements were conducted in order to prove or disprove that theory. For example one measurement conducted was imaging a certain, well defined sample (structured wafer). Then cellulose with cellulosomes would be imaged with the same tip. Finally the original sample was measured again to see how the recorded images changed, comparing before and after measurements. Also different probes were tried (Bruker SNL and Olympus TR400PSA), but the SNL probes proved nearly useless and did not work very well.

After all kinds of measurements were carried out it became evident that the most promising way to look for damage and contamination of the cantilever was in the SEM. A SEM image of the TR400PSA cantilever is displayed in the left image in Fig. 89. The whole cantilever is contaminated with what an EDX analysis revealed to probably be residues of the buffer. These residues are on the cantilever either because buffer residues attach to the cantilever while measurements are ongoing or because the cantilever was air-dried after removing it from the liquid cell, causing dried residues to stick on the cantilever. Which is more remarkable than the residues is the tip. A single cellulosome can be seen sticking nearly straight on top of the tip.

The SEM image of the SNL probe (Fig. 89 right image) also shows a cellulosome sticking on the head of the tip, indicating that this probably is happening quite regularly. This would also explain the artefacts that occurred when the cantilever changed direction (Fig. 84 right image) – the cellulosome would get stuck on the sample, the cantilever would rise till the cellulosome would bend over to the other side, then the cantilever would be close to the surface again and be able to image again. This also explains the loss of image quality, as the tip is considerably softer and also bigger through the cellulosome. The results found here were also a reason why it was tried to add surfactants to the buffer solution.

Despite these problems, interesting opportunities arise, as biological active and very specialised cantilevers with cellulosomes as tip-header become thinkable.
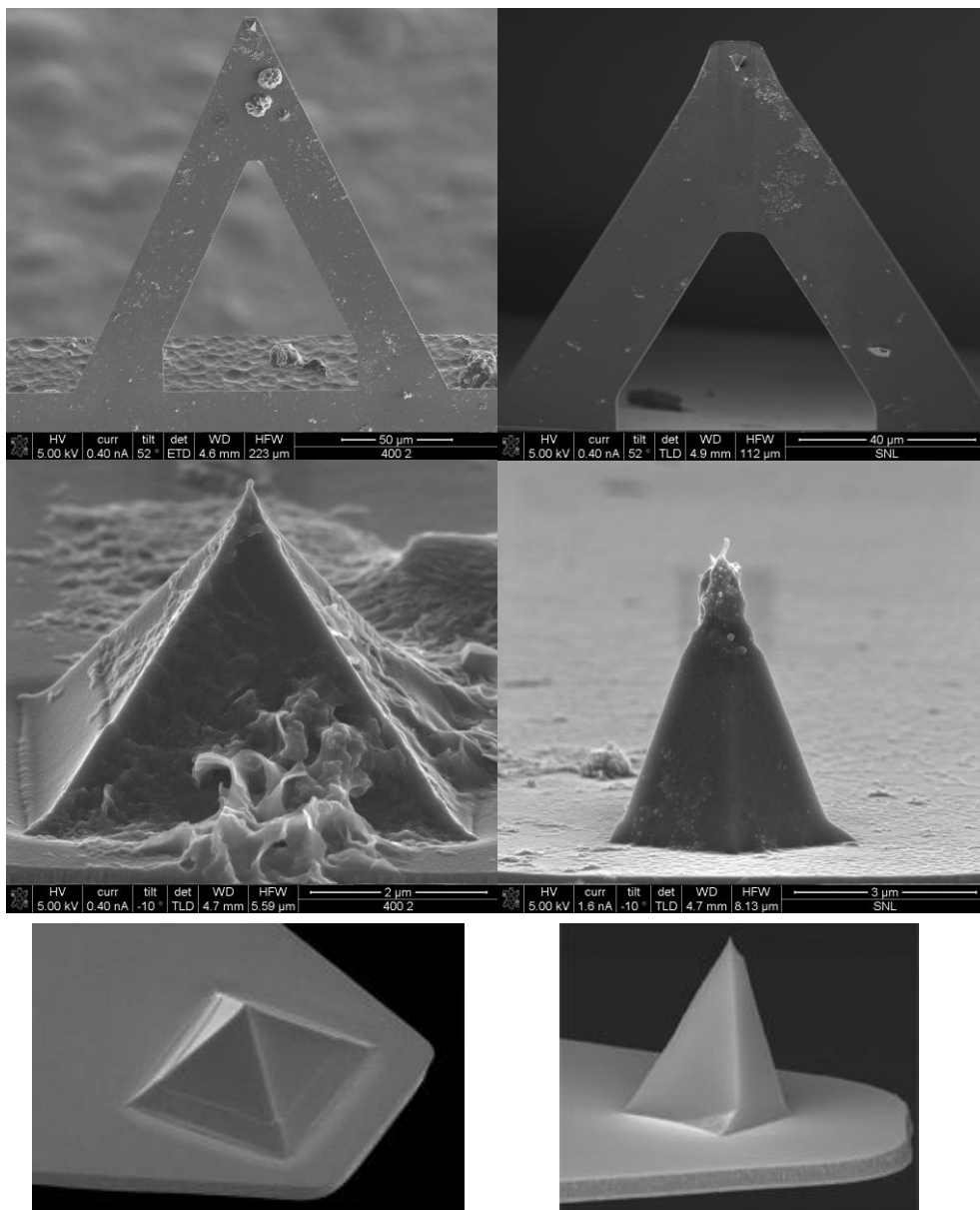
Fig. 89: SEM images of cantilevers. Left: Olympus TR400PSA, right: Bruker SNL. Top: used cantilever, middle: zoomed in on used tip, bottom: reference images [59], [60].

Imaging was performed on a spin cast cellulose sample with cellulosomes. After the image had blurred (as it always did) the cantilever was replaced with a new one. This was done in order to find out how long it takes for cellulosomes to attach to the tip. AFM height images before and after the change are displayed in Fig. 90. The left image was taken before the cantilever was exchanged. The right image was taken immediately after the cantilever was changed. The imaging direction is down and it shows in what short time the cantilever got contaminated, as the image quality drastically drops after two thirds of the image.
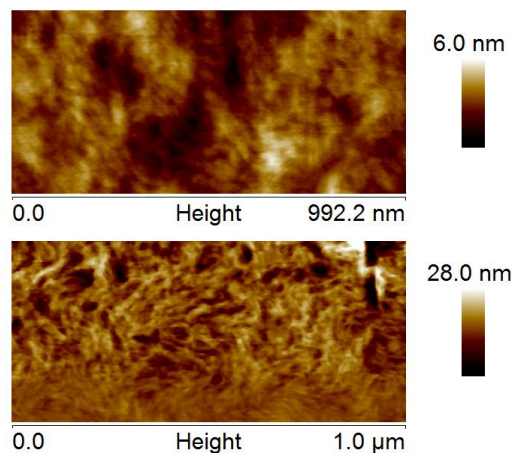
Fig. 90: AFM height images of spin cast cellulose with cellulosomes. Before (top) and after (bottom) exchanging cantilever.

7.6.3.4 AFM Parameter

The resonance curve of the cantilevers in liquid show multiple peaks of different modes (Fig. 17). Sometimes when imaging in liquid it can be beneficial to change to a different resonance frequency for measuring. But in this case no major improvement could be achieved.

Of course all possible parameters were varied. Different values for drive amplitude, amplitude setpoint, integral gain and proportional gain were tried in the "normal" regions (near the usually used values) to get better results or avoid the occurring problems, with no usable result.

Only after going to extreme values the imaging quality changed. In a series of measurements conducted on spin cast cellulose the image had become blurry (see Fig. 90). Relatively good images could be recorded after setting the drive amplitude to 3000 mV (!) and the amplitude setpoint to 8.0 V (common values in liquid are 100 − 500 mV for the drive amplitude and 0.8 − 3.0 V for the amplitude setpoint). The recorded image is displayed in Fig. 91. It again shows the characteristic fibrillar structure. This indicates that the high drive amplitude removed sludge and dirt from the surface and tip, making imaging possible again. Nevertheless measuring with such a high drive amplitude can lead to the sample taking damage, but will definitely destroy the tip quickly.
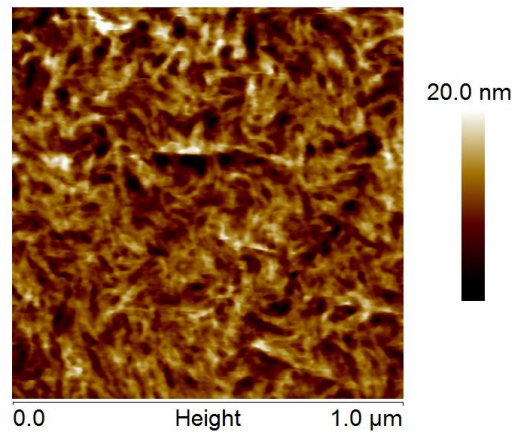
Fig. 91: 1 µm AFM height image of spin cast cellulose after 5.5 h of cellulosome incubation; drive amplitude of 3000 mV.

7.6.4 Summary and suggestions

Multiple problems while imaging with cellulosomes could be identified.

Buffer solution: The more complex the buffer solution is the more risky and difficult AFM-imaging becomes. Undissolved residues or precipitated buffer can deposit on the surface, rendering images meaningless. The buffer solution can also positively influence measurements, as a low concentration of surfactant improved imaging quality. Also the pH value is known to influence measurements in the LC-AFM [38]. These three variables (buffer composition, surfactant, pH) can be modified to gain better results.

Cantilever: The cantilever contaminated once the cellulosomes were added. The SEM images show cellulosomes on the tip, which strongly interferes with AFM imaging. Without exception silicon-nitride cantilever were examined in this work, a different chemical composition might prevent cellulosomes from binding to the cantilever. For this in-house chemical vapor deposition on a standard cantilever or a different cantilever are thinkable. Also the future prospect of a biological sensitive cantilever with a cellulosome as tip is promising.

Cellulosomes: They impaired measurements in two ways: they stick to the tips and they probably deposit as sludge which obscured the surface (e.g. Fig. 90.). Possibly the sludge is composed of parts of cellulosomes which were destroyed by the cantilever. If this were the case AFM-imaging of cellulose degradation by cellulosomes might be impossible, or only with extremely sensitive settings.

8 Summary

The main goal of this thesis was to produce and characterize artificial tunable cellulose substrates which are suitable the in situ AFM investigation of enzymatic degradation. Also a fast and easy test substrate was to be characterized. Finally the various cellulose samples were applied for in situ AFM measurements of enzymatic hydrolysis. This was done to make sure that the different substrates are usable for these experiments.

The first step was to refine the preparation method in order to get substrates of a more reproducible nature. An oil bath was constructed to ensure a constant environment and temperature during the dissolution of Avicel in the ionic liquid. Furthermore the drying after the fractional solvent exchange was improved to yield nanoflat surfaces. The samples are now smooth enough to allow high resolution AFM measurements on the native surface.

An additional task was to program a sample database to keep track of all samples of the project. This was done because a number of people work on the project and otherwise it can be very difficult to keep a clear overview of the samples. It offers an easy and fast way to look up sample properties and their process of production, without having to go through the lab notes.

In the main part the properties of different Avicel - BMIMCl mixing ratios were characterized. It has been found, that the maximum solubility of Avicel in BMIMCl is 8 wt. %. Samples with concentrations up to that value are of very amorphous cellulose 2 after regeneration. Higher concentrations result in microcrystalline Avicel being dispersed in the solution thus increasing the crystalline content. This means that the higher the ratio gets the more cellulose 1 can be found in the samples. Very high concentrations (larger or equal 12 wt. %) show problems with inhomogeneity. The samples show agglomerations of undissolved Avicel crystals. When the samples are stirred longer they become homogeneous with a finely dispersed cellulose 1 crystals in a cellulose 2 matrix, being closer to natural cellulose than any other artificial substrate. A test substrate was also characterized. It is easy and fast to produce and consists of highly amorphous cellulose 2. The topology shows very fine fibers of $1.5 - 15$ nm diameter.

The final part was to test the samples in enzymatic degradation to prove the applicability for AFM experiments on the one hand and the relevance compared to natural cellulose on the other hand. Samples consisting of cellulose 2, cellulose 2 / cellulose 1 and spin cast samples were subject to enzymatic degradation. Various enzymes and enzymatic combinations were subjected on the samples. The results confirmed findings about the specific preferential degradation of certain enzymes by [1] and proved the usefulness of having different substrates available. Furthermore, in situ AFM investigations of cellulosomes on cellulose substrates were conducted, but turned out to be very complicated due to many problems arising. A multitude of variations (parameter, substrates, cantilever and buffer solution) was performed to find out what was happening during the measurements.

To conclude, it is now possible to produce tunable substrates with specific properties regarding their crystallinity. A simple test substrate has been established. Both samples (low and high concentration) tested in enzymatic degradation showed good results. The tunable substrates proved their value for visualising specific enzymatic degradation on a nanoscale.

9 Outlook

With the tunable substrates it is possible to specifically characterize enzymatic degradation. This allows for further investigations with other enzymes and other enzymatic systems, like non-hydrolytic enzymes. Especially research on cellulosomes seems to be very promising with the synergistic possibilities the multi-enzyme complex offers.

Additional effort put into the spin coat samples should produce interesting results, as the spin coat samples offer many possibilities of tuning. Multi-layered systems with varying layers are conceivable and subject of ongoing research at the FELMI.

Another interesting opportunity, found during the research, was the possibility of biologically sensitive cantilever which were activated with a cellulosome as tip. This can allow for chemical sensitive AFM imaging, offering a multitude of new opportunities.

10 List of tables

11 List of figures

12 List of abbreviations

°	…	degree
^{13}C NMR	…	carbon-13 nuclear magnetic resonance spectroscopy
AFM	…	atomic force microscopy
Avicel	…	microcrystalline cellulose
BMIMCl	…	1-N-butyl-3-methylimidazolium chloride
CBD	…	cellulose binding domain
CBH1	…	cellobiohydrolase 1
CBH2	…	cellobiohydrolase 2
EG	…	endoglucanase
FSEC	…	fractional solvent exchanged cellulose
IL	…	ionic liquid
LC	…	liquid cell
PG	…	primary gel
SAXS	…	small angle X-ray scattering
SEM	…	scanning electron microscope
TEM	…	transmission electron microscope
WAXS	…	wide angle X-ray scattering
XRD	…	X-ray diffractometer

13 Bibliography

[1] T. Ganner, P. Bubner, M. Eibinger, C. Mayrhofer, H. Plank und B. Nidetzky, „Dissecting and Reconstructing Synergism: IN SITU VISUALIZATION OF COOPERATIVITY AMONG CELLULASES," *Journal of Biological Chemistry,* Bd. 287, Nr. 52, pp. 43215-43222, 2012.

[2] H. A. Krässig, Cellulose, Switzerland: Gordon and Breach Science Publishers, 1993.

[3] J.-L. Wertz, O. Bédué und J. P. Mercier, Cellulose Science and Technology // Cellulose science and technology, 1 Hrsg., Lausanne: EPFL Press, 2010, p. 364.

[4] D. Klemm, B. Heublein, H.-P. Fink und A. Bohn, „Cellulose: Fascinating Biopolymer and Sustainable Raw Material," *Angewandte Chemie International Edition,* Bd. 44, Nr. 22, pp. 3358-3393, 2005.

[5] D. Klemm, H.-P. Schmauder und T. Heinze, „Cellulose," *Biopolymers Online,* pp. 275-287, 2005.

[6] A. C. O'Sullivan, „Cellulose: the structure slowly unravels," *Cellulose,* Bd. 4, Nr. 3, pp. 173-207, 1997.

[7] H. Yamamoto und F. Horii, „CPMAS carbon-13 NMR analysis of the crystal transformation induced for Valonia cellulose by annealing at high temperatures," *Macromolecules,* Bd. 26, Nr. 6, pp. 1313-1317, 1993.

[8] J. S. Wilkes, „A short history of ionic liquids—from molten salts to neoteric solvents," *Green Chemistry,* Bd. 4, Nr. 2, pp. 73-80, 2002.

[9] F. Hermanutz, F. Gähr, E. Uerdingen, F. Meister und B. Kosan, „New Developments in Dissolving and Processing of Cellulose in Ionic Liquids," *Macromolecular Symposia,* Bd. 262, Nr. 1, pp. 23-27, 2008.

[10] H. Wang, G. Gurau und R. D. Rogers, „Ionic liquid processing of cellulose," *Chemical Society Reviews,* Bd. 41, Nr. 4, p. 1519, 2012.

[11] K. R. Seddon, „Ionic Liquids for Clean Technology," *J. Chem. Tech. Biotechnol.,* Bd. 68, pp. 351-356, 1997.

[12] T. T. P. Pham, C.-W. Cho und Y.-S. Yun, „Environmental fate and toxicity of ionic liquids: A review," *Water Research,* Bd. 44, Nr. 2, pp. 352-372, 2010.

[13] M. Mazza, D.-A. Catana, C. Vaca-Garcia und C. Cecutti, „Influence of water on the dissolution of cellulose in selected ionic liquids," *Cellulose,* Bd. 16, Nr. 2, pp. 207-215, 2009.

[14] J. S. Moulthrop, R. P. Swatloski, G. Moyna und R. D. Rogers, „High-resolution 13C NMR studies of cellulose and cellulose oligomers in ionic liquid solutions," *Chemical Communications,* Nr. 12, p. 1557, 2005.

[15] R. P. Swatloski, S. K. Spear, J. D. Holbrey und R. D. Rogers, „Dissolution of Cellose with Ionic Liquids," *Journal of the American Chemical Society,* Bd. 124, Nr. 18, pp. 4974-4975, 2002.

[16] J.-i. Kadokawa, M.-a. Murakami und Y. Kaneko, „A facile preparation of gel materials from a solution of cellulose in ionic liquid," *Carbohydrate Research,* Bd. 343, Nr. 4, pp. 769-772, 2008.

[17] R. C. Remsing, R. P. Swatloski, R. D. Rogers und G. Moyna, „Mechanism of cellulose dissolution in the ionic liquid 1-n-butyl-3-methylimidazolium chloride: a 13C and 35/37Cl NMR relaxation

study on model systems," *Chemical Communications,* Nr. 12, p. 1271, 2006.

[18] M. Freemantle, An Introduction to ionic liquids, Cambridge, UK: RSC Pub., 2010, pp. xiv, 281.

[19] M. Bhat und S. Bhat, „Cellulose degrading enzymes and their potential industrial applications," *Biotechnology Advances,* Bd. 15, Nr. 3–4, pp. 583-620, 1997.

[20] H. Esterbauer, W. Steiner, I. Labudova, A. Hermann und M. Hayn, „Production of Trichoderma cellulase in laboratory and pilot scale," *Enzymatic Hydrolysis of Cellulose,* Bd. 36, Nr. 1, pp. 51-65, 1991.

[21] G. Pettersson, M. Linder, T. Reinikainen, T. Drakenberg, M.-L. Mattinen, A. Annila, M. Kontteli, G. Lindeberg und J. Ståhlberg, „Identification of functionally important amino acids in the cellulose-binding domain of Trichoderma reesei cellobiohydrolase I," *Protein Science,* Bd. 4, Nr. 6, pp. 1056-1064, 1995.

[22] J. Rouvinen, T. Bergfors, T. Teeri, J. Knowles und T. Jones, „Three-dimensional structure of cellobiohydrolase II from Trichoderma reesei," *Science,* Bd. 249, Nr. 4967, pp. 380-386, 1990.

[23] W. Aehle, Enzymes in industry, 3 Hrsg., Weinheim, Chichester: Wiley-VCH;John Wiley [distributor], 2007, pp. 1 ressource en ligne (xxvi, 489.

[24] Thomas Ganner, „Enzymatic cellulose degradation via atomic force microscopy in liquid environments," Graz University of Technology, Graz, Austria, 2012.

[25] Ilan Levy und Oded Shoseyov, „Cellulose-binding domains: Biotechnological applications," *Biotechnology Advances,* Bd. 20, Nr. 3–4, pp. 191-213, 2002.

[26] C. M. Fontes und H. J. Gilbert, „Cellulosomes: Highly Efficient Nanomachines Designed to Deconstruct Plant Cell Wall Complex Carbohydrates," *Annual Review of Biochemistry,* Bd. 79, Nr. 1, pp. 655-681, 2010.

[27] E. A. Bayer, E. Morag und R. Lamed, „The cellulosome — A treasure-trove for biotechnology," *Trends in Biotechnology,* Bd. 12, Nr. 9, pp. 379-386, 1994.

[28] E. A. e. a. Bayer, „Cellulosomes—Structure and Ultrastructure," *Journal of structural biology,* Nr. 124, pp. 221-234, 1998.

[29] G. H. Michler, Ultramikrotomie in der Materialforschung, 1 Hrsg., München: Hanser, 2004, p. 242.

[30] *Courtesy of FELMI- ZFE, Institute for Electron Microscopy and Nanoanalysis, TU Graz, Austria, www.felmi-zfe.at.*

[31] E. F. Kaelble, HANDBOOK OF X-RAYS, 1 Hrsg., USA: McGraw-Hill Inc., 1967.

[32] H. P. Klug und L. Alexander, X-ray Diffraction Procedures for Polycrystalline and Amorphous Materials, John Wiley & Sons Inc, 1954.

[33] E. Smith und G. Dent, Modern Raman spectroscopy, Hoboken, NJ: J. Wiley, 2005, pp. x, 210.

[34] L. Reimer, Scanning electron microscopy, Berlin ;, New York: Springer-Verlag, 1985, pp. xviii, 457.

[35] J. Goldstein, Scanning electron microscopy and x-ray microanalysis, 3 Hrsg., New York: Kluwer Academic/Plenum Publishers, 2003, pp. xix, 689.

[36] D. B. Williams und C. B. Carter, Transmission electron microscopy, 2 Hrsg., New York ;, London: Springer, 2009, pp. LXII, 760.

[37] R. C. García, Amplitude modulation atomic force microscopy, Weinheim, Chichester: Wiley-

VCH;John Wiley [distributor], 2010, pp. 1 online resource (xiv, 179.

[38] V. J. Morris, A. R. Kirby und A. P. Gunning, Atomic force microscopy for biologists, 2 Hrsg., London: Imperial College Press, 2010, pp. 1 online resource (xiii, 406.

[39] *Courtesy of Harald Plank, Institute for Electron Microscopy and Nanoanalysis (FELMI_ZfE), TU Graz, Austria, www.felmi-zfe.at.*

[40] J. E. Sader und R. C. Sader, „Susceptibility of atomic force microscope cantilevers to lateral forces: Experimental verification," *Applied Physics Letters,* Bd. 83, Nr. 15, p. 3195, 2003.

[41] K. Prasad, Y. Kaneko und J.-i. Kadokawa, „Novel Gelling Systems of κ -, ι - and λ -Carrageenans and their Composite Gels with Cellulose Using Ionic Liquid," *Macromolecular Bioscience,* Bd. 9, Nr. 4, pp. 376-382, 2009.

[42] Judith Dohr, „Enzymatic degradation of superflat cellulose surfaces," Karl Franzens University of Graz, Graz, Austria, 2011.

[43] E. Kontturi, T. Tammelin und M. Osterberg, „Cellulose--model films and the fundamental approach," *Chemical Society reviews,* Bd. 35, Nr. 12, pp. 1287-1304, 2006.

[44] E. Kontturi, M. Suchy, P. Penttilä, B. Jean, K. Pirkkalainen, M. Torkkeli und R. Serimaa, „Amorphous Characteristics of an Ultrathin Cellulose Film," *Biomacromolecules,* Bd. 12, Nr. 3, pp. 770-777, 2011.

[45] T. Mohan, R. Kargl, A. Doliška, A. Vesel, S. Köstler, V. Ribitsch und K. Stana-Kleinschek, „Wettability and surface composition of partly and fully regenerated cellulose thin films from trimethylsilyl cellulose," *Journal of Colloid and Interface Science,* Bd. 358, Nr. 2, pp. 604-610, 2011.

[46] U. Richter, T. Krause und W. Schempp, „Untersuchungen zur Alkalibehandlung von Cellulosefasern. Teil 1. INFRAROTSPEKTROSKOPISCHE UND RÖNTGENOGRAPHISCHE BEURTEILUNG DER ÄNDERUNG DES ORDNUNGSZUSTANDES," *Angewandte Makromolekulare Chemie,* Bd. 185, Nr. 1, pp. 155-167, 1991.

[47] S. Park, J. O. Baker, M. E. Himmel, P. A. Parilla und D. K. Johnson, „Cellulose crystallinity index: measurement techniques and their impact on interpreting cellulase performance," *Biotechnology for Biofuels,* Bd. 3, Nr. 1, pp. 1-10, 2010.

[48] G. Sèbe, F. Ham-Pichavant, E. Ibarboure, A. L. C. Koffi und P. Tingaut, „Supramolecular Structure Characterization of Cellulose II Nanowhiskers Produced by Acid Hydrolysis of Cellulose I Substrates," *Biomacromolecules,* Bd. 13, Nr. 2, pp. 570-578, 2012.

[49] A. Thygesen, J. Oddershede, H. Lilholt, A. B. Thomsen und K. Ståhl, „On the determination of crystallinity and cellulose content in plant fibres," *Cellulose,* Bd. 12, Nr. 6, pp. 563-576, 2005.

[50] G. Cheng, P. Varanasi, C. Li, H. Liu, Y. B. Melnichenko, B. A. Simmons, M. S. Kent und S. Singh, „Transition of Cellulose Crystalline Structure and Surface Morphology of Biomass as a Function of Ionic Liquid Pretreatment and Its Relation to Enzymatic Hydrolysis," *Biomacromolecules,* p. 110225153814046, 2011.

[51] J. H. Wiley und R. H. Atalla, „Band assignments in the raman spectra of celluloses," *Carbohydrate Research,* Bd. 160, Nr. 0, pp. 113-129, 1987.

[52] K. Schenzel und S. Fischer, „Applications of FT Raman spectroscopy for the characterization of cellulose," *Lenzinger Berichte,* Bd. 83, pp. 64-70, 2004.

[53] K. Schenzel, S. Fischer und E. Brendler, „New Method for Determining the Degree of Cellulose I Crystallinity by Means of FT Raman Spectroscopy," *Cellulose,* Bd. 12, Nr. 3, pp. 223-231, 2005.

[54] K. Schenzel, H. Almlöf und U. Germgård, „Quantitative analysis of the transformation process of cellulose I → cellulose II using NIR FT Raman spectroscopy and chemometric methods," *Cellulose,* Bd. 16, Nr. 3, pp. 407-415, 2009.

[55] R. W. Berg, M. Deetlefs, K. R. Seddon, I. Shim und J. M. Thompson, „Raman and ab Initio Studies of Simple and Binary 1-Alkyl-3-methylimidazolium Ionic Liquids," *The Journal of Physical Chemistry B,* Bd. 109, Nr. 40, pp. 19018-19025, 2005.

[56] K. Schenzel und S. Fischer, „NIR FT Raman Spectroscopy - a Rapid Analytical Tool for Detecting the Transformation of Cellulose Polymorphs," *Cellulose,* Bd. 8, pp. 49-57, 2001.

[57] P. Krishnamachari, R. Hashaikeh und M. Tiner, „Modified cellulose morphologies and its composites; SEM and TEM analysis," *Micron,* Bd. 42, Nr. 8, pp. 751-761, 2011.

[58] S. Elazzouzi-Hafraoui, Y. Nishiyama, J.-L. Putaux, L. Heux, F. Dubreuil und C. Rochas, „The Shape and Size Distribution of Crystalline Nanoparticles Prepared by Acid Hydrolysis of Native Cellulose," *Biomacromolecules,* Bd. 9, Nr. 1, pp. 57-65, 2008.

[59] „http://www.asylumresearch.com/Probe/TR400PSA,Olympus," [Online]. [Zugriff am 02 02 2013].

[60] „http://www.brukerafmprobes.com/Product.aspx?ProductID=3693," [Online]. [Zugriff am 02 02 2013].

Appendix A

Oil bath – oil bath (1) and cover (2)

Oil bath - inlet

Database structure

tabUser
IDUserNum
txtUserCode
txtPasswort
intSecLevel
txtUserName
txtUserInitials

tabSample
IDSampleNum
txtDescrShort
datDate
timTime
intMixNum
txtDescrLong
txtPerson
txtSampleName
intFromSampleNum
intProjNum

tabProjects
IDProjNum
txtDescr

tabDocument
IDDocument
intSampleNum
txtFileName
txtDescr

tabShortDescr
IDShortDescr
txtShortDescr
txtDescr

tabMixture
IDMixNum
datDate
timTime
txtCellulose
txtIonicLiquid
dblWtPercCellul
txtAdditive
dblWtPercAddit
txtStirringStrength
dblStirringDurat
dblTemp
txtBox
txtInfo